# ADVANCES IN TIP-ENHANCED RAMAN AND PHOTOLUMINESCENCE SPECTROSCOPY

A Dissertation

by

ZHE HE

Submitted to the Office of Graduate and Professional Studies of
Texas A&M University
in partial fulfillment of the requirements for the degree of

DOCTOR OF PHILOSOPHY

| | |
|---|---|
| Chair of Committee, | Marlan O. Scully |
| Committee Members, | Alexei V. Sokolov |
| | Philip Hemmer |
| | Alexey A. Belyanin |
| Head of Department, | Grigory Rogachev |

May 2020

Major Subject: Physics

ABSTRACT

Tip-enhanced Raman scattering (TERS) and tip-enhanced photoluminescence (TEPL) can be widely applied to multi-disciplinary studies involving near-field scanning technologies. Several types of TERS setups have been applied in fields including biosensing, high-resolution imaging, and photocatalysis. After 20 years of development, TERS has been improved to resolve sub-nanometer structures with a high enhancement factor at $10^{13}$ over traditional Raman scattering. Furthermore, due to the quantum plasmonic effects, the tip-molecule interactions play a significant role during TERS measurements. In this dissertation, we will discuss the applications of TERS and TEPL in both the classical and quantum ways. In the classical regime, where the tip-molecule interactions are less important, we introduce our efforts to achieve bioimaging at sub-nanometer resolution. So as to understand the essential mechanisms, we introduce an innovative model of tip-substrate cavities and discuss several distinct enhancement scenarios. On the other hand, in the quantum regime, where charge transfer effects are unavoidable, we work out a theoretical model involving the charge transfer and apply it to study and control photoelectrical properties of 2D semiconductors. Consequently, this dissertation summarizes the overall properties of TERS, for the purpose of classifying different regimes and extending the applications to multidisciplinary branches of biophysics and biochemistry.

ACKNOWLEDGEMENTS

I would like to thank my committee chair, Dr. Scully, and my committee members, Dr. Sokolov, Dr. Hemmer, and Dr. Belyanin, for their guidance and support throughout the course of this research.

Thanks also go to my friends and colleagues and the department faculty and staff for making my years as a graduate student at Texas A&M University a wonderful experience.

Finally, thanks to my family for their encouragement and support.

CONTRIBUTORS AND FUNDING SOURCES

## Contributors

This work was supervised by a dissertation committee consisting of Professor Marlan O. Scully, Professor Alexei V. Sokolov, Professor Philip Hemmer, and Professor Alexey Belyanin of the Department of Physics.

All work conducted for the dissertation was completed by the student independently.

## Funding Sources

Graduate study was supported by the Herman F. Heep and Minnie Belle Heep Texas A&M University Endowed Fund held/administered by the Texas A&M Foundation.

# NOMENCLATURE

| | |
|---|---|
| SERS | Surface-enhanced Raman scattering |
| TERS | Tip-enhanced Raman scattering |
| SPR | Surface plasmon resonance |
| LSP | Localized surface plasmon |
| NSOM | Near-field scanning optical microscopy |
| CuPC | Copper phthalocyanine |
| $MoS_2$ | Molybdenum disulfide |
| CT | Charge transfer |
| EF | Enhancement factor |
| DNA | Deoxyribonucleic acid |
| AFM | Atomic force microscope |
| KPFM | Kelvin probe force microscope |
| A | Adenine |
| C | Cytosine |
| G | Guanine |
| T | Thymine |
| TEPL | Tip-enhanced photoluminescence |
| TEQPL | Tip-enhanced quantum plasmonics |
| $MoSe_2$ | Molybdenum diselenide |
| $WSe_2$ | Tungsten diselenide |

| | |
|---|---|
| HS | Heterostructure |
| $WS_2$ | Tungsten disulfide |
| QC | Quantum coupling |
| CC | Classical coupling |
| NF | Near-field |
| FF | Far-field |
| PL | Photoluminescence |

TABLE OF CONTENTS

Page

LIST OF FIGURES

Page

LIST OF TABLES

Page

# 1. INTRODUCTION

In chemistry, biology and many other fields of science and engineering, spectroscopy is widely applied for studying components and structures of materials. Among multiple types of spectroscopic techniques, Raman spectroscopy stands out due to its inherit sensitivity to the details of molecular bonds that identify multicomponent features in a complex system. This Raman-spectroscopic information is extremely helpful in chemical and structural analysis. Nevertheless, two drawbacks are known to limit Raman spectroscopy. One is low sensitivity due to the small cross-section of Raman scattering. The cross section can be estimated as $\sigma_R \sim \frac{1}{\lambda^4}$ where $\lambda$ is the wavelength of incident photons [1]. As a comparison, the cross-section corresponding to fluorescence can be as large as $10^{-18}\ cm^2$, while the Raman cross-section is typically $10^{-30}\ cm^2$. Though the exact value varies upon the frequency of the incident light, the Raman signals are usually assumed to be quite weak, especially when working with low-concentration biomolecules. The other restriction is the diffraction limit of optical imaging based on the Abbe theory [2]. According to the Abbe diffraction limit, the resolution of a microscope image is $d = \frac{\lambda}{2NA}$. $\lambda$ here is again the incident light wavelength, and $NA = nsin(\theta)$ is the numerical aperture, with refractive index n and half-angle $\theta$. When we use green incident light at 532 nm wavelength with an NA=0.9 objective, the smallest size we can resolve is 296 nm.

By introducing surface-enhanced Raman scattering (SERS), we aim for a simple solution allowing to increase signal-to-noise ratio of traditional Raman spectroscopy, while at the same time enhancing the spatial resolution. Back in 1973, the SERS effect was observed

as Raman scattering enhancement [3]. There are two main mechanisms to explain this effect, respectively, electromagnetic and chemical mechanisms [4]. The electromagnetic explanation focuses on the surface plasmon resonance (SPR) which provides the enhanced localized electric field. One of the means to realize SPR is to excite localized surface plasmon (LSP) with nanostructures. The LSP decays and causes light emission at the same frequency as the incident light. Consequently, due to these nano-scale emitters, the electric field nearby is dramatically stronger than the far field. The localized electric field enhancement is also known as the near-field effect. Granting that LSP can be generated with few restrictions and less expense, carrier structures such as Au nanoparticles and Au nanoplates are frequently adopted in SERS experiments.

By way of contrast, instead of traditional SERS, we use tip-enhanced Raman spectroscopy (TERS) to overcome the diffraction limit. In TERS measurements, signal enhancement is provided by a cone antenna made of noble metals. The nanoscale antenna, known as the tip, is usually fabricated by silicon coated with gold or silver. In a similar way, it can provide electric field enhancement upon resonant excitations. Usually, the resonance condition of tips is not strict due to the wide-band surface plasmon energy. As a consequence, a tip can be used in many conditions to collect intrinsically weak signals. As discussed above, TERS can overcome the diffraction limit because the localized electric field is of a similar size to the nanostructure. A common technique to utilize this feature is working under with a scanning probe microscope. According to the purposes and sample materials, some options such as the atomic force microscope (AFM), scanning

tunneling microscope (STM) or aperture mode near-field scanning optial microscope (NSOM) could be used for TERS measurements.

Provided that the actual enhancement factors are affected by shapes, materials, and sizes of tips, these are extra factors determining the resolving ability of TERS. The minimum spatial resolution of TERS is still under debate. In the traditional model, the electric field generated by a plasmonic tip is confined to an equally small area as the tip. Due to the technique limit of tip fabrication, the spatial resolution is assumed to be as small as 10 nm. Though 10 nm is already far below the diffraction limit, yet it cannot reach the single-molecule level. However, recently, many experiments have shown that TERS can realize single molecule sensing and even imaging [5], [6]. The best resolution reported was even less than 1 Å. One reasonable guess is that atomic structures on the tip guarantee the sub-nanometer resolution. These atomic structures might be formed during metal deposition and perform as mini-tips. During the measurement, certain mini-tips would contribute to single-molecule detections.

While spatial resolutions of TERS are proved to be single-molecule level, more efficient setups are also developed through years. By forming a plasmonic cavity with two or more metallic structures, better enhancement is observed. Under those circumstances, the usage of plasmonic cavity formed by a tip and a metallic substrate is utilized, namely, gap-mode TERS [7]. Compared to traditional TERS with a mono tip, the gap-mode configuration shows furtherly confined electric field between the tip and the substrate. This setup can promote the enhancement factor of TERS from $10^4$ to $10^{13}$.

Despite the gap-mode TERS is supposed to provide stronger enhancement effects, it has some huge drawbacks. In order to generate gap plasmon, the distance between a tip and substrates has to be optimized within 0.5 nm. Otherwise, larger distances can subsequently decrease enhancement factors. Therefore, the gap-mode configuration may not be applied for bulky samples including biological cells. Instead, it is suitable to single-molecule sensing and low-dimensional materials. In the following chapters, I focused on studies of single-molecule imaging and 2D semiconductor by gap-mode TERS.

Besides TERS, we also introduce a technique call tip-enhanced photoluminescence (TEPL) in order to study 2D semiconductors such as $MoS_2$. Though photoluminescence is different from Raman scattering, the electromagnetic enhancement mechanisms of tips are similar. Therefore, TEPL is an alternative method of TERS to study materials of photoluminescence.

This dissertation focuses on applications of tip-enhanced spectroscopies including both TERS and TEPL. Chapter 2 discusses two different mechanisms of TERS and shows their different effects. Chapter 3 shows sub-nanometer imaging of a DNA strand and performs the single-base sequencing. Chapter 4 and 5 demonstrate nanoscale photoresponse control of 2D semiconductor by tip-enhanced photoluminescence (TEPL) and tip-enhanced quantum plasmonics (TEQPL). The first two chapters are concentrated on molecule imaging while the next two chapters are focused on interactions of plasmon and materials upon quantum effects.

### 1.1. References


[1] W. R. Fenner, H. A. Hyatt, J. M. Kellam, and S. P. S. Porto, “Raman cross section of some simple gases,” *JOSA*, vol. 63, no. 1, pp. 73–77, Jan. 1973, doi: 10.1364/JOSA.63.000073.

[2] O. Scherzer, “The Theoretical Resolution Limit of the Electron Microscope,” *J. Appl. Phys.*, vol. 20, no. 1, pp. 20–29, Jan. 1949, doi: 10.1063/1.1698233.

[3] M. Fleischmann, P. J. Hendra, and A. J. McQuillan, “Raman spectra of pyridine adsorbed at a silver electrode,” *Chem. Phys. Lett.*, vol. 26, no. 2, pp. 163–166, May 1974, doi: 10.1016/0009-2614(74)85388-1.

[4] A. Campion and P. Kambhampati, “Surface-enhanced Raman scattering,” *Chem. Soc. Rev.*, vol. 27, no. 4, pp. 241–250, 1998, doi: 10.1039/A827241Z.

[5] J. Lee, K. T. Crampton, N. Tallarida, and V. A. Apkarian, “Visualizing vibrational normal modes of a single molecule with atomically confined light,” *Nature*, vol. 568, no. 7750, pp. 78–82, Apr. 2019, doi: 10.1038/s41586-019-1059-9.

[6] C. Chen, N. Hayazawa, and S. Kawata, “A 1.7 nm resolution chemical analysis of carbon nanotubes by tip-enhanced Raman imaging in the ambient,” *Nat. Commun.*, vol. 5, no. 1, pp. 1–5, Feb. 2014, doi: 10.1038/ncomms4312.

[7] W. Zhang, B. S. Yeo, T. Schmid, and R. Zenobi, “Single Molecule Tip-Enhanced Raman Spectroscopy with Silver Tips,” *J. Phys. Chem. C*, vol. 111, no. 4, pp. 1733–1738, Feb. 2007, doi: 10.1021/jp064740r.

## 2. TIP-ENHANCED RAMAN SCATTERING ON BULK $MOS_2$[*]

Surface-enhanced Raman scattering (SERS) has many applications in nanotechnology, biophotonics and high-resolution single molecule detection. Typically, it is performed using surface plasmon resonances, by noble metal nanostructures such as gold nanoparticles, gold or silver film deposited with target molecules. Tip-enhanced Raman spectroscopy (TERS) makes use of a nano-sized tip apex that provides localized plasmonic enhancement of the electromagnetic near field, which can be used for high resolution imaging and detection. We investigate the response of $MoS_2$ substrate to a gold tip and show the surface-enhanced and tip-enhanced Raman signals of copper phthalocyanine molecules (CuPc). The $MoS_2$ substrate changes relative intensity of molecular vibrations around the CuPc/$MoS_2$ interface, and especially effects the metal involved bonds of CuPc. It also reinforces tip enhanced Raman scattering (TERS) through an interaction with the gold tip.

---

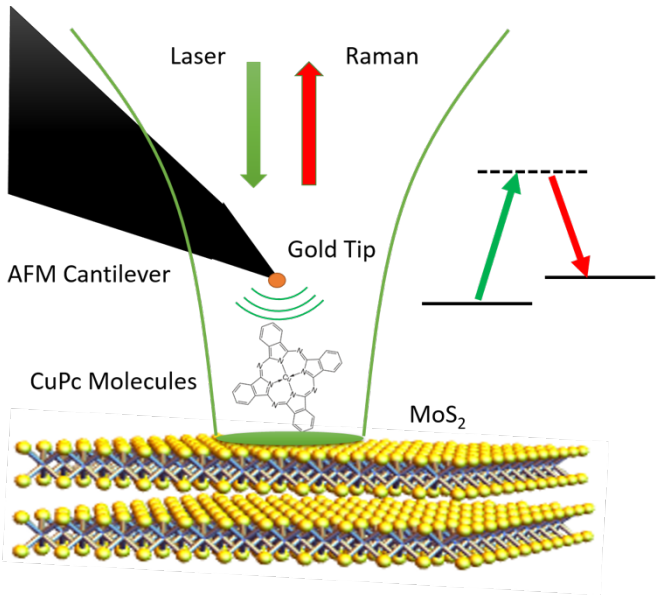


**Figure 2.1 Scheme of the experimental setup. The gold nanosphere tip at the apex of the AFM cantilever has a diameter 200 nm. The 532 nm laser beam was focused on the tip in AFM tapping mode over the CuPc/Substrate sample. The Raman signal was collected using a spectrometer above the sample. The CuPc sample was prepared by chemical vapor deposition on a MoS2, gold and SiO2 substrates.**

## 2.1. Introduction

### 2.1.1. Surface enhanced Raman scattering of CuPc

Surface-enhanced Raman scattering (SERS) is a powerful technique to investigate the molecular vibrations with high sensitivity and resolution [1]. The energy transfer and charge transfer near the junction of two materials potentially change the intensity of Raman scattering. Here we investigated the enhancement of Raman signal of copper phthalocyanine (CuPc) molecules and compare the SERS and TERS contributions with a $MoS_2$ substrate.

### 2.1.2. Molybdenum disulfide ($MoS_2$)

Molybdenum disulfide ($MoS_2$) has been meticulously investigated using Raman scattering [1], [2], [3]. The surface enhancement of molecular substrate Raman signals on $MoS_2$ substrates attracted attention due to the flat surface of 2D materials. Recent studies showed the potential of $MoS_2$ to enhance Raman scattering via chemical mechanism known as charge transfer (CT) [1], [4], [5]. Previous work focused on the chemical mechanism of Raman enhancement of CuPc based on the monolayer $MoS_2$ [1], [5]. In our experiment copper phtalocyanine (CuPc) deposited on a bulk $MoS_2$ substrate worked as the probe molecule. Raman spectroscopy is well suited for chromophore molecules like CuPc, in which charge transfer (CT) of copper atoms within the phthalocyanine complex contributes to strengthening Raman signals of the Cu-N stretching bond. Besides, Local field enhancement via the electromagnetic mechanism provides a remarkable enhancement of Raman signals which are proportional to the fourth power of the field [7, 19].

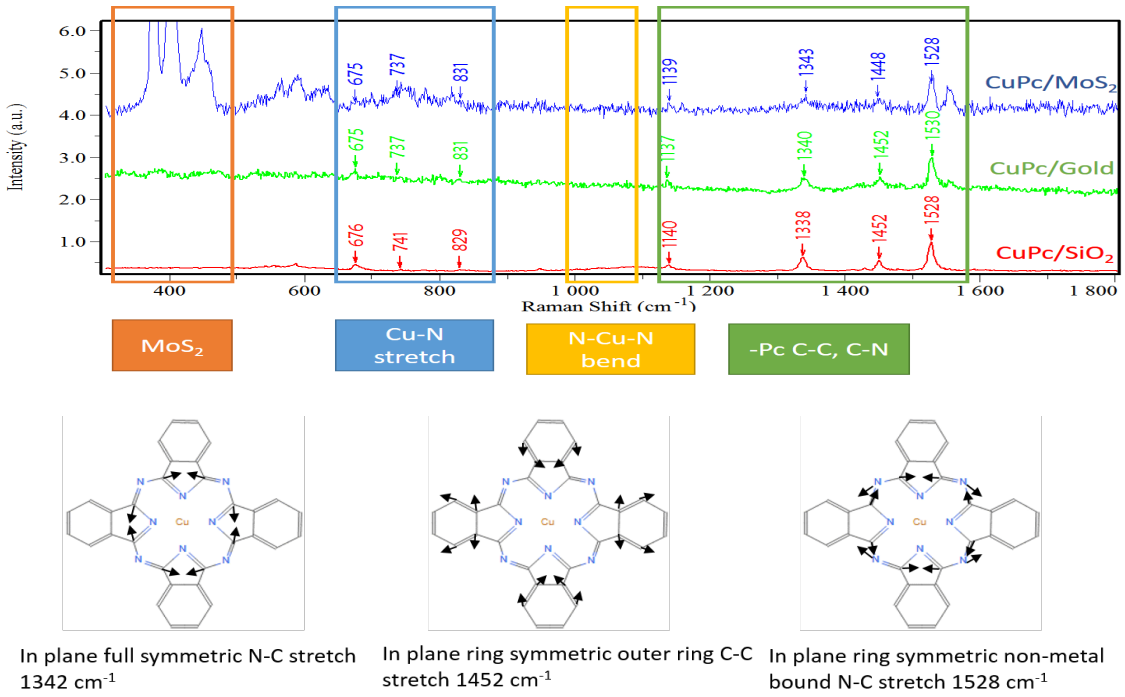


**Figure 2.2 Surface-enhanced Raman scattering (SERS) spectra of CuPc molecules on different substrates: $MoS_2$ (blue), gold (green), and $SiO_2$ (red). The spectra have been normalized and shifted for convenience. The peaks within the yellow part are not marked because of weak intensities. On the bottom, vector diagrams of three main molecular vibrations (1342 $cm^{-1}$, 1452 $cm^{-1}$, 1528 $cm^{-1}$) are shown.**

### 2.1.3. Chemical mechanism

Chemical interaction like charge transfer between CuPc and $MoS_2$ happens at the few layers around the junction. During this process intensity of bonds may change while new bonds may be generated. Thus, Raman signals corresponding to different molecular vibrations may vary. By comparing peak ratios in normalized spectra of CuPc on different substrates, we could see the surficial effects to different chemical bonds. A same method

was used to examine the TERS other than the measurement of enhancement factors to find the tip's specific effects to molecular bonds of CuPc.

**2.2. Materials and Methods**

The experimental scheme is shown in Fig. 2.1 CuPc molecules were deposited on bulk MoS2, gold and SiO2 substrates under identical conditions. The sample is placed on a horizontal X-Y translation stage. A silicon AFM cantilever (Nanonics) with a gold nanosphere tip of 200 nm diameter was used for the TERS experiments. The tip worked in the AFM tapping mode and the gap distance between the tip apex and the sample was less than 10 nm.

Previous work on resonance Raman spectroscopy of CuPc molecules was performed using the 632.8 nm Laser [1]. However, resonance Raman scattering was accompanied by strong fluorescence background which perturbed observation and analysis of Raman signals. We used a 532 nm laser for non-resonance Raman scattering to avoid the fluorescence background. The Laser beam was focused onto a sample through a $50\times$ objective.

The gold nanosphere tip supplies an enhanced localized focal spot in the near-field area $A_{NF} \approx \pi\left(\frac{d_{tip}}{2}\right)^2$, which is equal to 0.031 $\mu m^2$. Compared with the far-field, which is 0.055 $\mu m^2$, $A_{EF} \approx \pi\left(\frac{\lambda}{4}\right)^2$ [12] given by the Gaussian Laser beam, the near-field spatial resolution is approximately 1.33 times higher. Moreover, the effective TERS area is smaller than the enhanced field of which the approximate radius is half of the tip's [13, 14].

**Table 2.1 Peak assignment of Raman spectra. Peak assignment [6, 8] of Raman spectra in Fig. 2.2 The CuPc sample is deposited on three different substrates (a) $MoS_2$, (b) Gold and (c) $SiO_2$.**

| CuPc/$MoS_2$ ($cm^{-1}$) | CuPc/Gold ($cm^{-1}$) | CuPc/$SiO_2$ ($cm^{-1}$) | $I_{MoS_2}$ No tip | $I_{MoS_2}$ tip | $I_{Gold}$ No tip | $I_{Gold}$ tip | $I_{SiO_2}$ No tip | $I_{SiO_2}$ tip | Bonds |
|---|---|---|---|---|---|---|---|---|---|
| 377 | | | 14.39 | 0.17 | | | | | $E^1_{2g}$ ($MoS_2$) |
| 403 | | | 28.13 | 0.35 | | | | | $A_{1g}$ ($MoS_2$) |
| 675 | 675 | 676 | 0.21 | 0.23 | 0.37 | 0.28 | 0.22 | 0.28 | In plane full symmetric nonmetal bound N-Cu stretch and outer ring stretches |
| 737 | 737 | 741 | 0.51 | 0.13 | 0.18 | 0.12 | 0.07 | 0.12 | In plane ring symmetric N-Cu stretch |
| 831 | 831 | 829 | 0.36 | 0.07 | 0.19 | 0.06 | 0.05 | 0.06 | In plane full symmetric N-Cu stretch |
| 1139 | 1137 | 1140 | 0.33 | 0.22 | 0.37 | 0.25 | 0.22 | 0.26 | In plane ring symmetric and outer ring breathing |
| 1343 | 1340 | 1338 | 0.46 | 0.45 | 0.43 | 0.42 | 0.48 | 0.40 | In plane full symmetric N-C stretch and ring C-C Stretch |
| 1452 | 1452 | 1452 | 0.37 | 0.32 | 0.45 | 0.33 | 0.36 | 0.30 | In plane ring symmetric outer ring C-C stretch |
| 1528 | 1530 | 1528 | 1 | 1 | 1 | 1 | 1 | 1 | In plane ring symmetric non-metal bound N-C stretch |

## 2.3. Substrate effects of $MoS_2$, gold and $SiO_2$

We obtained Raman spectra of CuPc molecules in the condition of surface enhancement on three substrates. $MoS_2$ provides near-field effects to Raman scattering through energy and charge transfer based on light induced electron-hole pairs [5]. New bonds generation may take place at the junction between the CuPc molecules and $MoS_2$. Energy transfer also occurs due to recombination of electron-hole pairs. On the other hand, gold surface provides enhancement for Raman scattering mainly through the surface plasmon induced electromagnetic field [9]. Coupling of CuPc molecular vibration bonds and surface plasmons changes the density and energy of vibrations. We also investigated $SiO_2$ substrate for comparison because of its negligible SERS effects.

The non-resonant Raman spectrum excited by 532 nm laser is compared with a resonant Raman signal by 632 nm laser [1], which focused on a few-layer CuPc/$MoS_2$ sample. On the other hand, our work is based on about 5 to 10 layers CuPc film (30nm thick) [20] and bulk-size $MoS_2$. Without baseline correction, non-resonant Raman (blue)

shows less fluorescence while the resonant Raman signals are nearly overwhelmed by an inevitable fluorescence background.

Fig. 2.2 shows representative Raman spectra of three different samples with an incident laser power 0.05W and acquisition time of 60 s. The spectra were processed by normalization to the maximum intensity of the CuPc signal (1528 $cm^{-1}$). Marked peaks in Fig. 2.2 represent CuPc molecular vibrations in the range from 675 $cm^{-1}$ to 1530 $cm^{-1}$, where according to Table 1, Raman signals around 675, 737, and 831 $cm^{-1}$ (blue) correspond to Cu-N stretch bonds and 1139, 1343, 1448, 1528 $cm^{-1}$ (green) stand for non-metal phthalocyanine bonds. Though inapparent without tip enhancement, peaks at 948, 1105 $cm^{-1}$ (yellow) correspond to metal involved bending. Raman signals at 377 $cm^{-1}$ and 403 $cm^{-1}$ (orange) are attributed to the bulk $MoS_2$.

Table 1 shows peak assignment and the normalized intensities (peak ratios) of the three SERS spectra in Fig. 2.2 The Raman spectrum of CuPc indicates that the bonds related to the vibrations involving central metal atoms are of lower frequency compared with the non-metal vibrations. The peak ratios in three non-TERS lists show that compared to $SiO_2$ whose surface enhancement effects are ignorable, CuPc/$MoS_2$ made differences to the in-plane ring/full symmetric N-Cu stretch (737 $cm^{-1}$, 831 $cm^{-1}$), while CuPc/Gold made differences to all the listed bonds except the in-plane full symmetric N-C stretch and ring C-C stretch (1340 $cm^{-1}$).

Table 1 also list the peak ratios of TERS with the three same samples, in which same peaks of three samples are of less difference compared to the non-tip case. In the presence of CuPc/$MoS_2$, the exponentially decreasing electromagnetic field near the tip

results in more effects to CuPc and less to the substrate. The near-field volume is roughly estimated as $10\ \text{nm} \times \pi \left(\frac{d_{tip}}{2}\right)^2$, where the 10 nm is found as the penetration depth of the local electric field [12]. The Raman signal of $MoS_2$ is slightly reduced due to the shadowing effect of the tip. On another hand, the CuPc Raman signal is enhanced since it was covered by the TERS effective area. The same situation happened to the other two substrates, where SERS were shadowed and overwhelmed by relatively strong TERS signal.

Fig. 2.3 shows SERS (blue) and TERS (red) spectra. CuPc/$MoS_2$ TERS reveals apparent enhancement to CuPc signals but suppression to the signal of $MoS_2$. These effects are due to the gap-mode TERS as discussed below. Table 2 lists enhancement factor (EF) [12], [15], [16]. Judging from enhancement factors in Table 2, TERS of CuPc/Gold shows averagely strongest enhancement among three samples, then CuPc/$MoS_2$, and CuPc/$SiO_2$ displays weakest tip enhancement.

Then by comparing the enhancement factors of different molecular vibrations, an interesting observation is that the tip enhancement is stronger for the full symmetric nonmetal bound N-Cu stretch and outer ring stretches (676 $cm^{-1}$), non-metal C-C and N-C bonds (1139 $cm^{-1}$, 1340 $cm^{-1}$, 1450 $cm^{-1}$, 1527 $cm^{-1}$) rather than in-plane ring/full symmetric N-Cu stretch (742 $cm^{-1}$, 829 $cm^{-1}$) and in-plane diag symmetric N-Cu-N bend bonds (948 $cm^{-1}$, 1105 $cm^{-1}$) of CuPc molecules. In all three cases, TERS effects to metal involved bending bonds are weak. As to the TERS of phthalocyanine bonds, only CuPc/$MoS_2$ and CuPc/Gold demonstrated notable enhancement.

Generally speaking, as to the CuPc/$MoS_2$ and CuPc/Gold samples, the enhancement effects for the three classified vibrations is non-metal bonds (green) > Cu-N stretch bonds (blue) > N-Cu-N bending bonds (yellow). For the CuPc/$SiO_2$, vibrations related to non-metal bonds (green) are quite comparable to that of symmetric N-Cu stretch (blue).

### 2.4. Enhancement mechanisms of $MoS_2$ and gold substrates

In our experiment the fluorescence background was absent due to non-resonant excitation. In the previous work, 632 nm laser was used for resonance Raman spectroscopy. [1]

When the CuPc probe molecules are deposited on substrates, the coupling at the interface may contribute to changes of Raman signal. In the case of $MoS_2$, the main mechanism to modify Raman signal intensity of CuPc is by charge transfer (CT) near the interface junction [1], [5]. Light induced charge carriers such as electron-hole pairs could be delocalized and transfer to adjacent materials, which potentially changes the intensity of certain bonds involved in redox reaction. In our case, metal involved bonds provide ions for redox reaction. [21] Therefore, according to the "CuPc/$MoS_2$ non-tip" columns in Table 1, peak ratios of in-plane ring/full symmetric N-Cu stretch at 737 $cm^{-1}$ and 831 $cm^{-1}$ is particularly changed compared to CuPc/$SiO_2$. The changes depend on the density of charge carriers and probability of charge transfer between CuPc molecules and the $MoS_2$ surface.

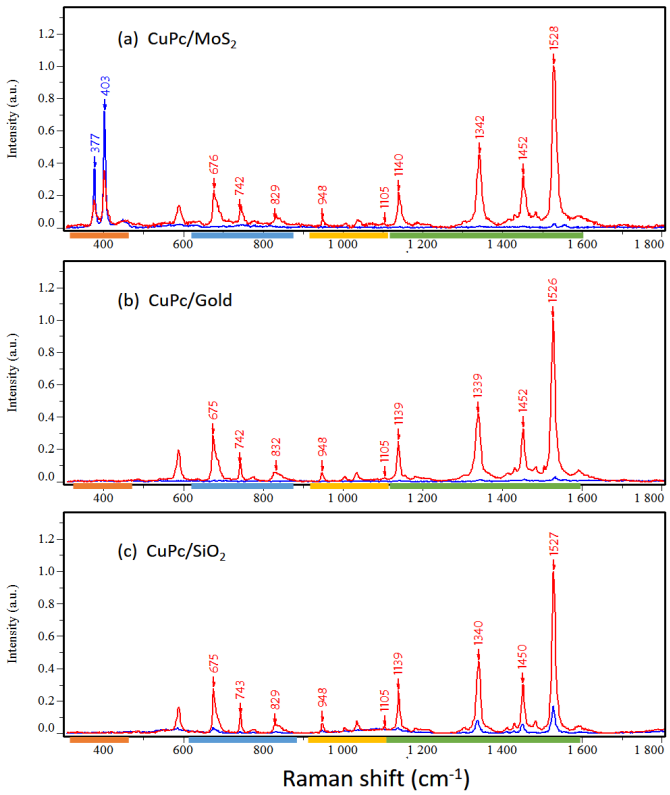


**Figure 2.3 Tip enhanced Raman scattering (TERS) spectra of CuPc molecules film on (a) $MoS_2$ (b) gold, and (c) $SiO_2$ substrates. All the spectra are normalized to the maximum intensity for convenience. Raman spectra without (blue) and with (red) tip correspond to normal Raman and TERS respectively. Enhancement factors analysis of these spectra is listed in Table 2.**

On the other hand, the SERS effects of the gold substrate are mainly attributed to the local surface plasmonic field. The molecular vibrations of CuPc would be coupled to the light induced surface plasmon modes and get enhanced [18]. According to Table 1, gold surface changed the peak ratios of all the marked signals other than in-plane full symmetric N-C stretch and ring C-C stretch (1340 $cm^{-1}$). Different from $MoS_2$, gold

surface didn't show particular enhancement to some certain vibration modes of CuPc molecules but impacted both metal and non-metal vibrations.

**Table 2.2 TERS enhancement factors (EFs). TERS EFs were estimated using the following procedure: $EF_{TERS} = \left(\frac{I_{NF}}{I_{FF}} - 1\right)\frac{A_{FF}}{A_{NF}}$ [7] after removing background by polynomial baseline correction. $I_{NF}$ and $I_{FF}$ represent the spectral intensity with the tip in contact with CuPc (near field) and retracted from the sample surface (far field). $A_{FF}$ and $A_{NF}$ stand for the area sizes of laser confocal spot and the tip's, whose value are approximately given by $\pi\left(\frac{\lambda}{4}\right)^2$ and $\pi\left(\frac{d_{tip}}{2}\right)^2$. $d_{tip} = 200\ nm$, $\lambda = 532\ nm$.**

| CuPc/$MoS_2$ $cm^{-1}$ | CuPc/Gold $cm^{-1}$ | CuPc/$SiO_2$ $cm^{-1}$ | $EF_{MoS2}$ | $EF_{Gold}$ | $EF_{SiO_2}$ | Bonds |
|---|---|---|---|---|---|---|
| 378 | | | -0.92 | | | $E^1_{2g}$ ($MoS_2$) |
| 402 | | | -0.49 | | | $A_{1g}$ ($MoS_2$) |
| 676 | 675 | 675 | 38.65 | 55.37 | 11.50 | In plane full symmetric nonmetal bound N-Cu stretch and outer ring stretches |
| 742 | 742 | 742 | 12.66 | 35.15 | 15.22 | In plane ring symmetric N-Cu stretch |
| 829 | 832 | 829 | 12.84 | 22.51 | 7.25 | In plane full symmetric N-Cu stretch |
| 948 | 948 | 948 | 3.27 | 13.32 | 4.32 | In plane diag symmetric N-Cu-N bend and N-Cu stretch |
| 1105 | 1105 | 1105 | 8.81 | 7.98 | 0.48 | In plane diag symmetric N-Cu-N bend |
| 1140 | 1139 | 1139 | 49.89 | 57.12 | 10.77 | In plane ring symmetric and outer rings breathing |
| 1342 | 1339 | 1340 | 60.29 | 69.76 | 13.58 | In plane full symmetric N-Cstretch and ring C-C Stretch |
| 1452 | 1452 | 1450 | 54.02 | 45.26 | 7.09 | In plane ring symmetric outer ring C-Cstretch |
| 1528 | 1526 | 1527 | 67.59 | 98.98 | 8.84 | In plane ring symmetric non-metal bound N-Cstretch |

TERS effects on peak ratios were also investigated which were almost same when the tip approached to the sample. Because the localized surface plasmon on the gold tip can be used to focus the incident light under identical conditions. Strong Raman signal enhancement occurs with close distance of the gold tip and CuPc film. Since the penetration depth of the effective field of the tip was about 10 nm that was less than the average thickness of CuPc film (30nm), the enhancement wouldn't influence the substrate as much as the CuPc film. Thus, the scattered light didn't contain so much substrate information as before. From peak ratios in the condition of TERS in Table 1, the

contribution of substrates we discussed above had been overwhelmed by the tip enhancement. The conventional SERS effects may be ignorable during the TERS experiment except for the case of tip-substrate interaction, which was investigated through enhancement factors.

The enhancement factor (EF) is a useful measure of the performance of enhanced Raman scattering [7], [12], [16]. As we discussed above, the SERS effects could be ignored during the TERS experiments. However, there is an exception for the gold substrate, which contains free electrons and leads to tip-substrate coupling and gap-mode TERS [10, 11].

**2.5. Conclusion**

In conclusion, using non-resonant Raman scattering to study CuPc molecules on different substrate $MoS_2$, gold and $SiO_2$ could remove the disturbance of fluorescence. Investigation of peak ratios give us information that under the condition of the $MoS_2$ substrate in-plane symmetric Cu-N stretches of CuPc are mostly influenced and the gold substrate impacts most bonds. Moreover, tip enhanced Raman scattering overwhelms the effects of substrate in accordance with the similar peak ratios whatever substrate is used. However, by comparing the enhancement effects of TERS among the same three substrates, we found that the enhancement effects are ranked by Gold>$MoS_2$>>$SiO_2$, which implies that interaction between the gold tip and the substrate has to be considered in the case of gold and $MoS_2$. Furthermore, results of TERS experiment shows that enhancement factors of non-metal bonds and symmetric Cu-N stretches are larger than N-

Cu-N bends. With gold and $MoS_2$ substrates, the enhancement effects of non-metal bonds are generally stronger than it of metal involved bonds.

**2.6. References**


1. X. Ling et al., "Raman enhancement effect on Two-Dimensional layered materials: Graphene, h-bN and MoS2," *Nano Letters*, vol. 14, no. 6, pp. 3033–3040, 2014.

2. C. Lee, H. Yan, L. E. Brus, T. F. Heinz, J. Hone, and S. Ryu, "Anomalous lattice vibrations of single- and few-layer moS 2," *ACS Nano*, vol. 4, no. 5, pp. 2695–2700, 2010.

3. K. Gołasa et al., "Resonant Raman scattering in moS2—From bulk to monolayer," *Solid State Communications*, vol. 197, pp. 53–56, 2014.

4. X. Zhu, N. R. Monahan, Z. Gong, H. Zhu, K. W. Williams, and C. A. Nelson, "Charge transfer Excitons at van der Waals interfaces," *Journal of the American Chemical Society*, vol. 137, no. 26, pp. 8313–8320, 2015.

5. X. Ling, L. G. Moura, M. A. Pimenta, and J. Zhang, "Charge-transfer mechanism in Graphene-Enhanced Raman scattering," *The Journal of Physical Chemistry C*, vol. 116, no. 47, pp. 25112–25118, 2012.

6. N. Jiang et al., "Observation of multiple Vibrational modes in Ultrahigh vacuum tip-enhanced Raman spectroscopy combined with molecular-resolution scanning Tunneling microscopy," *Nano Letters*, vol. 12, no. 10, pp. 5061–5067, 2012.

7. N. Kumar, S. Mignuzzi, W. Su, and D. Roy, "Tip-enhanced Raman spectroscopy: Principles and applications," EPJ Techniques and Instrumentation, vol. 2, no. 1, 2015. 8.

M. Xia et al., "Spectroscopic signatures of AA′ and AB stacking of chemical vapor deposited Bilayer MoS2," *ACS Nano*, vol. 9, no. 12, pp. 12246–12254, 2015.

9. J. R. Ferraro, Introductory Raman spectroscopy. United States: Academic Press, 2014.

10. Z. Yang, J. Aizpurua, and H. Xu, "Electromagnetic field enhancement in TERS configurations," *Journal of Raman Spectroscopy*, vol. 40, no. 10, pp. 1343–1348, 2009.

11. Y. Zhang et al., "Improving resolution in quantum subnanometre-gap tip-enhanced Raman nanoimaging," *Scientific Reports*, vol. 6, p. 25788, 2016.

12. N. Kumar, A. Rae, and D. Roy, "Accurate measurement of enhancement factor in tip-enhanced Raman spectroscopy through elimination of far-field artefacts," *Applied Physics Letters*. vol. 104, no. 12, p. 123106, 2014.

13. J. Steidtner and B. Pettinger, "Tip-enhanced Raman spectroscopy and microscopy on single dye molecules with 15 nm resolution," *Physical Review Letter*s. vol. 100, no. 23, 2008.

14. K. F. Domke, D. Zhang, and B. Pettinger, "Toward Raman fingerprints of single dye molecules at Atomically smooth au(111)," *Journal of the American Chemical Society*, . vol. 128, no. 45, pp. 14721–14727, 2006.

15. B. Pettinger, B. Ren, G. Picardi, R. Schuster, and G. Ertl, "Tip-enhanced Raman spectroscopy (TERS) of malachite green isothiocyanate at au(111): Bleaching behavior under the influence of high electromagnetic fields," *Journal of Raman Spectroscopy*, . vol. 36, no. 6-7, pp. 541–550, 2005.

16. B. Pettinger, P. Schambach, C. J. Villagómez, and N. Scott, "Tip-enhanced Raman spectroscopy: Near-fields acting on a few molecules," *Annual Review of Physical Chemistry*, vol. 63, no. 1, pp. 379–399, 2012.

17. B. J. Palys, D. M. W. van den Ham, W. Briels, and D. Feil, "Resonance Raman spectra of phthalocyanine monolayers on different supports. A normal mode analysis of zinc phthalocyanine by means of the MNDO method," *Journal of Raman Spectroscopy*, vol. 26, no. 1, pp. 63–76, 1995.

18. B. Sharma, R. R. Frontiera, A.-I. Henry, E. Ringe, and R. P. Van Duyne, "SERS: Materials, applications, and the future," *Materials Today*, vol. 15, no. 1-2, pp. 16–25, 2012.

19. Z. Zalevsky. “Integrated nanophotonic devices”. *Elsevier*, 2014.

20. T. V. Basova, V. G. Kiselev, B.-E. Schuster, H. Peisert, and T. ChassÃ©, "Experimental and theoretical investigation of vibrational spectra of copper phthalocyanine: Polarized single-crystal Raman spectra, isotope effect and DFT calculations," *Journal of Raman Spectroscopy*, vol. 40, no. 12, pp. 2080–2087, 2009.

21. P. Myers, "Subrayal M. Reddy (Ed): Advanced synthetic materials in detection science," *Chromatographia*, vol. 78, no. 3-4, pp. 299–300, 2014.

22. Z. Zalevsky, "Integrated micro- and nanophotonic dynamic devices: A review," *Journal of Nanophotonics*, vol. 1, no. 1, p. 012504, 2007.

23. M. Scalora, M. A. Vincenti, D. de Ceglia, M. Grande, and J. W. Haus, "Raman scattering near metal nanostructures," *Journal of the Optical Society of America B*, vol. 29, no. 8, p. 2035, 2012.

24. M. Warner et al., "Potential for spin-based information processing in a thin-film molecular semiconductor," *Nature*, vol. 503, no. 7477, pp. 504–508, 2013.

# 3. TIP-ENHANCED RAMAN IMAGING OF SINGLE-STRANDED DNA WITH SINGLE BASE RESOLUTION[*]

Tip-enhanced Raman scattering (TERS) is a promising optical and analytical technique for chemical imaging and sensing at single molecule resolution. [1] In particular, TERS signals generated by a gap-mode configuration where a silver tip is coupled with a gold substrate can resolve a single-stranded DNA (ssDNA) molecule with a spatial resolution below 1 nm. To demonstrate the proof of sub-nanometer resolution, we show direct nucleic acid sequencing using TERS of a phage ssDNA (M13mp18). M13mp18 provides a known sequence and, through our deposition strategy, can be stretched (uncoiled) and attached to the substrate by its phosphate groups, while exposing its nucleobases to the tip. After deposition, we scan the silver tip along the ssDNA and collect TERS signals with a step of 0.5 nm, comparable to the bond length between two adjacent DNA bases. By demonstrating the real-time profiling of a ssDNA configuration and furthermore, with unique TERS signals of monomeric units of other biopolymers, we anticipate that this technique can be extended to the high-resolution imaging of various nanostructures as well as the direct sequencing of other important biopolymers including RNA, polysaccharides, and polypeptides.

---

[*] Reprinted/adapted with permission from "Tip-enhanced raman imaging of single-stranded DNA with single base resolution" by He, Z., Han, Z., Kizer, M., Linhardt, R. J., Wang, X., Sinyukov, A. M., ... & Scully, M. O., 2018. *Journal of the American Chemical Society*, *141*(2), 753-757, Copyright 2019 by American Chemical Society

## 3.1. Introduction

### 3.1.1. Single molecule imaging by tip-enhanced Raman scattering (TERS)

Tip-enhanced Raman scattering (TERS) provides an effective technique at the forefront of the chemical imaging. TERS can effectively enhance Raman signals by localized plasmon resonance on a nanoscale tip, increasing Raman signals by a factor of $10^6$. [2, 3] In addition, the near-field effects caused by nanoscale tips overcome the optical diffraction limit to allow high-resolution imaging of target molecules. Previous studies illustrated that TERS enables a resolution of near or less than 1 nm under ambient and cryogenic conditions for both STM and AFM based systems, [4–9] which may be due to the localization effects of atomic-scale structures on tips. [10,11] Furthermore, the gap-mode configuration generated in the plasmonic cavity formed between the silver tip and the gold substrate can further boost the enhancement factor of TERS to $10^{13}$-fold within the gap. [12] These advantages make TERS an ideal technique for chemical identifications of single molecules.

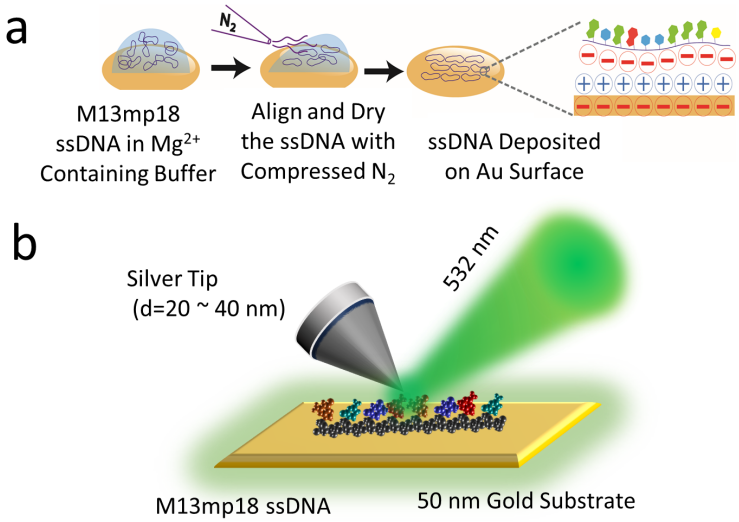


**Figure 3.1 (a) The DNA deposition method. we used forced-air to align the ssDNA on the gold surface to stretch the DNA for evading/minimizing DNA coiling during the deposition. Furthermore, we added $Mg^{2+}$ cations in the DNA buffer solution (pH 7.5) during the deposition to preferentially facilitate the adhesion of highly negatively-charged DNA phosphate backbone to negatively-charged gold surface. This will help to maximize the exposure of nucleobases to AFM tips for the downstream sensing and sequencing. Each '+' sign indicates a $Mg^{2+}$ ion, and '-' sign indicates the negative charge carried by DNA phosphate backbone or the gold surface. (b) Schematic for tip-enhanced Raman scattering of ssDNA molecules. The diameter of the silver tip is 20 to 40 nm. An objective (100X, NA 0.7) focuses the 532 nm incidence light on the tip at 45°. TERS signals are collected by the same objective. Gap-mode TERS is formed by reducing tip-substrate distances to less than 1 nm.**

### 3.1.2. Deoxyribonucleic acid (DNA) sequencing

Deoxyribonucleic acid (DNA) is an essential and information-rich biological molecule carrying the genetic information of all living organisms. The DNA molecule contains a linear sequence encoded by four nucleobases with prominently different Raman signals which provide a powerful tool for the determination of DNA nucleobase sequences. [13,14] To date, heroic progress has been made in single molecule sequencing (SMS).

Among this progress, a nanopore-based sequencing method, a representative of the third-generation sequencing methods that focus on single molecule sequencing (SMS), is limited by the incredibly short dwell times of DNA in the nanopore and the poor resolution of the individual nucleobase signals, [15,16] resulting in sequencing errors. As a technology of high-resolution imaging, TERS provides an alternative application to analyze nucleobases without requiring the amplification of nucleic acids or labeled reagents and is not limited by the same factors that limit nanopore technology. So far, TERS has been demonstrated capable of distinguishing nucleobases [13,17] as well as enabling the exploration of DNA sensing, [18,19] hydrogen bonds [20] and aggregation effects [21]. For pure nucleic acids, a spatial resolution of 0.9 nm was obtained by using TERS to scan across the boundary of pure nucleobase networks. [17] A practical solution for reading nucleotides sequences along DNA bundles requires DNA with very simple sequences and careful scans along a DNA strand. [1]

### 3.1.3. DNA imaging and sequencing by TERS

Although TERS can distinguish individual nucleobases, imaging the single ssDNA molecule remains very challenging since stable alignment of the single DNA molecule is difficult and required to read non-overlapping nucleotides. As further elaborated below, in this report for the first time we have demonstrated the success of single ssDNA imaging and using TERS to directly sequence multiple segments of the known M13mp18 bacteria phage ssDNA with at least 90% accuracy. Our success relies on (1) TERS imaging that leads to mapping DNA molecules and identifying sequences with a single-base resolution

and (2) a unique DNA deposition method we have developed for effectively minimizing DNA coiling as well as maximizing the exposure of nucleobases to the AFM tips.

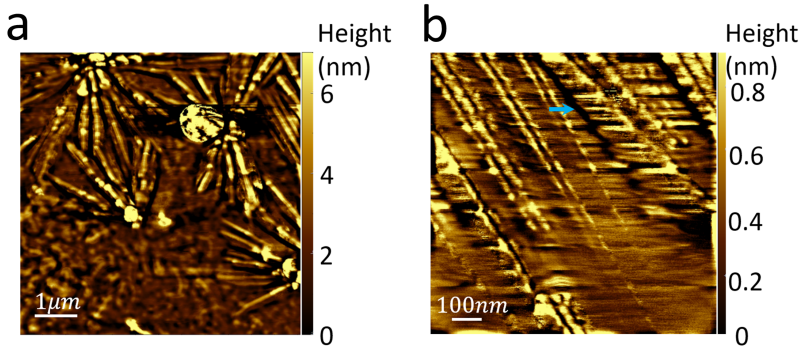


**Figure 3.2 DNA sensing by AFM. (a) AFM image of DNA clusters and (b) a zoom-in image of the red dash-line squared region in (a).**

### 3.2. Method

We show a tapping-mode AFM image in Fig. 3.2 and estimate the thickness of a ssDNA strand at approximately 0.6 nm. Since the thickness of the M13mp18 ssDNA was reported to be $0.3 \pm 0.1$ nm, [22] it is reasonable to assume that this represents a planar bundle of one to two nucleobase height. However, it is noted that AFM cannot precisely measure the width of a ssDNA molecule because its lateral resolution is limited by the tip broadening effects.

#### 3.2.1. Spatial resolution of TERS and AFM

Compared to AFM, TERS provides a superior, sub-nanometer resolution of the bundle edges. We performed a TERS scan along the blue arrow as indicated in Fig. 3.2b

with a step size of 0.5 nm. We set the acquisition time as 4 s to attenuate the effects of spectral fluctuations for achieving stable measurements. Shown by the red curve in Fig. 3.3a, the integrated intensities of the Raman signal peaks from 1630 cm-1 to 1650 cm-1 can refer to DNA nucleobases cytosine (C), guanine (G) and thymine (T). The width of the DNA bundle is estimated to be 2.5 nm. Similarly, in Fig. 3.4a, we imaged the sample based on the same peaks. The high contrast map highlights a single DNA strand (spot 1 to 24). Moreover, the one-step spectral changes from the red to blue parts in Fig. 3.3b and the distinguishable on-strand and off-strand signals in Fig. 3.4b prove that TERS was able to reach a spatial resolution of 0.5 nm.

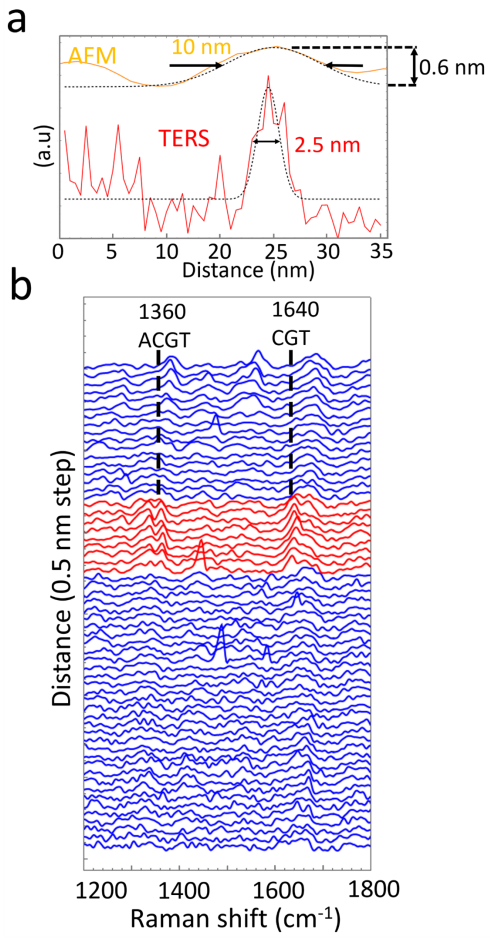


**Figure 3.3 (a) AFM (yellow) and TERS (red) signals collected along the blue arrow in Fig. 3.2b. We use AFM and TERS to estimate the width of a DNA bundle. The AFM curve exhibits a full-width at half-maximum (FWHM) of 10 nm based on a Gaussian fitting. The TERS curve, which is the integrated intensity of the Raman signal from 1630 $cm^{-1}$ to 1650 $cm^{-1}$, exhibits a FWHM of 2.5 nm, far narrower than AFM. (b) TERS spectra taken along the blue arrow in Fig. 3.2b. The scanning step is 0.5 nm. The red curves represent the spectra on the DNA bundle.**

### 3.2.2. Scanning step of TERS

In this study, we chose the scanning step of 0.5 nm to be comparable to the base-to-base distance, which was reported as 0.4 nm to 0.6 nm. [23–25] A choice of step size

larger than 0.6 nm would be inadequate for sequence mapping. In contrast, a step size smaller than 0.4 nm can lead to difficulties in distinguishing homogeneous sequences such as 'AAAAA' from 'AAAA'. Moreover, when the step size is comparable to the base interval, the tip apex could possibly "push" nucleobases and rearrange these at each step. Although the distances between bases are initially varied due to the random rotation of nucleotides, the tip may shift them to a certain degree, so that these distances become approximately equal to the step size of TERS scanning, which may lead to the capability of detecting one base in one step. Moreover, DNA strands were possibly pushed by the tip apex and showed themselves as a line along the horizontal direction. It has been reported that the AFM tip, operating in the contact mode, can move carbon nanotubes. [26] In our case, although the AFM was operated in the tapping mode, the TERS scanning could resemble a contact procedure and realign the strands. Meanwhile, since the vibration frequency of the cantilever is close to the oscillation resonance, the tip will still perform strong tapping force towards the ssDNA molecules. [27] The lateral pressure may also cause the ssDNA realignment.

### 3.2.3. TERS peak assignment of DNA nucleobases

We then identify the characteristic peaks of each nucleobase used to identify the nucleobases sequences. Summarized in Appendix Table A1, Raman peaks at 735 to 737 $cm^{-1}$ (A1), 1467 to 1492 $cm^{-1}$ (A2), 799 to 801 $cm^{-1}$ (C1), 1235 to 1270 $cm^{-1}$ (C2), 954 to 958 $cm^{-1}$ (G1), 1545 to 1554 $cm^{-1}$ (G2), and 778 to 782 $cm^{-1}$ (T1), 1366 to 1373 $cm^{-1}$ (T2) are utilized to distinguish adenine (A), cytosine (C), guanine (G) and thymine (T). [1,13,28–31] Four spectral references were

then built according to the modes A1, A2, C1, C2, G1, G2, T1 and T2 (Fig. A3). Moreover, Fig. A4 and Fig. A5 display these identifiable modes in our measurement. Baseline correction by a third order polynomial fitting was applied to TERS spectra. The linear correlation between the scanning spectra and the templates was based on the discrete Pearson correlation function. [32] The normalized correlation coefficient can be found to evaluate probabilities $P_i$ of four nucleobases. As described below, repeating the calculations (see Supporting information) for all spots, we determined the sequences of each scanned DNA segment. Then, by comparing these data with the actual sequence of M13mp18 DNA through approximate string matching, [33] we proved the credibility of our TERS sequencing results.

**3.3. DNA sequencing**

Identified DNA sequences are shown in Fig. 3.4c and Fig. 3.4d. We used the same tip as in Fig. 3.3. Since interferences of adjacent bases result in multi-component signals, we label the most possible bases below the bar charts. The multi-component spectrum occurs due to the interference of adjacent bases. Mistakes may happen when the surrounding signals overwhelm the target base. Therefore, in Fig. 3.4c, spot 7 and spot 11 were misread due to the strong signals of guanine and thymine. The accuracy shown in Fig. 3.4c is 91.7% (22/24). Six repeated measurements in Fig. A1 and Table A2 show the sequencing accuracy, using different tips and different deposited samples, is better than 90.9%.

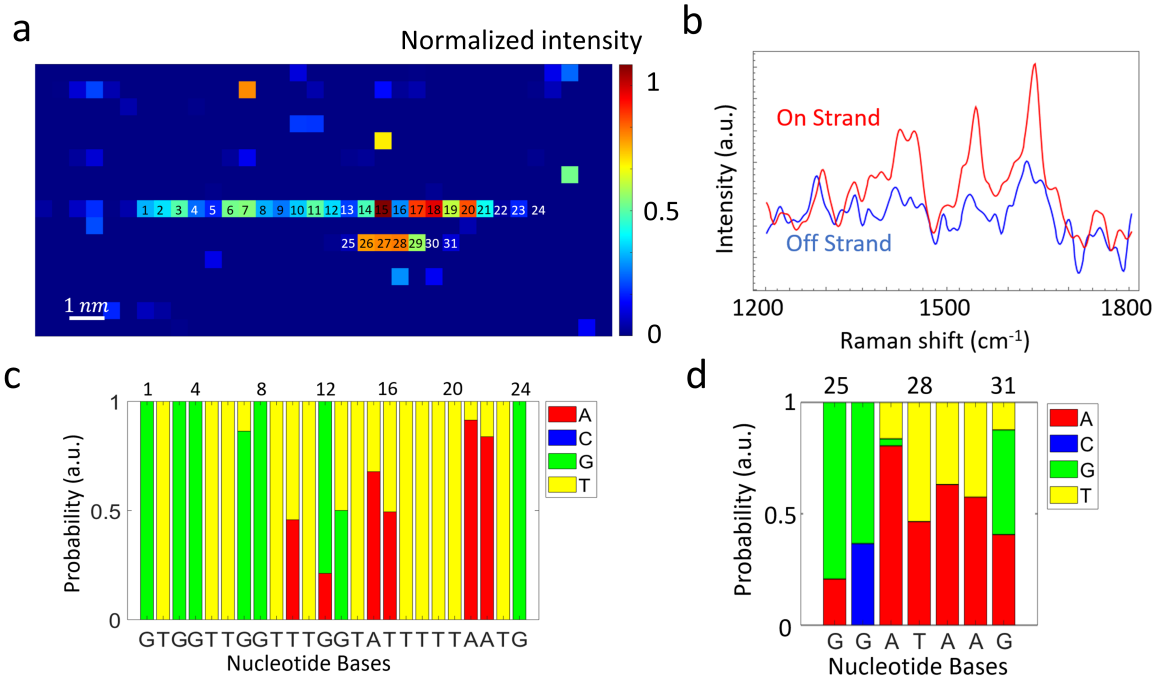


**Figure 3.4 DNA sequencing of sample 1 containing 1.0 pmol of M13mp18 DNA. (a) TERS image of a single ssDNA segment with a step size of 0.5 nm. The acquisition time for each step is 4 s. The plots show the integral intensities of the spectrum from 1630 $cm^{-1}$ to 1650 $cm^{-1}$. The numbers marking the map indicate the order of the sequences. (b) The "on strand" TERS spectrum of the pixel 7 and the "off strand" spectrum one step above the pixel 7 in (a). The substantial difference proves the 0.5 nm resolving capacity along the cross section. (c) A bar chart shows the probabilities $P_i$ from the spot 1 to 24 labeled in (a). The most probable bases are labeled at the bottom. Compared to the real DNA sequence GTGGTTCGTTCGGTATTTTTAATG, two errors are found at the spot 7 (G→ C) and spot 11 (T → C). (d) The probabilities $P_i$ from the spot 25 to 31. Two strands in (a) are 1 nm separated. The different sequences of spots 13 to 19 and spots 25 to 31 provides an evidence that TERS imaging can distinguish two parallel DNA molecules only separated by 1 nm.**

To prove that the measured sequences of each segment truly matched the actual M13mp18 sequence, we constructed a random 24-base trial sequence as a comparison and applied approximate string-matching algorithm for 10 million times. Under the best matching conditions between a 24-base random sequence and any 24-base long segment

of M13mp18, the average number of mismatching errors was 9.4. The probability of 2 errors for a random trial is less than 1/10,000,000. The distribution of mismatching errors for trials using random sequences are shown in Fig. A2. This negligible probability proves that our sequencing result is authentic, and the sequence from spot 1 to spot 24 belongs to a specific fragment of the M13mp18 DNA. The similar comparison was repeated for each repeating result in Table A2.

### 3.4. Conclusion

In conclusion, by displaying ssDNA imaging and sequencing at room temperature, we have demonstrated the sub-nanometer resolving ability of TERS and have shown the repeatability of using different tips and ssDNA molecules. As a straightforward optical sensing technique, TERS has the potential of becoming a next generation sequencing method for DNA/RNA as well as other important biological polymers such as polysaccharides, polypeptides, and even glyco-peptide conjugates.

### 3.5. References

1. Lin, Xiu-Mei, et al. "Direct base-to-base transitions in ssDNA revealed by tip-enhanced Raman scattering." *arXiv preprint arXiv:1604.06598* (2016).

2. T. Deckert-Gaudig, D. Kurouski, M. Hedegaard, P. Singh, I. Lednev and V. Deckert, "Spatially resolved spectroscopic differentiation of hydrophilic and hydrophobic domains on individual insulin amyloid fibrils", *Scientific Reports*, vol. 6, no. 1, 2016.

3. B. Pettinger, B. Ren, G. Picardi, R. Schuster and G. Ertl, "Nanoscale Probing of Adsorbed Species by Tip-Enhanced Raman Spectroscopy", *Physical Review Letters*, vol. 92, no. 9, 2004.

4. C. Chen, N. Hayazawa and S. Kawata, "A 1.7 nm resolution chemical analysis of carbon nanotubes by tip-enhanced Raman imaging in the ambient", *Nature Communications*, vol. 5, no. 1, 2014.

5. R. Zhang et al., "Chemical mapping of a single molecule by plasmon-enhanced Raman scattering", *Nature*, vol. 498, no. 7452, pp. 82-86, 2013.

6. T. Deckert-Gaudig, D. Kurouski, M. Hedegaard, P. Singh, I. Lednev and V. Deckert, "Spatially resolved spectroscopic differentiation of hydrophilic and hydrophobic domains on individual insulin amyloid fibrils", *Scientific Reports*, vol. 6, no. 1, 2016.

7. S. Jiang et al., "Distinguishing adjacent molecules on a surface using plasmon-enhanced Raman scattering", *Nature Nanotechnology*, vol. 10, no. 10, pp. 865-869, 2015.

8. D. Kurouski, T. Deckert-Gaudig, V. Deckert and I. Lednev, "Structure and Composition of Insulin Fibril Surfaces Probed by TERS", *Journal of the American Chemical Society*, vol. 134, no. 32, pp. 13323-13329, 2012.

9. M. Richard-Lacroix, Y. Zhang, Z. Dong and V. Deckert, "Mastering high resolution tip-enhanced Raman spectroscopy: towards a shift of perception", *Chemical Society Reviews*, vol. 46, no. 13, pp. 3922-3944, 2017.

10. S. Trautmann et al., "A classical description of subnanometer resolution by atomic features in metallic structures", *Nanoscale*, vol. 9, no. 1, pp. 391-401, 2017.

11. M. Urbieta et al., "Atomic-Scale Lightning Rod Effect in Plasmonic Picocavities: A Classical View to a Quantum Effect", *ACS Nano*, vol. 12, no. 1, pp. 585-595, 2018.

12. J. Marr and Z. Schultz, "Imaging Electric Fields in SERS and TERS Using the Vibrational Stark Effect", *The Journal of Physical Chemistry Letters*, vol. 4, no. 19, pp. 3268-3272, 2013.

13. R. Treffer, X. Lin, E. Bailo, T. Deckert-Gaudig and V. Deckert, "Distinction of nucleobases – a tip-enhanced Raman approach", *Beilstein Journal of Nanotechnology*, vol. 2, pp. 628-637, 2011.

14. Y. Cao, "Nanoparticles with Raman Spectroscopic Fingerprints for DNA and RNA Detection", *Science*, vol. 297, no. 5586, pp. 1536-1540, 2002.

15. J. Heather and B. Chain, "The sequence of sequencers: The history of sequencing DNA", *Genomics*, vol. 107, no. 1, pp. 1-8, 2016.

16. S. Agah, M. Zheng, M. Pasquali and A. Kolomeisky, "DNA sequencing by nanopores: advances and challenges", *Journal of Physics D: Applied Physics*, vol. 49, no. 41, p. 413001, 2016.

17. R. Zhang et al., "Distinguishing Individual DNA Bases in a Network by Non-Resonant Tip-Enhanced Raman Scattering", *Angewandte Chemie International Edition*, vol. 56, no. 20, pp. 5561-5564, 2017.

18. E. Bailo and V. Deckert, "Tip-Enhanced Raman Spectroscopy of Single RNA Strands: Towards a Novel Direct-Sequencing Method", *Angewandte Chemie International Edition*, vol. 47, no. 9, pp. 1658-1661, 2008.

19. S. Najjar et al., "Tip-Enhanced Raman Spectroscopy of Combed Double-Stranded DNA Bundles", *The Journal of Physical Chemistry C*, vol. 118, no. 2, pp. 1174-1181, 2014.

20. D. Zhang, K. Domke and B. Pettinger, "Tip-Enhanced Raman Spectroscopic Studies of the Hydrogen Bonding between Adenine and Thymine Adsorbed on Au (111)", *ChemPhysChem*, vol. 11, no. 8, pp. 1662-1665, 2010.

21. F. Pashaee, M. Tabatabaei, F. Caetano, S. Ferguson and F. Lagugné-Labarthet, "Tip-enhanced Raman spectroscopy: plasmid-free vs. plasmid-embedded DNA", *The Analyst*, vol. 141, no. 11, pp. 3251-3258, 2016.

22. J. Adamcik, D. Klinov, G. Witz, S. Sekatskii and G. Dietler, "Observation of single-stranded DNA on mica and highly oriented pyrolytic graphite by atomic force microscopy", *FEBS Letters*, vol. 580, no. 24, pp. 5671-5675, 2006.

23. W. Grange, M. Duckely, S. Husale, S. Jacob, A. Engel and M. Hegner, "VirE2: A Unique ssDNA-Compacting Molecular Machine", *PLoS Biology*, vol. 6, no. 2, p. e44, 2008.

24. W. Chen, W. Chen, Z. Chen, A. Gooding, K. Lin and C. Kiang, "Direct Observation of Multiple Pathways of Single-Stranded DNA Stretching", *Physical Review Letters*, vol. 105, no. 21, 2010.

25. A. Candelli, M. Modesti, E. Peterman and G. Wuite, "Single-molecule views on homologous recombination", *Quarterly Reviews of Biophysics*, vol. 46, no. 4, pp. 323-348, 2013.

26. T. Yano et al., "Tip-enhanced nano-Raman analytical imaging of locally induced strain distribution in carbon nanotubes", *Nature Communications*, vol. 4, no. 1, 2013.

27. M. Li, D. Dang, L. Liu, N. Xi and Y. Wang, "Imaging and Force Recognition of Single Molecular Behaviors Using Atomic Force Microscopy", *Sensors*, vol. 17, no. 12, p. 200, 2017.

28. F. Madzharova, Z. Heiner, M. Gühlke and J. Kneipp, "Surface-Enhanced Hyper-Raman Spectra of Adenine, Guanine, Cytosine, Thymine, and Uracil", *The Journal of Physical Chemistry C*, vol. 120, no. 28, pp. 15415-15423, 2016.

29. S. Yang and I. Butler, "Pressure-tuning infrared and Raman microscopy study of the DNA bases: adenine, guanine, cytosine, and thymine", *Journal of Biomolecular Structure and Dynamics*, vol. 31, no. 12, pp. 1490-1496, 2013.

30. Peticolas, W. L., Raman Spectroscopy of DNA and Proteins. In *Methods in Enzymology*; Biochemical Spectroscopy; Academic Press, Vol. 246, pp 389–416. 1995

31. J. De Gelder, K. De Gussem, P. Vandenabeele and L. Moens, "Reference database of Raman spectra of biological molecules", *Journal of Raman Spectroscopy*, vol. 38, no. 9, pp. 1133-1147, 2007.

32. P. Griffiths and L. Shao, "Self-Weighted Correlation Coefficients and Their Application to Measure Spectral Similarity", *Applied Spectroscopy*, vol. 63, no. 8, pp. 916-919, 2009.

33. J. Kawulok, "Approximate String Matching for Searching DNA Sequences", *International Journal of Bioscience, Biochemistry and Bioinformatics*, pp. 145-148, 2013.

# 4. QUANTUM PLASMONIC HOT ELECTRON INJECTION IN THE LATERAL $WSE_2$-$MOSE_2$ HETEROSTRUCTURE*

Lateral two-dimensional (2D) transitional metal dichalcogenide (TMD) heterostructures have recently attracted a wide attention as promising materials for optoelectronic nano-devices. Due to the nanoscale width of lateral heterojunctions, the study of their optical properties is challenging and requires using subwavelength optical characterization techniques. We investigated the photoresponse of a lateral 2D $WSe_2$-$MoSe_2$ heterostructure using tip-enhanced photoluminescence (TEPL) with nanoscale spatial resolution and with picoscale tip-sample distance dependence. We demonstrate the first observation of quantum plasmonic effects in 2D heterostructures and report the first nano-optical measurements of the lateral 2D TMD heterojunction width of ~ 150 nm and the quantum plasmonic tunneling distance of ~ 20 pm. The controllable plasmonic tip allows for both nano-optical imaging and plasmon-induced hot electron injection into the heterostructure, mediated by the depletion region. By adjusting the tip-sample distance, we demonstrated the controllability of the hot electron injection via the competition of two quantum plasmonic PL enhancement and quenching mechanisms. The directional charge transport in the depletion region leads to the increased hot electron injection in the $MoSe_2$ side of the junction, enhancing the $MoSe_2$ PL signal. The properties of the directional hot

* Reprinted/adapted with permission from Tang, C., He, Z., Chen, W., Jia, S., Lou, J., & Voronine, D. V., "Quantum plasmonic hot-electron injection in lateral WSe2/MoSe2 heterostructures." by *Physical Review B*, *98*(4), 041402, 2018, Copyright 2018 by American Physical Society

electron injection in the quantum plasmonic regime make the lateral 2D $MoSe_2$-$WSe_2$ heterostructures promising for quantum nano-devices with tunable photoresponse.

## 4.1. Introduction

### 4.1.1. Two-dimensional transition metal dichalcogenides (TMDs)

Two-dimensional (2D) transition metal dichalcogenides (TMDs) are promising candidates for optoelectronic devices [1]–[3], sensors [4]–[6], and photo-catalysts [7], [8]. Assembling two TMD materials vertically or laterally introduced new possibilities [9]–[12]. Optoelectronic properties of lateral heterostructures are determined by the band structure, doping, and defects of both materials near the boundary [13], [14]. Due to the nanoscale size and multi-component optical properties, lateral TMD heterostructures are suitable for single molecule sensing and nano-devices with tunable photoresponse [15], [16]. However, in order to fully understand and utilize the unique optoelectronic properties of these 2D materials it is important to characterize and control them with nanoscale spatial resolution.

### 4.1.2. Tip-enhanced photoluminescence (TEPL)

Tip-enhanced photoluminescence (TEPL) can be used to investigate the photoresponse of the subwavelength sharp boundary of TMD heterostructures. Resonant excitation of surface plasmons by the metallic tip generates large electric field enhancement [17], and therefore provides emission enhancement and the increase in spatial resolution [18]–[21]. However, when the distance between the tip and the substrate decreases to the sub-nanometer range, quantum tunneling effects become significant, leading to the saturation and quenching behavior of the near-field enhancement [22]–[28].

In addition to the enhanced electric field [29]–[31], the charge transfer mechanisms [32],[33] may also contribute to the improved sensitivity and spatial resolution. High spatial resolution of tip-enhanced imaging down to the sub-nm scale has recently been demonstrated [34]–[39]. Therefore, TEPL is well suited for studying the subwavelength heterostructures.

### 4.1.3. Tunneling hot electrons in 2D heterostructures

Tunneling hot electrons in 2D materials can be generated using a bias voltage [40], [41], photocurrent [42], and plasmonic nanostructures including plasmonic tips [43], [44]. Previous work showed that hot electron injection into the TMDs may facilitate photocatalytic reactions [7], [45] and photoelectron emission [46]. In addition to the electric field enhancement, the plasmon-induced hot electron injection may also contribute to the TMD photoluminescence enhancement via the carrier recombination mechanism. In this work, we show how these two mechanisms affect the photoresponse of pure TMDs and $MoSe_2$-$WSe_2$ heterostructure. Quantum plasmonic hot electron injection in the tip-TMD system may be described using the metal-semiconductor coupling model [47]–[50]. Plasmon-induced hot electrons can be transferred from the tip to the 2D semiconductor [51]. Plasmonic tips are especially suitable for hot electron transfer into semiconductors due to the high efficiency of hot carrier generation [52]. Moreover, directional hot electron transfer in TMD heterostructures may take place in the depletion region [47]–[49] and may be enhanced using quantum plasmonics. Quantum plasmonic effects were previously observed in plasmonic metallic nanostructures with sub-nanometer gaps, due to the quantum tunneling leading to the quenching of the local electric fields [26], [53], [54].

Since the quantum plasmonic effects are sensitive to the sub-nm gap size, it is possible to manipulate them by varying the gap size at the picometer scale in the quantum coupling limit. Recently, we developed a picometer-scale tip-sample distance dependence approach which is able to perform such precise measurements [28]. This approach is well suited for studying quantum plasmonic effects in 2D TMD heterostructures.

In this work, we observed the quantum plasmonic effects in the system of the coupled Au-coated plasmonic Ag tip and the MoSe2-WSe2 heterostructure on the Si/SiO2 substrate leading to the picoscale distance-dependent electric field quenching and charge transfer enhancement of the PL from the 2D heterojunction. Using the near-field TEPL imaging, we performed nanoscale optical characterization of the heterojunction and we achieved control of the junction PL by varying the nanoscale lateral tip position and picoscale tip-sample distance. For the tip-sample distance of $d > 0.36$ nm, the classical plasmon-induced hot electron injection is limited by the air gap barrier. For the gap size comparable to or smaller than the van der Waals contact distance, the electron tunneling facilitates thermionic injection in the quantum plasmonic regime [50]. This provides an alternative mechanism for manipulating the optoelectronic properties of 2D materials which may be used for improving the characterization and design of TMD based devices.

## 4.2. Materials and methods

### 4.2.1. lateral type II $MoSe_2$-$WSe_2$ heterostructure

The monolayer lateral type II $MoSe_2$-$WSe_2$ heterostructure was grown on the $Si/SiO_2$ substrate via chemical vapor deposition [55], [56]. $MoO_3$ and $WO_3$ acting as precursors were put into the center of the furnace. Se powder at upstream was introduced

into the furnace center by the hydrogen gas and it reacted with $MoO_3$ and $WO_3$ precursors to grow $MoSe_2$-$WSe_2$ heterojunctions at 750 ℃. Atomic force microscopy (AFM) revealed uniform thickness of the selected triangle area to be < 2 nm (Fig. 4.1b). We compared the photoluminescence (PL) intensity of the heterostructure with the Raman intensity of the $Si/SiO_2$ substrate to determine the number of layers. The near unity ratio and the narrow full width half maximum (FWHM) of the PL signal strongly indicate that the sample is a monolayer. The chemical composition of the $MoSe_2$ and $WSe_2$ parts of the heterostructure was also confirmed using the PL and Raman spectra shown in Figs.4.1c and 4.1d, respectively.

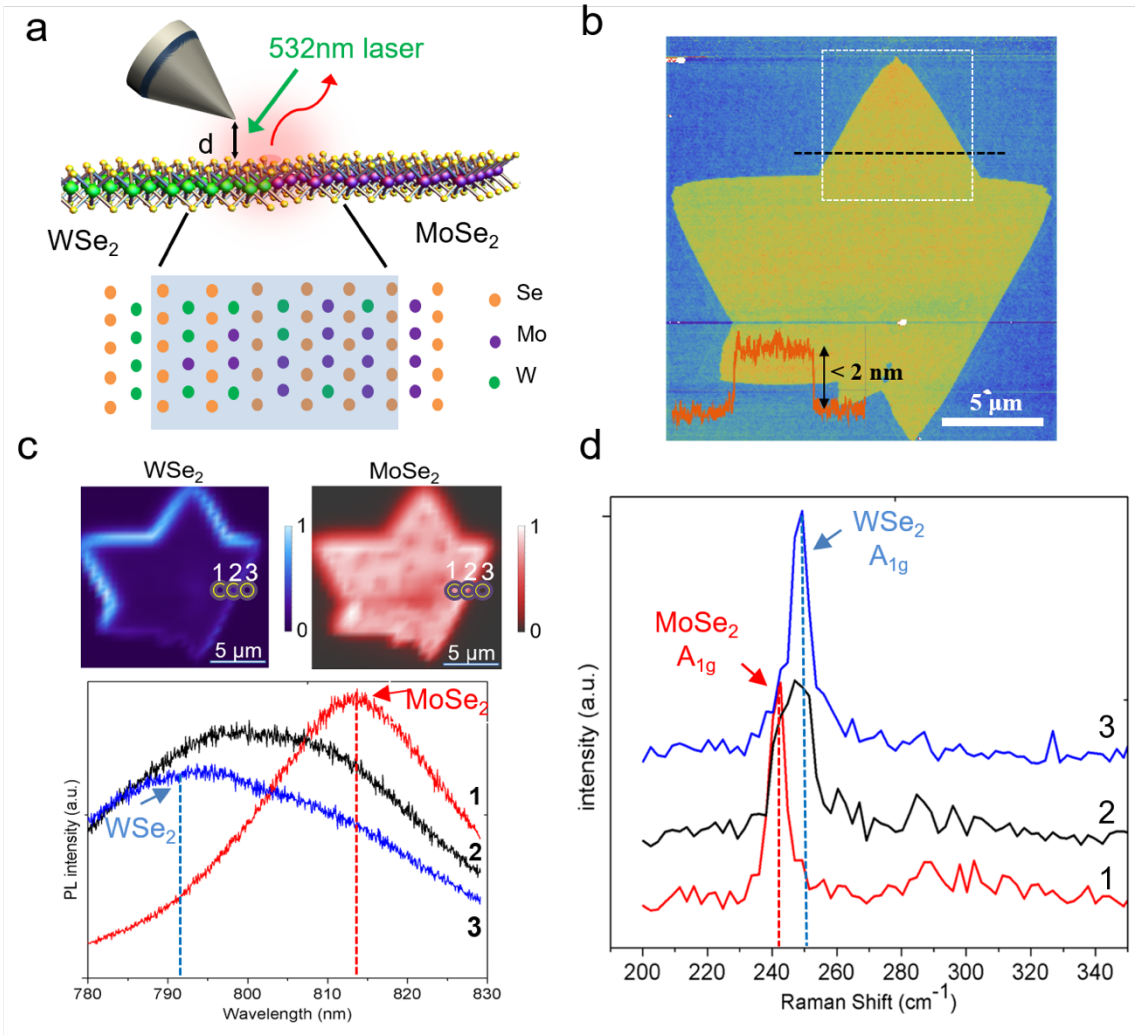


**Figure 4.1 Lateral 2D $MoSe_2$-$WSe_2$ heterostructure. (a) Sketch of the tip-enhanced photoluminescence (TEPL) measurement setup. 532 nm linearly polarized laser (green arrow) is focused onto a Au-coated plasmonic Ag nanotip operated in the contact mode with the controllable tip-sample distance d. The back-scattered TEPL signal (red arrow) is collected as a function of d in the classical (d > 0.36 nm) and quantum plasmonic (d < 0.36 nm) regimes. (b) Atomic force microscopy (AFM) image of the $MoSe_2$-$WSe_2$ heterostructure. The bottom profile curve shows a uniform sample thickness < 2 nm along the black dashed line. (c) Normalized far-field PL images of the $WSe_2$ (blue) and $MoSe_2$ (red) parts of the heterostructure. Highlighted spots 1, 2, and 3 correspond to the $MoSe_2$, junction and $WSe_2$ parts of the heterostructure, respectively. (d) The corresponding Raman spectra show the peaks of $WSe_2$ at 250 cm-1 [57], $MoSe_2$ at 242 cm-1 [58] and both peaks at the heterojunction.**

### 4.2.2. Experimental setup

TEPL was carried out using the state-of-the-art commercial system (OmegaScope-R, formerly AIST-NT, now Horiba Scientific, coupled with LabRAM Evolution microscope, Horiba Scientific). Silicon tips with apex radius ~ 10 nm were used for AFM and Au-coated Ag tips with apex radius ~ 10 - 25 nm were used for TEPL measurements. The 532 nm linearly polarized laser radiation was focused onto the tip apex at an incident angle of 53 degrees (Fig. 4.1a) and the resulting PL signals were collected using the same objective (100×, NA 0.7, f = 200). The sample was scanned while recording at each point both the near-field and the far-field PL in the contact mode with the controllable tip-sample distance d ~ 0.36 nm and ~ 20 nm, respectively. For the results shown in Figs. 4.2a and 4.2b, the laser power was 2.5 mW and the sample scanning step size was 40 nm, with 0.2 s acquisition time. The results shown in Figs. 4.2d and 4.2e were obtained with the same laser power and acquisition time while the scanning step size was 1 nm.

## 4.3. Results

### 4.3.1. TEPL imaging of $MoSe_2$-$WSe_2$ heterostructures

We performed TEPL imaging of the part of the $MoSe_2$-$WSe_2$ heterostructure marked by the dashed rectangular area in Fig. 4.1b. The double Gaussian fitting of the heterojunction PL is shown in Fig. 4.2c, where the $WSe_2$ (centered at 783 nm, 1.58 eV) and $MoSe_2$ (centered at 806 nm, 1.54 eV) components are shown by blue and red curves, respectively. The integrated values within FWHM of these Gaussian functions represent the total PL intensities of both components. Figs. 4.2a and 4.2b show the integrated PL intensity distributions of the $WSe_2$ and $MoSe_2$ for the near-field TEPL and far-field PL,

respectively. The near-field image in Fig. 4.2a shows a sharper heterojunction boundary than the far-field image in Fig. 4.2b. To estimate the junction width, we scanned the tip along the white dashed line across the junction with 1 nm step size (Figs. 4.2d and 4.2e), which showed ~150 nm and >400 nm width in the near-field and far-field profiles, respectively. Therefore, compared with the confocal PL microscopy, TEPL with subwavelength spatial resolution is more suitable for probing the spectral properties of the heterojunction.

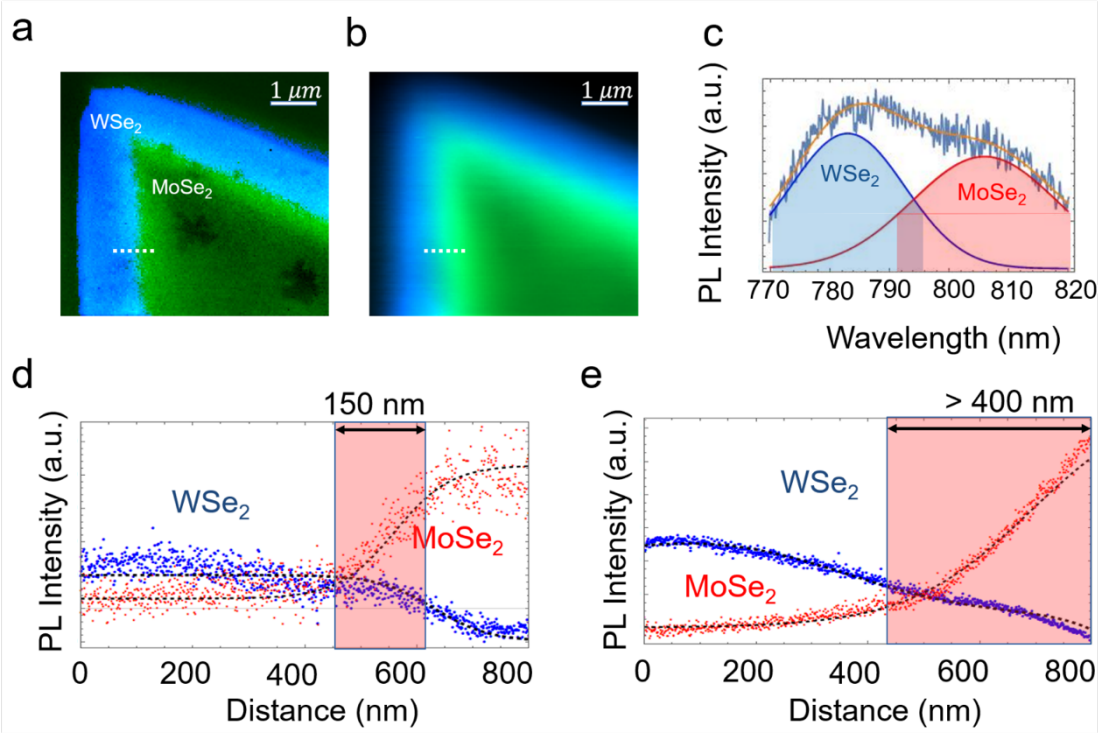


**Figure 4.2 Tip-enhanced photoluminescence (TEPL) imaging of the $MoSe_2$ - $WSe_2$ heterostructure. (a) Near-field PL image with the tip-sample distance d ~ 0.36 nm and (b) far-field PL image with d ~ 20 nm. The green and blue areas correspond to the integrated $MoSe_2$ (806 nm) and $WSe_2$ (783 nm) PL signals, respectively. The PL intensity of each component is obtained by integrating the area which corresponds to the FWHM of each component's Gaussian fit (c). Spatial dependence of the near-field (d) and far field (e) PL intensity of both components along a white dashed line crossing the heterojunction marked in (a) and (b), respectively. The heterojunction width is highlighted in (d) and (e) by the shaded red areas.**

### 4.3.2. Directional hot electron injection

To understand the effects of the tip-sample interaction on the PL of the heterostructure, we varied the tip-sample distance from ~ 40 nm to the Au-S van der Waals (vdW) contact of ~ 0.36 nm and further down to ~ 0.2 nm which was estimated according to the contact force via the Lenard-Jones potential [18], [28], [32], [34], [59]. The

picometer-scale tip-sample distance dependence calibration procedure was used as previously described [28]. Two main factors, namely, the local electric field enhancement and the hot electron injection, contribute to the tip-sample distance dependence of the PL signal. As the tip-sample distance decreases from 40 nm to 20 nm, the near-field effects gradually emerge while the hot electron injection can be neglected (Fig. 4.3 and SI Fig. 4.1). For the pure $WSe_2$, the near-field enhancement saturates at $d \approx 20$ nm, at which point, the hot electron injection rate increases, leading to a competition between the PL enhancement induced by hot electrons and quenching due to the attenuation of the tip electric field [60]. For the CVD-grown pure $WSe_2$, the concentration of the holes is larger than the intrinsic electrons, and, therefore, its PL shows gradual enhancement in the classical regime of $0.36 \text{ nm} < d < 40$ nm (Fig. B1a & B1c). Once the tip and $WSe_2$ are within the van der Waals contact separation ($d = 0.36$ nm), thermionic injection may occur with the increasing electron density in $WSe_2$ [50]. Consequently, an abrupt increase of the PL intensity in pure $WSe_2$ can be seen in Fig. B1a & B1c. On the other hand, for the CVD-grown $MoSe_2$, as the electron-hole recombination is limited by the lack of the intrinsic holes, the PL of pure $MoSe_2$ shows no significant enhancement (Fig. B1b & B1c).

Directional hot electron injection may take place at the heterojunction of $MoSe_2$ and $WSe_2$ due to the carrier-deficient depletion region formed at the junction [47]–[49]. Fig. 4.3b shows a schematic energy diagram of the hot electrons transferred to $MoSe_2$ due to the chemical potential gradient at the heterojunction [9], [10]. As the tip diameter is comparable to or narrower than the size of the $WSe_2$-$MoSe_2$ depletion region, the energy needed for the diffused hot electrons transferred to the $MoSe_2$ side to tunnel back to the

tip is higher because of the air barrier. The Au-semiconductor depletion region [47] also performs as a barrier to reduce the backward tunneling of the dissipated hot electrons in the $MoSe_2$. Therefore, as the tip-sample distance decreases from 20 nm to 0.36 nm, the injected hot electrons accumulate in $MoSe_2$, resulting in the PL enhancement in $MoSe_2$ while quenching the PL in $WSe_2$ at the heterojunction (Fig. 4.2c and 4.2d) [46], [61]. It is the depletion region that allows for the $MoSe_2$ side of the heterojunction accumulating more plasmon-induced hot electrons than in the pure materials. This directionality contributes to the unequal enhancement of the TEPL signals from the $MoSe_2$ and $WSe_2$ sides of the heterojunction.

**Figure 4.3 Directional plasmonic hot electron injection in the $WSe_2$-$MoSe_2$ heterostructure revealed by TEPL distance dependence. (a) TEPL tip-sample distance dependence from 40 nm to 0.2 nm, showing abrupt changes in the PL spectra of $WSe_2$ and $MoSe_2$ components when the tip-sample distance $d \leq 0.36$ nm, indicating the quantum-to-classical transition in the photo response of the heterostructure coupled to the plasmonic tip. (b) Energy diagram of the lateral $MoSe_2$-$WSe_2$ heterojunction shows the directional hot electron injection due to the potential gradient at the junction. Two control mechanisms are shown: hot electron injection (thick black arrows) and plasmon-induced charge transfer (green arrow), and TEPL (purple) leading to the controllable quenching or enhancement of the PL signals (dashed arrows). (c, d) Tip-sample distance dependence of the PL intensities of the $WSe_2$ and $MoSe_2$ components at the heterojunction. The dashed line at d = 0.36 nm corresponds to the van der Waals (vdW) contact distance between the tip and the sample and the transition from the classical to the quantum plasmonic regime. (e, f) Zoomed-in plots of the heterojunction PL tip-sample distance dependence in the quantum regime. Solid black lines in (c) – (f) are the fittings obtained using the theoretical model described below.**

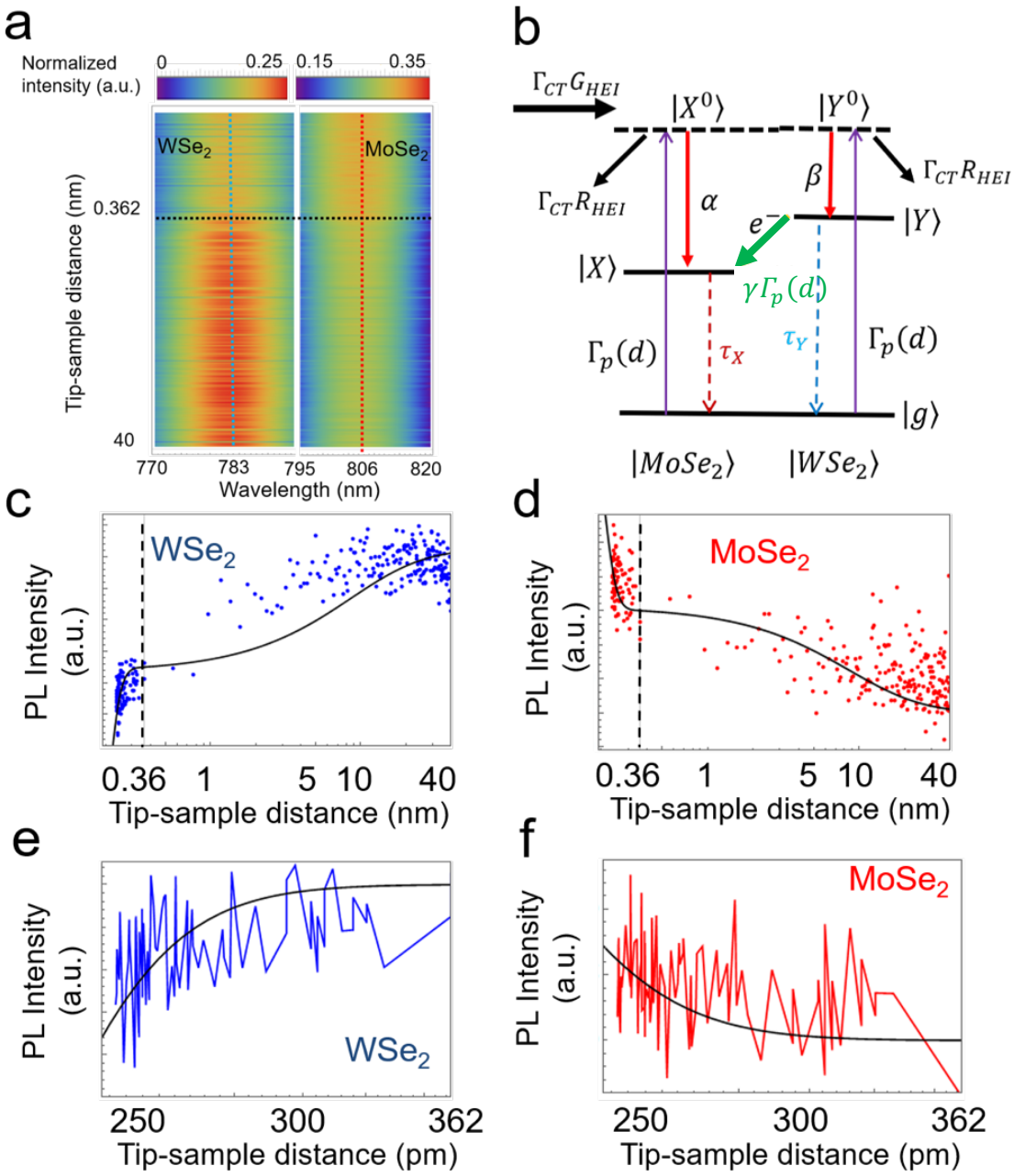
a
Normalized intensity (a.u.)
0
0.25
0.15
0.35
WSe2
MoSe2
Tip-sample distance (nm)
0.362
40
770
783
795
806
820
Wavelength (nm)
b
$\Gamma_{CT}G_{HEI}$
$|X^0\rangle$
$|Y^0\rangle$
$\Gamma_{CT}R_{HEI}$
$\Gamma_{CT}R_{HEI}$
$\alpha$
$\beta$
$e^-$
$|Y\rangle$
$|X\rangle$
$\gamma\Gamma_p(d)$
$\Gamma_p(d)$
$\tau_X$
$\tau_Y$
$\Gamma_p(d)$
$|g\rangle$
$|MoSe_2\rangle$
$|WSe_2\rangle$
c
WSe2
PL Intensity (a.u.)
0.36
1
5
10
40
Tip-sample distance (nm)
d
MoSe2
PL Intensity (a.u.)
0.36
1
5
10
40
Tip-sample distance (nm)
e
PL Intensity (a.u.)
WSe2
250
300
362
Tip-sample distance (pm)
f
MoSe2
PL Intensity (a.u.)
250
300
362
Tip-sample distance (pm)

### 4.4. Theoretical model of the hot electron injection

Next we present a theoretical model used to fit the data which accounts for the competition between the two quantum plasmonic effects, explaining the quantum plasmonic hot electron injection and near field PL quenching mechanisms. Fig. 4.3b shows the simplified diagram of the energy states and transitions at the $WSe_2$-$MoSe_2$ heterojunction, including the effects of the hot electron injection, photo-induced charge transfer, and tip-enhanced photoluminescence due to the tip-sample interaction. The simulation results are shown in Figs. 4c-4f (black curves). The initial state populations $N_{X0}$, $N_{Y0}$, and $N_g$ of the excited states $|X^0\rangle$, $|Y^0\rangle$, and the ground state $|g\rangle$, respectively, and the exciton populations $N_X$, and $N_Y$ of the $MoSe_2$ state $|X\rangle$ and the $WSe_2$ state $|Y\rangle$, respectively, can be described by the rate equations [62]:

$$\frac{dN_{X0}}{dt} = (G_{HEI} - R_{HEI}N_{X0})\Gamma_{CT}(d) - \alpha N_{X0} + \Gamma_p(d)\big(N_g - N_{X0}\big), \tag{4.1}$$

$$\frac{dN_X}{dt} = \alpha N_{X0} + \gamma\Gamma_p(d)N_Y - \frac{N_X}{\tau_X}, \tag{4.2}$$

$$\frac{dN_{Y0}}{dt} = -\beta N_{Y0} - RN_{Y0}\Gamma_{CT}(d) + \Gamma_p(d)\big(N_g - N_{Y0}\big), \tag{4.3}$$

$$\frac{dN_Y}{dt} = \beta N_{Y0} - \gamma\Gamma_p(d)N_Y - \frac{N_Y}{\tau_Y}, \tag{4.4}$$

$$\frac{dN_g}{dt} = -\Gamma_p(d)\big(N_g - N_{X0}\big) - \Gamma_p(d)\big(N_g - N_{Y0}\big) + \frac{N_X}{\tau_X} + \frac{N_Y}{\tau_Y}, \tag{4.5}$$

where $\Gamma_{CT}G_{HEI}$ is the hot electron injection (HEI) rate, and $\Gamma_{CT}R_{HEI}$ is the hot electron decay rate from states $|X^0\rangle$ or $|Y^0\rangle$ [62]. We assume $G_{HEI} = R_{HEI} = 1$. The quantum plasmonic tunneling $\Gamma_{CT}(d)$ is given by:

$$\Gamma_{CT}(d) = \begin{cases} Ae^{-\frac{d-c}{d_{CT}}}\ ps^{-1}, \text{for } d < 0.36\,nm, \\ 0 \qquad\qquad , \text{for } d > 0.36\,nm. \end{cases} \tag{4.6}$$

$\Gamma_{CT}(d)$ describes the efficiency of the hot electron tunneling between the tip and the sample, $d_{CT}$ is the average tunneling distance in the quantum plasmonic regime of $d < 0.36\,nm$. For simplicity, we neglected the tunneling for the tip-sample distance larger than the vdW contact distance of 0.36 nm. $A$ is the normalization parameter. The near-field pumping rate $\Gamma_p(d)$ describes the local optical excitation by the near field of the tip as [18]

$$\Gamma_p(d) = \begin{cases} 1 - e^{-\frac{d-c}{d_p}}, \text{ for } c < d < 0.36\,nm, \\ B(R + d - c)^{-4}, \text{ for } d > 0.36\,nm, \end{cases} \quad (4.7)$$

where $d_p$ is the average quantum coupling distance which leads to the quenching of the optical excitation by the charge tunneling from the tip in the quantum plasmonic regime when $d < 0.36\,nm$. R = 25 nm is the tip radius, B is a fitting parameter to smoothen the piecewise function, and c is the conductive contact distance which corresponds to the Ohmic tip-sample contact. When the tip-sample distance d < c, the near field of the tip is completely quenched and the pumping rate $\Gamma_p(d) = 0$. Since the TEPL depends on $\Gamma_p(d)$, we only consider in the region of d > c. The exciton generation rates of $MoSe_2$ and $WSe_2$ are given by $\alpha = 1\,ps^{-1}$ and $\beta = 1\,ps^{-1}$, respectively [63]. $\gamma\Gamma_p(d)$ is the photo-induced charge transfer rate across the junction [64], where we assume the constant $\gamma = 1$. The near-field excitation may facilitate the charge transfer within heterostructures [64]. The exciton relaxation times of $MoSe_2$ and $WSe_2$ were taken as $\tau_X = \tau_Y = 2\,ps$ [65].

The model was used to fit the tip-sample distance dependence results shown in Fig. 4.3. The main fitting parameters were $d_{CT} = d_p = 0.02\,nm$, and c = 0.17 nm. The latter

shows the measured conductive contact distance approximately equal to the half of the vdW contact distance (0.36 nm) between the Ag and S atoms. If we decrease the tip-sample distance d to ~ 0.17 nm, the near-field TEPL signal is expected to be completely quenched. The sun-nm values of the mean distance parameters $d_{CT}$ and $d_p$ reflect the tunneling nature of the quantum plasmonic effects. Our model fits the experimental results well in both the classical and quantum regimes as shown in Figs. 4.3c and 4.3d. In the classical regime (d > 0.36 nm), since the near-field pumping rate $\Gamma_{\mathrm{p}}(d)$ is larger when the distance d approaches 0.36 nm, the photo-induced charge transfer $\gamma\Gamma_{\mathrm{p}}(d)$ leads to the decrease of the $WSe_2$ PL signal and the increase of the $MoSe_2$ PL signal which corresponds to the decrease of the tip-sample distance d in the classical regime. On the other hand, in the quantum regime (d < 0.36 nm), the quantum plasmonic hot electron injection and PL quenching effects are dominant.

### 4.5. Conclusion

Once the tip-sample distance reaches the van der Waals contact (d = 0.36 nm), the sub-nanometer gap between the tip and the sample leads to the quantum plasmonic hot electron injection and quantum tip-sample coupling. Previous TEPL measurements in sub-nanometer gap metal-metal contacts showed that the PL is quenched due to the quantum tunneling [59]. Despite the absence of the metal-metal contacts here, the PL of pure $MoSe_2$ shows quenching when d < 0.36 nm (Fig. B1b). At the heterojunction, the PL intensity of the $WSe_2$ component also shows quenching (Figs. 4.3a, 4.3c, 4.3e and Fig. B2c). The repeated TEPL measurements on the heterostructure confirm the observed effects (Fig.

B2). On the other hand, the $MoSe_2$ component shows abrupt enhancement when $d < 0.36$ nm (Figs. 4.3a, 4.3d, 4.3f and Fig. B2d). These phenomena could be explained by the decrease of the air barrier between the tip and the sample, leading to the increased number of the quantum plasmonic hot electrons injected into $MoSe_2$ due to the quantum tunneling and the corresponding decrease of the number of surface charges and near-field intensity of the tip [53],[59]. The quantum plasmonic hot electron injection enhances the PL signal of the $MoSe_2$ part of the junction due to the increase of the recombination rate which is larger than the PL decrease due to the near-field quenching. On the other hand, the hot electron accumulation in the $WSe_2$ part of the junction is suppressed due to the charge transfer across the depletion region leading to the overall quenching of the $WSe_2$ PL. This delicate interplay of the two PL enhancement mechanisms may be controlled by the lateral tip position and tip-sample distance dependence. Due to the nanoscale size, the plasmonic tip can be used to generate hot electrons with high precision in the depletion region formed by the heterostructure which may be used for designing controllable nano-devices.

**4.6. References**

1. K. F. Mak and J. Shan, "Photonics and optoelectronics of 2D semiconductor transition metal dichalcogenides," *Nat. Photonics*, vol. 10, no. 4, pp. 216–226, 2016.

2. H. Tian *et al.*, "Optoelectronic devices based on two-dimensional transition metal dichalcogenides," *Nano Res.*, vol. 9, no. 6, pp. 1543–1560, 2016.

3. J. Ross *et al.*, "Electrically tunable excitonic light-emitting diodes based on monolayer WSe2 p-n junctions," *Nat. Nanotechnol.*, vol. 9, no. 4, pp. 268–272, 2014.

4. M. Pumera and A. H. Loo, “Layered transition-metal dichalcogenides (MoS2 and WS2) for sensing and biosensing,” *TrAC Trends Anal. Chem.*, vol. 61, pp. 49–53, 2014.

5. D. Sarkar *et al.*, “Functionalization of Transition Metal Dichalcogenides with Metallic Nanoparticles: Implications for Doping and Gas-Sensing,” *Nano Lett.*, vol. 15, no. 5, pp. 2852–2862, 2015.

6. M. Feierabend, G. Berghäuser, A. Knorr, and E. Malic, “Proposal for dark exciton based chemical sensors,” *Nat. Commun.*, vol. 8, p. ncomms14776, 2017.

7. Y. Shi *et al.*, “Hot Electron of Au Nanorods Activates the Electrocatalysis of Hydrogen Evolution on MoS2 Nanosheets,” *J. Am. Chem. Soc.*, vol. 137, no. 23, pp. 7365–7370, 2015.

8. Q. Lu, Y. Yu, Q. Ma, B. Chen, and H. Zhang, “2D Transition-Metal-Dichalcogenide-Nanosheet-Based Composites for Photocatalytic and Electrocatalytic Hydrogen Evolution Reactions,” *Adv. Mater.*, vol. 28, no. 10, pp. 1917–1933, 2016.

9. J. Kang, S. Tongay, J. Zhou, J. Li, and J. Wu, “Band offsets and heterostructures of two-dimensional semiconductors,” *Appl. Phys. Lett.*, vol. 102, no. 1, p. 012111, 2013.

10. C. Gong, H. Zhang, W. Wang, L. Colombo, R. M. Wallace, and K. Cho, “Band alignment of two-dimensional transition metal dichalcogenides: Application in tunnel field effect transistors,” *Appl. Phys. Lett.*, vol. 103, no. 5, p. 053513, 2013.

11. A. K. Geim and I. V. Grigorieva, “Van der Waals heterostructures,” *Nature*, vol. 499, no. 7459, pp. 419–425, 2013.

12. H. Lim, S. I. Yoon, G. Kim, A.-R. Jang, and H. S. Shin, “Stacking of Two-Dimensional Materials in Lateral and Vertical Directions,” *Chem. Mater.*, vol. 26, no. 17, pp. 4891–4903, 2014.

13. C. Huang *et al.*, “Lateral heterojunctions within monolayer MoSe2–WSe2 semiconductors,” *Nat. Mater.*, vol. 13, no. 12, pp. 1096–1101, 2014.

14. Y. Gong *et al.*, “Vertical and in-plane heterostructures from WS2/MoS2 monolayers,” *Nat. Mater.*, vol. 13, no. 12, pp. 1135–1142, 2014.

15. M.-Y. Li, C.-H. Chen, Y. Shi, and L.-J. Li, “Heterostructures based on two-dimensional layered materials and their potential applications,” *Mater. Today*, vol. 19, no. 6, pp. 322–335, 2016.

16. M.-Y. Li *et al.*, “Epitaxial growth of a monolayer WSe2-MoS2 lateral p-n junction with an atomically sharp interface,” *Science*, vol. 349, no. 6247, pp. 524–528, 2015.

17. P. Nordlander and E. Prodan, “Plasmon Hybridization in Nanoparticles near Metallic Surfaces,” *Nano Lett.*, vol. 4, no. 11, pp. 2209–2213, 2004.

18. K.-D. Park, O. Khatib, V. Kravtsov, G. Clark, X. Xu, and M. B. Raschke, “Hybrid Tip-Enhanced Nanospectroscopy and Nanoimaging of Monolayer WSe2 with Local Strain Control,” *Nano Lett.*, vol. 16, no. 4, pp. 2621–2627, 2016.

19. W. Su, N. Kumar, S. Mignuzzi, J. Crain, and D. Roy, “Nanoscale mapping of excitonic processes in single-layer MoS2 using tip-enhanced photoluminescence microscopy,” *Nanoscale*, vol. 8, no. 20, pp. 10564–10569, 2016.

20. Z. He *et al.*, “Tip-Enhanced Raman Scattering on Bulk MoS2 Substrate,” *IEEE J. Sel. Top. Quantum Electron.*, vol. 23, no. 2, pp. 113–118, 2017.

21. A. M. Alajlan, D. V. Voronine, A. M. Sinyukov, Z. Zhang, A. V. Sokolov, and M. O. Scully, “Gap-mode enhancement on MoS2 probed by functionalized tip-enhanced Raman spectroscopy,” *Appl. Phys. Lett.*, vol. 109, no. 13, p. 133106, 2016.

22. A. G. Borisov, J. Aizpurua, P. Nordlander, and R. Esteban, “Bridging quantum and classical plasmonics with a quantum-corrected model,” *Nat. Commun.*, vol. 3, p. 825, 2012.

23. J. Zuloaga, E. Prodan, and P. Nordlander, “Quantum Description of the Plasmon Resonances of a Nanoparticle Dimer,” *Nano Lett.*, vol. 9, no. 2, pp. 887–891, 2009.

24. K. B. Crozier and W. Zhu, “Quantum mechanical limit to plasmonic enhancement as observed by surface-enhanced Raman scattering,” *Nat. Commun.*, vol. 5, p. 5228, 2014.

25. N. J. Halas, S. Lal, W.-S. Chang, S. Link, and P. Nordlander, “Plasmons in Strongly Coupled Metallic Nanostructures,” *Chem. Rev.*, vol. 111, no. 6, pp. 3913–3961, 2011.

26. M. S. Tame, K. R. McEnery, Ş. K. Özdemir, J. Lee, S. A. Maier, and M. S. Kim, “Quantum plasmonics,” *Nat. Phys.*, vol. 9, no. 6, p. nphys2615, 2013.

27. J. A. Scholl, A. García-Etxarri, A. L. Koh, and J. A. Dionne, “Observation of Quantum Tunneling between Two Plasmonic Nanoparticles,” *Nano Lett.*, vol. 13, no. 2, pp. 564–569, 2013.

28. Y. Zhang *et al.*, “Improving resolution in quantum subnanometre-gap tip-enhanced Raman nanoimaging,” *Sci. Rep.*, vol. 6, p. srep25788, 2016.

29. N. Kumar, S. Mignuzzi, W. Su, and D. Roy, “Tip-enhanced Raman spectroscopy: principles and applications,” *EPJ Tech. Instrum.*, vol. 2, no. 1, p. 9, 2015.

30. P. Verma, “Tip-Enhanced Raman Spectroscopy: Technique and Recent Advances,” *Chem. Rev.*, vol. 117, no. 9, pp. 6447–6466, 2017.

31. D. Richards, R. G. Milner, F. Huang, and F. Festy, “Tip-enhanced Raman microscopy: practicalities and limitations,” *J. Raman Spectrosc.*, vol. 34, no. 9, pp. 663–667, 2003.

32. Z. Zhang, S. Sheng, R. Wang, and M. Sun, “Tip-Enhanced Raman Spectroscopy,” *Anal. Chem.*, vol. 88, no. 19, pp. 9328–9346, 2016.

33. N. Hayazawa, H. Watanabe, Y. Saito, and S. Kawata, “Towards atomic site-selective sensitivity in tip-enhanced Raman spectroscopy,” *J. Chem. Phys.*, vol. 125, no. 24, p. 244706, 2006.

34. J. Steidtner and B. Pettinger, “Tip-Enhanced Raman Spectroscopy and Microscopy on Single Dye Molecules with 15 nm Resolution,” *Phys. Rev. Lett.*, vol. 100, no. 23, p. 236101, 2008.

35. R. Zhang *et al.*, “Chemical mapping of a single molecule by plasmon-enhanced Raman scattering,” *Nature*, vol. 498, no. 7452, pp. 82–86, 2013.

36. C. Chen, N. Hayazawa, and S. Kawata, “A 1.7 nm resolution chemical analysis of carbon nanotubes by tip-enhanced Raman imaging in the ambient,” *Nat. Commun.*, vol. 5, p. ncomms4312, 2014.

37. F. Latorre *et al.*, “Spatial resolution of tip-enhanced Raman spectroscopy - DFT assessment of the chemical effect,” *Nanoscale*, vol. 8, no. 19, pp. 10229–10239, 2016.

38. S. Trautmann *et al.*, “A classical description of subnanometer resolution by atomic features in metallic structures,” *Nanoscale*, vol. 9, no. 1, pp. 391–401, 2016.

39. C. Zhang, B.-Q. Chen, and Z.-Y. Li, “Optical Origin of Subnanometer Resolution in Tip-Enhanced Raman Mapping,” *J. Phys. Chem. C*, vol. 119, no. 21, pp. 11858–11871, 2015.

40. B. Fischer, A. Ghetti, L. Selmi, R. Bet, and E. Sangiorgi, “Bias and temperature dependence of homogeneous hot-electron injection from silicon into silicon dioxide at low voltages,” *IEEE Trans. Electron Devices*, vol. 44, no. 2, pp. 288–296, 1997.

41. D. Lock, K. R. Rusimova, T. L. Pan, R. E. Palmer, and P. A. Sloan, “Atomically resolved real-space imaging of hot electron dynamics,” *Nat. Commun.*, vol. 6, p. ncomms9365, 2015.

42. W. Wang, A. Klots, D. Prasai, Y. Yang, K. I. Bolotin, and J. Valentine, “Hot Electron-Based Near-Infrared Photodetection Using Bilayer MoS2,” *Nano Lett.*, vol. 15, no. 11, pp. 7440–7444, 2015.

43. M. L. Brongersma, N. J. Halas, and P. Nordlander, “Plasmon-induced hot carrier science and technology,” *Nat. Nanotechnol.*, vol. 10, no. 1, pp. 25–34, 2015.

44. C. Clavero, “Plasmon-induced hot-electron generation at nanoparticle/metal-oxide interfaces for photovoltaic and photocatalytic devices,” *Nat. Photonics*, vol. 8, no. 2, pp. 95–103, 2014.

45. T. Hartman, C. S. Wondergem, N. Kumar, A. van den Berg, and B. M. Weckhuysen, “Surface- and Tip-Enhanced Raman Spectroscopy in Catalysis,” *J. Phys. Chem. Lett.*, vol. 7, no. 8, pp. 1570–1584, 2016.

46. T. P. White and K. R. Catchpole, “Plasmon-enhanced internal photoemission for photovoltaics: Theoretical efficiency limits,” *Appl. Phys. Lett.*, vol. 101, no. 7, p. 073905, 2012.

47. S. M. Sze and K. K. Ng, *Physics of Semiconductor Devices*. John Wiley & Sons, 2006.

48. K. Chen *et al.*, “Electronic Properties of MoS2–WS2 Heterostructures Synthesized with Two-Step Lateral Epitaxial Strategy,” *ACS Nano*, vol. 9, no. 10, pp. 9868–9876, 2015.

49. D. Cahen and A. Kahn, “Electron Energetics at Surfaces and Interfaces: Concepts and Experiments,” *Adv. Mater.*, vol. 15, no. 4, pp. 271–277, 2003.

50. A. Allain, J. Kang, K. Banerjee, and A. Kis, “Electrical contacts to two-dimensional semiconductors,” *Nat. Mater.*, vol. 14, no. 12, pp. 1195–1205, 2015.

51. J. S. DuChene, B. C. Sweeny, A. C. Johnston-Peck, D. Su, E. A. Stach, and W. D. Wei, “Prolonged Hot Electron Dynamics in Plasmonic-Metal/Semiconductor Heterostructures with Implications for Solar Photocatalysis,” *Angew. Chem. Int. Ed.*, vol. 53, no. 30, pp. 7887–7891, 2014.

52. P. J. Schuck, “Nanoimaging: Hot electrons go through the barrier,” *Nat. Nanotechnol.*, vol. 8, no. 11, pp. 799–800, 2013.

53. W. Zhu *et al.*, “Quantum mechanical effects in plasmonic structures with subnanometre gaps,” *Nat. Commun.*, vol. 7, p. ncomms11495, 2016.

54. J. A. Scholl, A. L. Koh, and J. A. Dionne, “Quantum plasmon resonances of individual metallic nanoparticles,” *Nature*, vol. 483, no. 7390, pp. 421–427, 2012.

55. A. Ramasubramaniam, D. Naveh, and E. Towe, “Tunable band gaps in bilayer transition-metal dichalcogenides,” *Phys. Rev. B*, vol. 84, p. 205325, 2011.

56. H. Sahin *et al.*, “Anomalous Raman spectra and thickness-dependent electronic properties of WSe2$,” *Phys. Rev. B*, vol. 87, no. 16, p. 165409, 2013.

57. W. Zhao *et al.*, “Lattice dynamics in mono- and few-layer sheets of WS2 and WSe2,” *Nanoscale*, vol. 5, no. 20, p. 9677, 2013.

58. G. W. Shim *et al.*, “Large-Area Single-Layer MoSe2 and Its van der Waals Heterostructures,” *ACS Nano*, vol. 8, no. 7, pp. 6655–6662, 2014.

59. V. Kravtsov, S. Berweger, J. M. Atkin, and M. B. Raschke, “Control of Plasmon Emission and Dynamics at the Transition from Classical to Quantum Coupling,” *Nano Lett.*, vol. 14, no. 9, pp. 5270–5275, 2014.

60. A. Hartschuh, “Tip-enhanced optical spectroscopy,” *Philos. Trans. R. Soc. Lond. Math. Phys. Eng. Sci.*, vol. 362, no. 1817, pp. 807–819, 2004.

61. T. Dixit, I. A. Palani, and V. Singh, “Role of Surface Plasmon Decay Mediated Hot Carriers toward the Photoluminescence Tuning of Metal-Coated ZnO Nanorods,” *J. Phys. Chem. C*, vol. 121, no. 6, pp. 3540–3548, 2017.

62. A. Vercik, Y. G. Gobato, I. Camps, G. E. Marques, M. J. S. P. Brasil, and S. S. Makler, “Kinetics of excitonic complexes on tunneling devices,” *Phys. Rev. B*, vol. 71, no. 7, p. 075310, 2005.

63. H. Chen *et al.*, “Ultrafast formation of interlayer hot excitons in atomically thin $MoS_2/WS_2$ heterostructures,” *Nat. Commun.*, vol. 7, p. 12512, 2016.

64. F. Ceballos, M. Z. Bellus, H.-Y. Chiu, and H. Zhao, “Ultrafast charge separation and indirect exciton formation in a MoS2-MoSe2 van der Waals heterostructure,” *ACS Nano*, vol. 8, no. 12, pp. 12717–12724, 2014.

65. C. Robert *et al.*, “Exciton radiative lifetime in transition metal dichalcogenide monolayers,” *Phys. Rev. B*, vol. 93, no. 20, p. 205423, 2016.

# 5. QUANTUM PLASMONIC CONTROL OF TRIONS IN A PICOCAVITY WITH MONOLAYER $WS_2$[*]

Monitoring and controlling the neutral and charged excitons (trions) in 2D materials are essential for the development of high-performance devices. However, nanoscale control is challenging due to diffraction-limited spatial resolution of conventional far-field techniques. Here, we extend the classical tip-enhanced photoluminescence (TEPL) based on tip-substrate nanocavity to quantum regime, and demonstrate controlled nano-optical imaging, namely, tip-enhanced quantum plasmonics (TEQPL). In addition to improving the spatial resolution, we use the scanning probe to control the optoelectronic response of monolayer $WS_2$ by varying the neutral/charged exciton ratio via charge tunneling in Au-Ag picocavity. We observe trion "hot spots" generated by varying the picometer-scale probe-sample distance, and show the effects of weak and strong coupling, which depend on the spatial location. Our experimental results are in agreement with simulations and open an unprecedented view of a new range of quantum plasmonics phenomena with 2D materials that will help designing new quantum optoelectronic devices.

---

[*] Reprinted/adapted with permission from "Quantum plasmonic control of trions in a picocavity with monolayer WS2." by He, Z., Han, Z., Yuan, J., Sinyukov, A. M., Eleuch, H., Niu, C., ... & Scully, M. O., 2019. *Science advances*, *5*(10), eaau8763. 

## 5.1. Introduction

### 5.1.1. Quasiparticles in TMDs

Two-dimensional transition metal dichalcogenides (TMDs) have attracted worldwide attention for their promising applications in photonics [1] , sensing [2] , and optoelectronic nanodevices [3]. Low-dimensional quantum confinement effects play a major role in the optoelectronic response of 2D TMDs such as monolayer tungsten disulfide ($WS_2$) [4]. Many-body states such as neutral excitons, trions, and biexcitons govern the photo-response in TMDs [5, 6]. Their interconversion may be controlled by using photoexcitation or bias, which strongly depends on the local inhomogeneities such as impurities, defects, or external dopants. As a result, unlike the bulk materials, the optoelectronic properties of monolayer $WS_2$ are dominated by excitons and trions [4]. Therefore, controlling the excitons in 2D TMDs allows manipulating the device performance.

Previous work on the control of neutral excitons ($X^0$) and negatively charged trions ($X^-$) was based on the exciton interconversion $X^0 + e^- \rightarrow X^-$ via gating [7], photo-excitation [8], plasmonic hot carriers [9], and chemical doping [14] . However, the nanoscale optical control of the 2D materials has not yet been realized. Nanoscale control of trions is of great importance in optoelectronic nano-devices, for example, CNT film-based electroluminescence devices [11] and $MoS_2$-based field-effect transistors [12]. Here we show that quantum plasmonics provides a convenient and effective tool for generation, nano-imaging, and control of trions in 2D materials.

### 5.1.2. Tip-enhanced Quantum plasmonics (TEQPL)

Quantum plasmonics plays an important role when the dimensions of plasmonic nanostructures reach a critical sub-nanometer size [13], as, for example, in the picoscale cavity formed by the plasmonic scanning probe and metal substrate [14]. Few-layer $MoS_2$ in the picocavity showed interesting tunneling-induced photoluminescence (PL) and Raman quenching effects [14]. However, although the classical plasmonic modulation of excitons in $MoS_2$ has been achieved [15, 16], the quantum yield of exciton generation is low in few-layer compared to monolayer 2D materials and the quantum plasmonic control of trions in monolayer TMDs was not yet explored. Using tip-enhanced quantum plasmonic (TEQPL) imaging, we show that it is possible to locally control both neutral excitons and trions in monolayer $WS_2$. Compared to the classical plasmonic imaging, TEQPL can be used to control and monitor the exciton interconversion by varying the size of the picocavity.

### 5.1.3. Quantum plasmonics for TEPL

The classical tip-enhanced photoluminescence (TEPL) technique provides a high spatial resolution beyond the optical diffraction limit due to the near-field enhancement of the PL signals by localized surface plasmon resonances (LSPR) of a plasmonic scanning probe such as a silver or gold coated nano tip [14, 17]. The classical tip-substrate coupling leads to the large local electric field enhancement within a tip-sample distance of $1 < d < 10$ nm with an additional enhancement in the case of a metallic substrate via gap-mode plasmons. However, for very small sub-nanometer gaps, the near-field enhancement may be reduced due to the quantum plasmonic effects such as tunneling of surface charges in

the gap plasmon TMD system [14]. As a result, the tunneling electrons reduce the overall surface charges and the corresponding local electromagnetic fields at the probe [18, 19]. Previously we reported similar control experiments in a plasmonic picocavity made of a pure gold substrate and gold tip (without $WS_2$) and observed quantum plasmonic quenching due to electron tunneling [14]. Here, we use quantum plasmonic effects in a Au-Ag substrate-tip picocavity to control trions in monolayer $WS_2$ by the tunneling charges. In addition, due to the picometer-scale control of the tip-sample distance, we obtained picoscale control of the photo-response in the vertical tip-sample coupling direction. Using TEQPL, we achieved both imaging and control of neutral excitons and trions with a high lateral spatial resolution of ~ 80 nm. This is the first demonstration of quantum plasmonic interconversion of neutral excitons to trions in 2D materials, which has promising applications of novel nanoscale light-matter interaction schemes in atomically thin semiconductors.

**5.2. Methods**

The schematic representation of the experimental setup is shown in Fig. 5.1a. We used the state-of-the-art commercial scanning probe microscopy system to perform the coupled atomic force microscopy (AFM) and nano-optical TEQPL experiments with precisely controlled tip-sample distance (OmegaScope-R coupled with LabRAM, Horiba Scientific; details are given in the Methods section). Au-coated Ag tip was mounted on an AFM cantilever, and the 532 nm laser was focused on the tip apex, leading to the enhancement of local electric fields in the tip-substrate cavity. To study the quantum plasmonic effects, we constructed a picometer-gap cavity between the Au substrate and

the Au-coated Ag tip by calibrating the tip-sample distance using the force-distance analysis which was previously described [14] and is shown in Fig. C1. Briefly, we used the short-distance approximation of the Lennard-Jones potential to estimate the tip-sample distance within the van der Waals (vdW) contact between the Au and S atoms (0.35 nm) [20]. We used the vdW radii of 0.166 nm (Au) and 0.180 nm (S) for the estimation of the 0.346 nm Au-S contact.

Figs. 5.1c and 5.1e show the PL spectra of monolayer $WS_2$ in the Au-Ag cavity fitted by two Gaussian functions [19] centered at the PL signals of $X^0$ (614 nm) and $X^-$ (625 nm). Similar observations of trionic emission on both nonmetallic [4, 10, 21, 22] and metallic [23–26] substrates reported red-shifted negative trion peaks at room temperature. Fig. C10 shows the corresponding PL signals of $WS_2$ on $Si/SiO_2$ substrate for comparison with the PL on Au substrate. The PL spectra on the $Si/SiO_2$ substrate are in agreement with previous reports [21, 27], and show similar line shapes with ~ 30 meV separation between the PL peaks of neutral excitons and trions, indicating similar values of the binding energies on both substrates. The relative blue shift of ~ 10 nm on the Au compared to $Si/SiO_2$ substrate may be due to the combination of surface plasmonic effects [10, 21, 28] , and the release of strain in CVD-grown $WS_2$ due to the transfer on Au [25, 26].

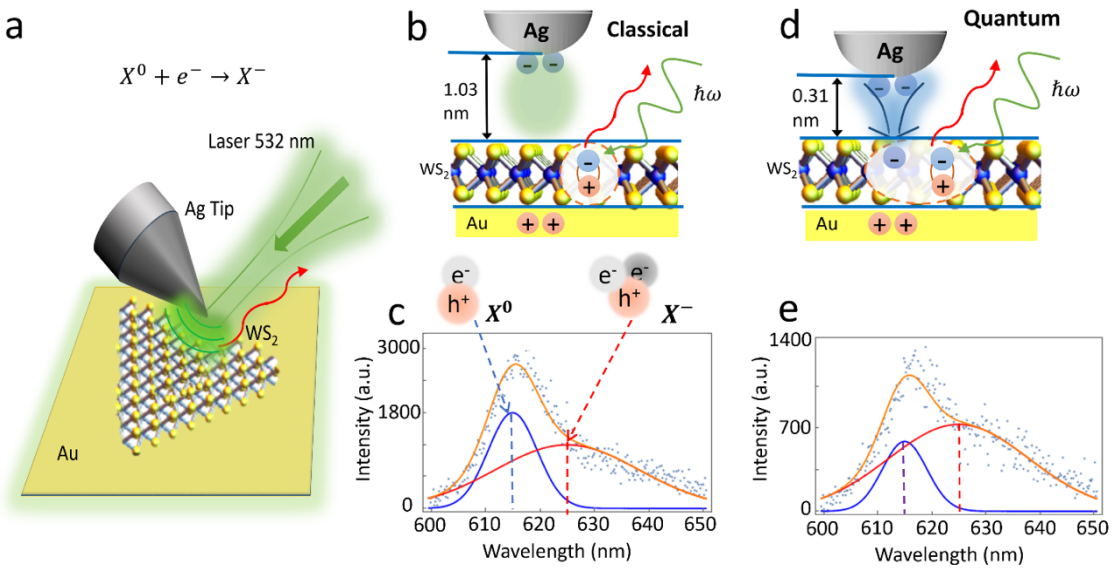


**Figure 5.1 Quantum plasmonic generation of trions in a Au-Ag picocavity with monolayer $WS_2$. (a) Schematic of tip-enhanced quantum plasmonic (TEQPL) imaging with monolayer $WS_2$ in a picocavity formed by the Ag tip and the Au substrate. The 532 nm laser beam was focused on the tip apex and the sample was scanned to obtain the photoluminescence (PL) spatial maps of neutral excitons ($X^0$) and trions ($X^-$). The tunneling-induced $X^0 \rightarrow X^-$ transition takes place for the short tip-sample distance. (b) Sketch of the Au-Ag cavity with d > 1 nm tip-sample distance which corresponds to the classical coupling (CC) regime. (c) PL spectra of $X^0$ and $X^-$ in monolayer $WS_2$ in the CC regime. Blue and red solid lines are Gaussian fitting functions centered at 614 nm and 625 nm, respectively. (d) and (e) are the corresponding sketch and PL spectra of monolayer $WS_2$ in the Au-Ag picocavity in the quantum coupling (QC) regime with the tip-sample distance $d$ < 0.35 nm where the charge tunneling (blue arrow in (d)) contributes to the formation of trions. The PL intensity of $X^-$ becomes larger than it is of $X^0$ in the QC (e) compared to the CC (c) regime.**

### 5.2.1. Binding energies of excitons and trions

Several previous theoretical studies predicted a strong dependence of the binding energy of both neutral excitons and trions on the dielectric properties of the substrate [29–31], that was confirmed experimentally for neutral excitons, however, contrary to the

predictions, only a weak dependence of binding energy on the substrate was shown experimentally for trions [32, 33]. Another recent model accounted for this difference by treating the monolayer TMD behavior of the transition metal and chalcogenide atomic sheets [34]. The trion wavefunctions, confined to the middle layer transition-metal sheet, were screened by the outer chalcogen layers. In addition, the model included the polaron effects of lattice distortion due to the charged exciton, which increased the effective mass of the trion and increased the trion's binding energy. This weak dependence allowed for the observation and control of trions on metallic substrates at room temperature.

## 5.3. Results

### 5.3.1. Classical and quantum regime of TEPL

Figs. 5.1c and 5.1e correspond to the two representative tip-sample distances $d$ for the classical coupling (CC) and quantum coupling (QC) regimes with $d > d_0$ and $d < d_0$, shown in Figs. 5.1b and 5.1d, respectively, where $d_0$ = 0.35 nm is the vdW contact distance. When $d$ = 0.31 nm (QC, Fig. 5.1e), the peak ratio of the $X^-$ and $X^0$ signals is larger than that of $d$ = 1.03 nm (CC, Fig. 5.1c), which indicates that the relative ratio of trions to neutral excitons increased due to the tunneling.

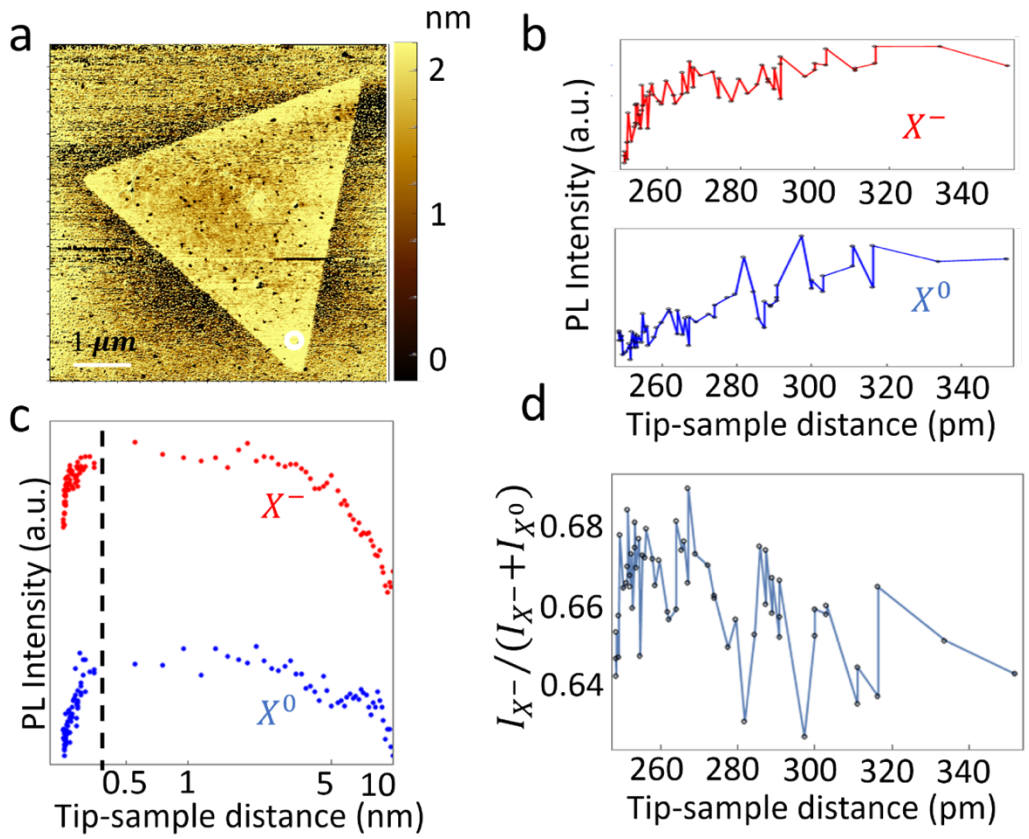


**Figure 5.2 Picoscale quantum plasmonic control of neutral excitons ($X^0$) and trions ($X^-$) in monolayer $WS_2$ in a Au-Ag cavity. (a) AFM image of the triangular monolayer WS2 nanoflake. Photoluminescence (PL) intensity of neutral excitons ($X^0$, blue) and trions ($X^-$, red) measured in a spatial location marked by a circle in (a) as a function of the tip-sample distance in the picometer scale (b) and in the whole range (c) shows the PL quenching of both signals at the picoscale distances. However, the ratio $I_{X^-}/(I_{X^0}+I_{X^-})$ shows an increase of the trion relative to the neutral exciton signal at distances shorter than 300 pm.**

Quantum plasmonic control of trions in monolayer $WS_2$ in the Au-Ag cavity was further investigated as a function of the tip-sample distance as shown in Fig. 5.2. AFM imaging confirmed the monolayer uniform thickness and a high quality of the triangular shaped $WS_2$ nanoflake (Fig. 5.2a). The PL intensity measured in the spatial location

marked by a circle in Fig. 5.2a was investigated as a function of the tip-sample distance in the range from 10 nm down to a few hundred pm which correspond to the CC and QC regimes, respectively (Fig. 5.2c). Fig. 5.2b shows the PL quenching of both neutral excitons ($X^0$, blue) and trions ($X^-$, red) at the picoscale distances. The rates of the $X^0$ and $X^-$ quenching are different due to the different mechanisms such as the tunneling-induced decrease of the local electric field at the tip apex [14, 35, 36] and the tunneling-assisted exciton-trion interconversion [12, 35]. The PL ratio $I_{X^-}/(I_{X^0} + I_{X^-})$ shows an increase of the trion signal at distances shorter than ~ 300 pm (Fig. 5.2d). More examples are shown in Fig. C2.

### 5.3.2. TEPL/TEQPL imaging

We then performed similar measurements on a complex WS2 nanoflake which consists of several areas of interest including a monolayer periphery and a few-layer center as well as a multi-layer structural defect at the right corner shown by the AFM height variations in Fig. 5.3a. TEQPL imaging provides a sensitive method for probing the heterogeneity of the nano-optical response of 2D materials. We obtained PL images of neutral excitons and trions by plotting the integrated areas under the corresponding fitted PL spectra (Figs. 5.3c-5.3f). We observed significant differences between the near-field (Figs. 5.3c and 5.3e) and far-field (Figs. 5.3d and 5.3f) PL images of the complex WS2 nanoflake in a Au-Ag cavity with the tip-sample distance of 0.31 nm and 10 nm, respectively. Compared with the far-field images, the near-field TEQPL images show a higher spatial resolution and reveal a rich variety of features. For example, the width of the Au-WS2 interface at the edge of the flake was measured as ~ 82 nm and 881 nm using

the near-field (NF) and far-field (FF) $X^-$ PL signals, respectively (Fig. 5.3g). The AFM profile in Fig. 5.3g indicates the position of the WS2-Au substrate boundary, which correlates well with the optically detected boundary in the NF images. The origin of the increased roughness of the AFM height profile in Fig. 5.3g is the use of the same Au-coated Ag tip for the AFM measurements and the simultaneous TEPL. The metal coating of the tip leads to the enhanced tip-sample interaction, which is responsible for the increased noise level with the estimated standard deviation of the height profile to be less than 1 nm.

Since TEQPL is based on tunneling, it is very sensitive to the thickness of the sample placed in the gap-mode-enhanced electric field of the cavity. This leads to a higher imaging contrast of TEQPL compared to the conventional FF PL. For example, the few-layer central triangle part of the WS2 nanoflake is better resolved in the NF TEQPL images (Figs. 5.3c and 5.3e) than in the FF PL images (Figs. 5.3d and 5.3f). Also, the top (G) and right (I) corners of the WS2 nanoflake have low intensities in both the FF and NF signals due to the presence of the charge doping effects in G and multi-layer structural defects in I. The increase in the height in I is supported by the correlated AFM data in Fig. 5.3a. The charge doping is supported by the correlated Kelvin probe force microscopy (KPFM) image which shows the surface contact potential difference (CPD) signal in Fig. 5.3b. KPFM shows larger signals in the G and I corners compared to H, which anti-correlate with the PL signal intensities. It has been previously shown that charge doping reduces the PL signals in 2D materials, which is in agreement with our results.

### 5.3.3. Kelvin probe force microscopy

The apparent lack of the clear triangular shapes in the FF and NF images is a result of the limited spatial resolution of ~ 880 nm and 80 nm for the FF and NF respectively, which limits the ability to resolve small triangular features (especially for the FF) in the chosen relatively small (~ 4 μm size nanoflake). The flake outlines in the NF images in Figs. 5.3c and 5.3e exhibit the triangular shape more clearly than the corresponding FF images in Figs. 5.3d and 5.3f. Still, the absence of the full triangular outline is due to two effects, namely, charge doping and multi-layer structural defect. In addition to the intrinsic charge doping of the nanoflake, there is also a quantum plasmonic contribution due to the plasmon-induced electron tunneling from the tip to the sample. Therefore, we performed KPFM measurement both without and with the simultaneous laser excitation (Fig. C4a and C4b, respectively). Now it is more clearly seen that quantum plasmonic charge doping leads to the significant variation of the contact potential difference across the G-H line of the KPFM image in the Fig. C4b.

### 5.3.4. TEPL near-field and far-field mapping of $X^0$ and $X^-$

More detailed information about the sample heterogeneity and the correlation of the AFM topography, KPFM surface potential and PL signals is shown in the line profiles in Figs. 5.3g and 5.3h obtained from the spatial maps as indicated by the white dashed lines (i) and (ii), respectively. The weaker PL signal from the central area is due to the indirect band gap nature of multilayer $WS_2$. Both FF PL and NF TEQPL signals are strong when the sample thickness is small as shown in the line profiles in Fig. 5.3h. The NF TEQPL signals show a significantly higher spatial resolution and qualitatively new spatial

features compared to the FF PL signals. Different areas of strong PL signals ("hot spots") exist at different locations in the NF images. For example, the left corner (H) shows strong FF PL hot spots of both neutral excitons (Fig. 5.3d) and trions (Fig. 5.3f). However, these hot spots are suppressed in the corresponding NF images (Figs. 5.3c and 5.3e). Also, the FF profiles of neutral excitons and trions are similar (Fig. 5.3h, green and orange lines), but the corresponding NF profiles show maximum intensity peak shifts of $X^0$ and $X^-$ (blue and red lines with shifted maxima highlighted by the vertical dashed lines), which indicates a possible quantum plasmonic tip-induced conversion $X^0 \rightarrow X^-$ in certain spatial locations. This qualitative difference between the hot spots in the FF and NF signals indicates the importance of the tip-sample interaction during the imaging, and it can be used for both imaging and controlling the excitons in 2D materials simultaneously by adjusting the appropriate instrument parameters. The PL spectra at different tip-sample distances and the corresponding $I_{X^-}/(I_{X^0} + I_{X^-})$ ratios for different spots labeled A – E in Figs. 5.3a and 5.3b are shown in Fig. C2. These selected spots provide a rich picture of various heterogeneous photo-responses. The results were reproducible as shown by the two consecutive distance dependence measurements at spot B in Fig. C6. Further insight about the sample heterogeneity may be obtained by a more detailed analysis of the NF TEQPL maps. For example, Fig. C7 and C8 show zoomed-in $X^0$ and $X^-$ maps with anti-correlated subwavelength features. The regions of large intensity in the $X^-$ map in Fig. C7b reveal trion "hot spots" (dashed circles). Similar regions in the $X^0$ map show the suppression of the PL signal in Fig. C7a. This provides evidence for the $X^0 \rightarrow X^-$ conversion due to the tunneling-induced tip-sample interaction. While FF PL maps

show microscale variation of contrast, they do not show any localized anti-correlations. (Fig. C7c and C7d).

**Figure 5.3 Tip-enhanced quantum plasmonic (TEQPL) imaging of a complex $WS_2$ nanoflake. (a) Atomic force microscopy (AFM) image shows the height topography with $WS_2$ triangular monolayer periphery and a few-layer triangular central region. Several areas of interest are marked (A) – (F) in different parts of the flake. (b) Kelvin probe force microscopy (KPFM) image under 532 nm laser illumination shows inhomogeneous contact potential difference (CPD) signal at the surface of the sample. (G), (H) and (I) mark the top, left and right corners, respectively. Near-field neutral exciton, $X^0$, (c) and trion, $X^-$, (e) TEQPL, and far-field $X^0$ (d) and $X^-$ (f) photoluminescence (PL) images of the complex $WS_2$ nanoflake in a Au-Ag cavity with the tip-sample distance of 0.31 nm and 10 nm, respectively. Black dashed lines indicate the outlines of the $WS_2$ nanoflake. The imaging step size is 50 nm. (g) and (h) Line profiles of the AFM, KPFM, and PL signals from the marked white dashed lines (i) and (ii), respectively. Vertical orange and red dashed lines in (g) mark the width of the far-field (FF) and near-field (NF) PL profiles, respectively, of trions at the Au- $WS_2$ interface at the edge of the flake. Vertical blue and red dashed lines in (h) mark the positions of the maximum signal intensities of the NF PL signal profiles of neutral excitons and trions, respectively, showing the relative shift of the two signals.**

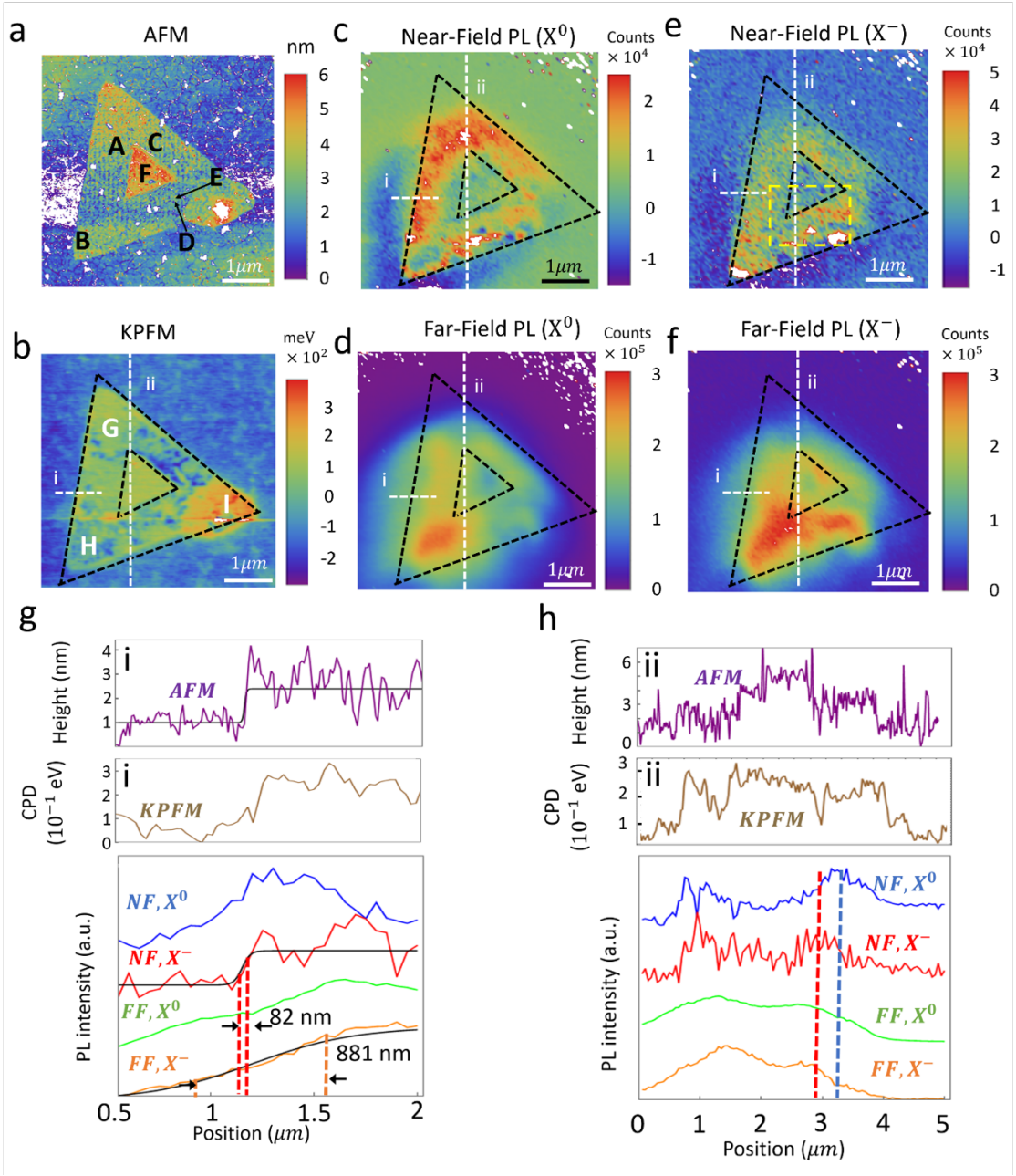
a
AFM
nm
A
C
F
E
B
D
1μm
c
Near-Field PL ($X^0$)
Counts × $10^4$
e
Near-Field PL ($X^-$)
Counts × $10^4$
b
KPFM
meV × $10^2$
G
H
I
d
Far-Field PL ($X^0$)
Counts × $10^5$
f
Far-Field PL ($X^-$)
Counts × $10^5$
g
Height (nm)
AFM
CPD ($10^{-1}$ eV)
KPFM
PL intensity (a.u.)
NF, $X^0$
NF, $X^-$
FF, $X^0$
FF, $X^-$
82 nm
881 nm
Position (μm)
h
Height (nm)
AFM
CPD ($10^{-1}$ eV)
KPFM
PL intensity (a.u.)
NF, $X^0$
NF, $X^-$
FF, $X^0$
FF, $X^-$
Position (μm)

### 5.3.5. Tip-sample distance dependence

The tip-sample distance used for the TEQPL images in Figs. 5.3c and 5.3e corresponds to the QC regime, where the local electric field was partially quenched by the tunneling leading to a significant contribution of the $X^0 \rightarrow X^-$ transition. The TEQPL images revealed a highly inhomogeneous pattern with localized regions of strong PL signals (hot spots) in accordance with previous reports of nano-optical imaging of 2D materials [17, 37] Here, we further investigated the tip-sample distance dependence from different spatial locations within the complex $WS_2$ nanoflake. Fig. 5.4 shows the tip-sample distance dependence of the $X^0$ and $X^-$ PL signal intensities from two spatial locations marked in Fig. 5.3a as spots A (Figs. 5.4b and 5.4c) and C (Figs. 5.4d and 5.4e). These two locations represent the typical examples of strong and weak quantum tip-sample coupling which correspond to the complete and incomplete quenching of the PL signals in the QC regime. Due to the small size of the tip apex, its influence on the FF PL signals within the 10 nm range can be ignored. Therefore, the effects of the varying tip-sample distance on the FF signals can be ignored and one expects the same FF contributions to the PL signals at all tip-sample distances plotted in Fig. 5.4.

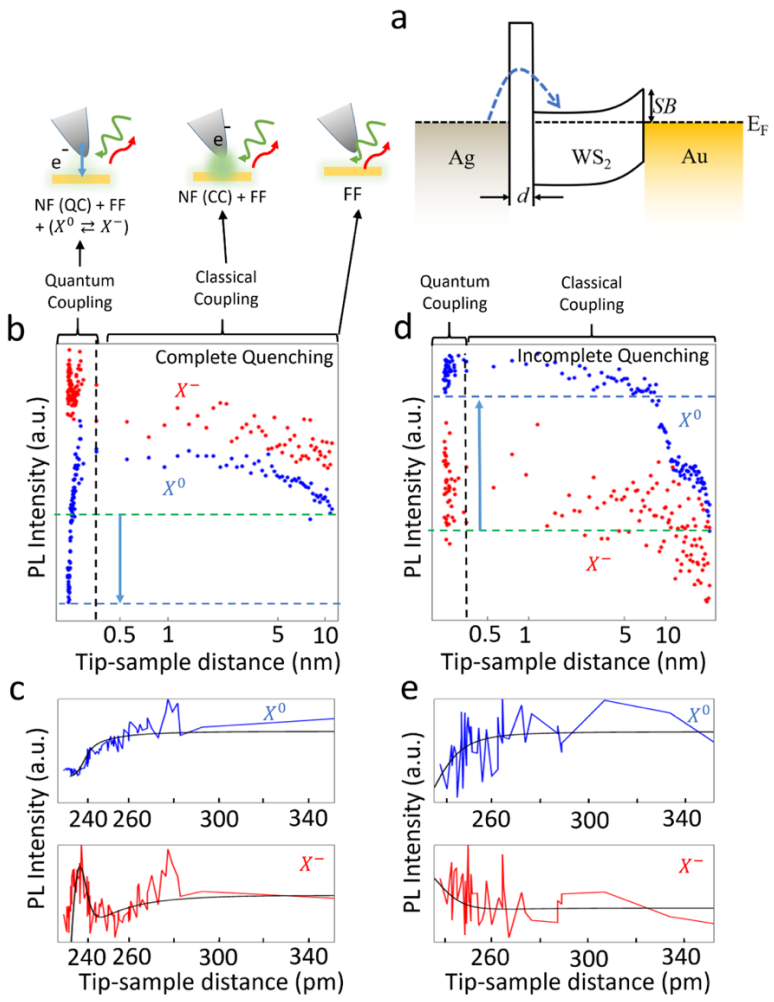


**Figure 5.4 Tip-sample distance dependence of photoluminescence (PL) of $WS_2$ nanoflake in a Au-Ag cavity. (a) Energy diagram of the tip-sample-substrate (Ag-$WS_2$-Au) system with Schottky barrier (SB). Tip-sample distance dependence of the PL signal intensities of neutral excitons ($X^0$) and trions ($X^-$) from two spatial locations marked A (b, c) and C (d, e) in Fig. 5.3a. Three regimes of tip-sample coupling are identified in (b): (i) far-field (FF) with no tip-sample coupling ($d$ > 10 nm), (ii) near-field with classical tip-sample coupling (NF CC) with 0.35 nm < $d$ < 10 nm, and (iii) near-field with quantum tip-sample coupling (NF QC) with $d$ < 0.35 nm. Green and blue dashed lines indicate the FF and the short-distance NF $X^0$ PL signals, respectively. Zoomed-in picoscale tip-sample distance dependence of TEQPL signals from spatial locations A (c) and C (e) in the QC regime. The vertical black dashed lines separate the CC and QC regimes at the van der Waals tip-sample contact distance (0.35 nm).**

### 5.3.6. Three regimes of TEPL

We consider three different regimes of tip-sample coupling which are indicated by arrows and corresponding schematic diagrams in Fig. 5.4b: (i) far-field (FF) with no tip-sample coupling (with tip-sample distance $d > 10$ nm and pure far-field excitation), (ii) near-field with classical tip-sample coupling (NF CC) with tip-sample distance 0.35 nm < $d < 10$ nm, and (iii) near-field with quantum tip-sample coupling (NF QC) with $d < 0.35$ nm. The case (ii) corresponds to the classical NF coupling while the case (iii) corresponds to the NF coupling with strong quantum plasmonics effects due to field quenching via tunneling and $X^0 \rightarrow X^-$transition. Fig. 5.4b shows the enhancement and quenching of the $X^0$ and $X^-$ PL signals in the NF CC and QC regimes, respectively. Interestingly, the $X^0$ PL intensity at the short tip-sample distances of < 250 pm is smaller than the $X^0$ FF PL intensity at the long distance of 10 nm, as indicated by the horizontal blue and green dashed lines in Fig. 5.4b, respectively. In the absence of the $X^0 \rightarrow X^-$transition, one would expect the same PL intensities in the case of the complete NF PL quenching at short tip-sample distance as in the case of the long-distance FF PL signal. This is because the tunneling completely suppresses the NF enhancement in the QC regime [14]. In the case of the incomplete PL quenching, the PL intensities at the short tip-sample distances are larger than at the long distances. This is indeed observed in the incomplete quenching case where the NF QC PL (blue dashed line) is larger than the FF PL (green dashed line) in Fig. 5.4d. However, this is not the case in the complete quenching case where the opposite behavior is observed (Fig. 5.4b). This may be attributed to the $X^0 \rightarrow X^-$ contribution which reduced the number of $X^0$ below the FF limit. This shows the main difference

between the classical TEPL imaging technique where the tip-sample interaction only leads to the confinement of the enhanced electric field. Due to the inhomogeneity of the $WS_2$ nanoflake under the ambient conditions in air, the Schottky barrier (SB) depends on the local surface energy [38] leading to the inhomogeneous local quenching behavior. The incomplete quenching may take place when the electron tunneling is suppressed by the $WS_2$-gold SB, while in the complete quenching case, the SB is low. In addition, the variations in the local electrostatic environment under the ambient conditions, revealed by the inhomogeneous CPD images in KPFM (Figs. 5.3b and Fig. C4) result in different tip-$WS_2$ tunneling efficiencies, which together with SB, determine the PL quenching. The spatial locations in Figs. 5.2 and 5.4b showed complete PL quenching, while the spatial locations in Figs. 5.4d and Fig. C3 showed incomplete PL quenching. Only the spots with complete PL quenching showed significant decrease of the $X^-$ signals in the QC range from 360 pm to 260 pm because of the strong contributions of the quantum plasmonic quenching effects needed to support the $X^0 \rightarrow X^-$ conversion.

### 5.3.7. Controlling the $X^0 \rightarrow X^-$ transition

Here we show that the tip-sample distance is a convenient control parameter. For example, Figs. 5.4c and 5.4d show zoomed-in picoscale tip-sample distance dependence of TEQPL signals from spatial locations A and C in Fig. 5.3a. Fig. 5.4c shows a decrease of the $X^-$ PL signal with the decrease of the tip-sample distance until it reaches ~ 250 pm. Classically, the opposite trend is expected in which the PL signal increases with the decrease of the gap due to the plasmonic gap-mode enhancement. Therefore, the observed PL quenching is attributed to the tunneling-induced quenching of the plasmonic fields.

Similar effects were previously predicted and observed in metallic plasmonic systems [13, 14, 39]. However, after the further decrease of the tip-sample distance below 250 pm the $X^-$ PL signal increases again with the simultaneous decrease of the $X^0$ PL signal. This gives a strong evidence for the tunneling-induced contribution of the $X^0 \rightarrow X^-$transition. Then, subsequently, the $X^-$ PL signal decreases again with the further decrease of the tip-sample distance below 240 pm which is attributed to the formation of the conductive channel in the reduced tip-substrate cavity gap. As a result, all the optical NF signals are suppressed.

The tip-sample distance dependence plots in Fig. 5.4 show the overall quenching of the PL signals of neutral excitons in both CC and QC regimes. However, the signals of trions show less changes in the QC regime for the selected spatial locations. The quenching rates for the neutral excitons and trions are different due to the contribution of the $X^0 \rightarrow X^-$transition. To show more clearly the competition of these two mechanisms we use the peak ratio $I_{X^-}/(I_{X^0} + I_{X^-})$ from the two adjacent spots E and D separated by 60 nm (Figs. 5.5b and 5.5d). In the CC regime, these peak ratios are constant and do not depend on the tip-sample distance (see Fig. C2). However, in the QC regime, spot E shows a decreasing ratio at $d < 260$ pm (Fig. 5.5b) and spot D shows the opposite behavior with an increasing ratio (Fig. 5.5d). This can be understood by analyzing the behavior of the $X^0$and $X^-$ PL signals separately for these two spots. Fig. 5.5c shows that the $X^-$ PL intensity in spot D did not significantly change, but the $X^0$ PL intensity decreased due to the $X^0 \rightarrow X^-$transition and tunneling, respectively. This indicates a significant contribution of the $X^0 \rightarrow X^-$ transition in spot D but also a reversal of the peak ratio and a significant

contribution of the opposite reaction in spot E leading to the inverse $X^- \rightarrow X^0$ transition. This shows a strong dependence of the observed effects on the spatial location and sample heterogeneity, and also provides new opportunities for controlling the subwavelength local photo-response of excitons in 2D materials.

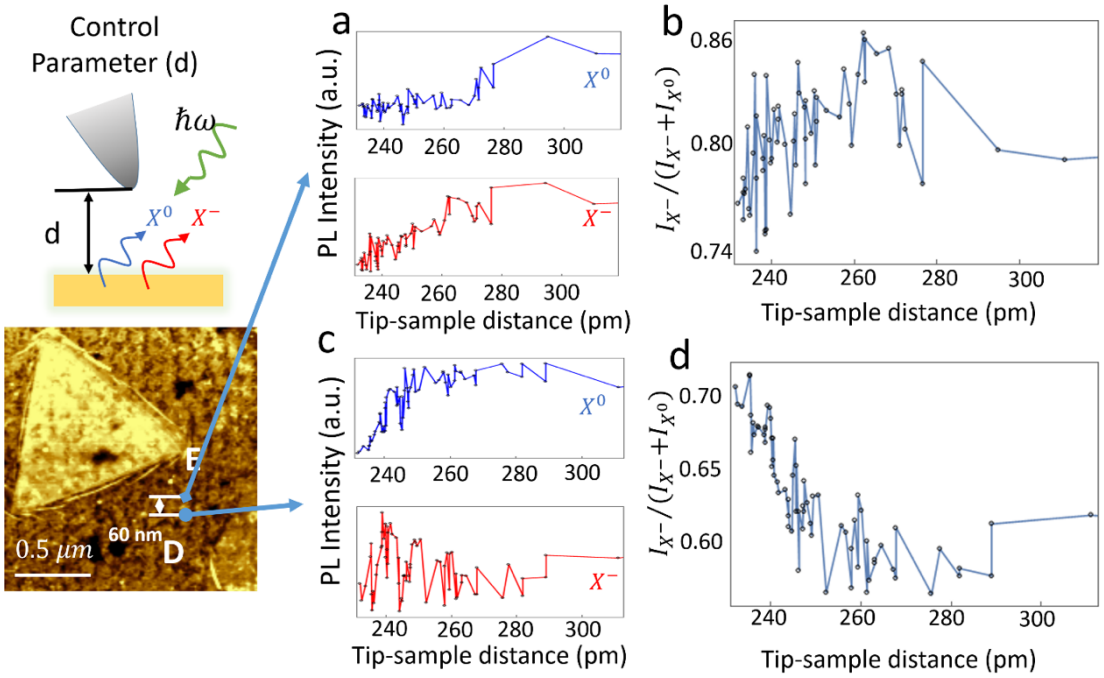


**Figure 5.5 Subwavelength control of trions in a Au-Ag picocavity with monolayer $WS_2$. Zoomed-in picoscale tip-sample distance dependence of TEQPL signals of neutral excitons $X^0$ (blue) and trions $X^-$ (red) from spatial locations E (a) and D (c) in the QC regime. The corresponding peak ratios $I_{X^-}/(I_{X^0} + I_{X^-})$ show the relative number of trions and neutral excitons and reveal the underlying quantum plasmonic mechanisms. Inset shows the tip-sample distance control parameter d and the AFM image of the central part of the complex $WS_2$ nanoflake with the marked locations of spots D and E separated by 60 nm. The peak ratios show two different types of behavior from the closely spaced locations which may be switched by varying the tip-sample distance by only a few picometers.**

## 5.4. Discussion

The TEQPL images revealed detailed inhomogeneous properties of the samples that correlated with the topography and CPD measurements. TEQPL also revealed specific locations with different quenching behavior that could not be identified using the conventional FF PL, AFM and KPFM techniques. Different regimes of PL imaging may be used for different purposes. Distance dependence may be classified based on the results shown in Fig. 5.4 into 4 cases. First, the classical PL enhancement increases with the decrease of the tip-sample distance. Second, the saturation of the enhancement takes place due to the energy transfer between the tip and the sample and the competing PL suppression., Third, PL control in the QC regime is achieved below the vdW distance due to the $X^0 \rightarrow X^-$ transition. Forth, the complete suppression of the TEQPL is due to the broken tip-substrate cavity and the formation of the classical conductive channels shown in Fig. 5.4c when d < 240 pm. Though the transition to quantum plasmonic trion generation increases the trion density in WS2, the strong near-field quenching mechanism suppresses the overall near-field effects. Therefore, the tip-sample distance should be optimized based on a specific target.

We distinguish two regimes of the tip-sample coupling, namely, the CC and QC regimes, which correspond to the tip-sample distance of d > 1 nm and d < 0.35 nm, respectively. In theory, we distinguish the classical TEPL and quantum TEQPL imaging techniques. However, in reality, both TEPL and TEQPL contribute in the quantum plasmonic regime of small tip-sample distance, where the classical near-field effects of TEPL are still present and, in addition, the quantum plasmonic effects make a significant

contribution. The contribution of the TEQPL can be controlled by varying the tip-sample distance. Optical NF and FF images in Fig. C3 show a small contribution of TEQPL and a significant contribution of TEPL, that was achieved by varying the setpoint of the AFM measurement. The NF maps of neutral excitons and trions in Fig. C3a and C3b, respectively, show correlated intensity distributions of the TEPL signals (the TEQPL signals show anti-correlated intensity distributions but contribute less in this measurement due to a different AFM setpoint). The comparison between the mostly TEQPL and mostly TEPL signals in Figs. 5.3 and Fig. C3, respectively, shows the key differences between the classical and quantum plasmonic techniques. The classical TEPL technique provides nanoscale imaging by the plasmonic near field enhancement but does not allow for the local control of the charged excitons and trions. The quantum plasmonic TEQPL technique provides new control tools in addition to imaging. This opens new possibilities of simultaneous imaging and control in the quantum regime.

## 5.5. Materials and methods

### 5.5.1. Atomic force microscopy (AFM)

We performed atomic force microscopy (AFM), Kelvin probe force microscopy (KPFM) and tip-enhanced quantum plasmonic (TEQPL) imaging of monolayer $WS_2$ in a Au-Ag tip-substrate cavity using the state-of-the-art commercial instrument (OmegaScope-R coupled to LabRAM, Horiba Scientific). Plasmonic Ag tips have larger near field enhancement compared to the Au tips. However, Ag rapidly oxidizes in air reducing the tip lifetime. Therefore, the Ag tips were coated with 3 – 4 nm of Au to protect

from oxidation. The $WS_2$ samples were grown on $Si/SiO_2$ substrates via chemical vapor deposition (CVD) and were transferred to the atomically flat Au substrates (Platypus).

### 5.5.2. AFM and TEPL scanning

AFM measurements were performed using a silicon tip with ~ 20 nm diameter. The scanning step size was 25 nm. Each scan took 3 mins with a scanning rate of 1.0 Hz. TEPL imaging was based on the contact mode AFM. 532 nm laser (400 μW power with the equivalent power density of $4\times10^5$ W/cm$^2$) was used for excitation and was adjusted to focus on the tip apex by optimizing the microscope objective. Both the FF and NF PL signals were collected before and after the tip-sample contact. The TEQPL scanning step size was 50 nm, and the acquisition time per pixel was 0.5 s. The NF signals were obtained by subtracting the data with and without the tip contact. The overall background was removed, and the PL spectra were normalized for convenience.

The contact mode AFM image, which was obtained during the TEQPL mapping simultaneously with the NF and FF PL maps in Fig. 5.3, shows the absence of any significant thermal drift (Fig. C5).

### 5.5.3. Tip-sample distance controlling

The PL distance dependence was performed by keeping the tip stationary within the laser focus lifting the sample up towards the tip using the piezo-electric control. The total displacement of the sample stage was 40 nm, but the actual tip-sample distance variation was less as it was previously described [14] and is shown in Fig. C1. The distance-dependence data was collected using 200 steps and the 0.5 s acquisition time per step.

### 5.5.4. Kelvin probe force microscopy

KPFM was performed using the same Au-coated Ag tip as was used in TEQPL for measuring the relative surface contact potential difference (CPD) between the sample and the tip. KPFM scans were performed with 25 nm step size under the 532 nm laser illumination.

All experiments were performed under the ambient conditions at room temperature.

### 5.5.5. Theoretical model

To understand the mechanisms of the two quantum plasmonic effects, that is the tunneling-induced $X^0 \rightarrow X^-$ transition and PL quenching, we developed a rate equation model describing the distance dependence of the PL of neutral excitons $X^0$ and trions $X^-$ by considering the ground $|g\rangle$, neutral exciton $|X^0\rangle$, and trion $|X^-\rangle$ states (Fig. C5a) with $N_g$, $N_{X^0}$, and $N_{X^-}$ populations, respectively:

$$\frac{dN_g}{dt} = -s\Gamma_p(d)\left(N_g - N_{X^-}\right) - \Gamma_p(d)\left(N_g - N_{X^0}\right) + \Gamma_{X^0}N_{X^0} + \Gamma_{X^-}N_{X^-} \quad (5.1)$$

$$\frac{dN_{X^0}}{dt} = \Gamma_p(d)\left(N_g - N_{X^0}\right) - \Gamma_{CT}(d)(N_{X^0}) + \beta\,\Gamma_{CT}(d)(N_{X^-}) - \Gamma_{X^0}N_{X^0} \quad (5.2)$$

$$\frac{dN_{X^-}}{dt} = s\Gamma_p(d)\left(N_g - N_{X^-}\right) + \Gamma_{CT}(d)(N_{X^0}) - \beta\,\Gamma_{CT}(d)(N_{X^-}) - \Gamma_{X^-}N_{X^-} \quad (5.3)$$

where $\tau_{X0} = 1/\Gamma_{X^0}$ and $\tau_{X^-} = 1/\Gamma_{X^-}$ are the neutral exciton and trion relaxation times, respectively. The relaxation times of the neutral excitons and trions in $WS_2$ at room temperature were approximately set to $\tau_{X0} = \tau_{X^-} = 1\ ps$ [40]. We only consider the near-field excitation in describing the distance dependence because the far-field excitation does not depend on the tip-sample distance that was kept below 10 nm. The near-field neutral

exciton pumping rate $\Gamma_p(d)$ depends on the tip-sample distance due to the tunneling-induced plasmonic field quenching. The corresponding near-field trion pumping rate $s\Gamma_p(d)$ includes the parameter $s$ to describe the ratio of the neutral exciton to trion excitation rate that was set to $s = 0.15$. Since we assume that the quantum quenching effects contribute at $d < 0.35$ nm, $\Gamma_p(d)$ is described by a piecewise function corresponding to the classical (CC) and quantum (QC) coupling regimes, [12]

$$\Gamma_p(d) = \begin{cases} 1 - e^{-\frac{d-c}{d_p}}, & \text{for } d < 0.35; \\ B(R + d - c)^{-4}, & \text{for } d > 0.35. \end{cases} \quad (5.4)$$

In the QC regime of $d < 0.35$ nm, the parameter $c$ represents the distance of the conductive contact between the tip and the sample with the complete quenching of the near field. The value $1/d_p = 0.02\ nm^{-1}$ describes the inverse mean tunneling distance. When $d > 0.35$ nm, the pumping rate is described by the near-field tip-sample energy transfer function $(R + d - c)^{-4}$, where R = 25 nm is the tip apex radius and $B$ is the smoothing parameter (*29*). The distance dependence of the tunneling-induced $X^0 \rightarrow X^-$ transition rate is given by $\Gamma_{CT}(d)$,

$$\Gamma_{CT}(d) = \begin{cases} Ae^{-\frac{d-c}{d_{CT}}}, & \text{for } d < 0.35; \\ 0, & \text{for } d > 0.35, \end{cases} \quad (5.5)$$

where we assume $\Gamma_{CT}(d) = 0$ in the CC regime for $d > 0.35$ nm due to the low tunneling probability for large tip-sample distance. The value $1/d_{CT}$ describes the inverse mean distance dependence of the $X^0 \rightarrow X^-$ transition rate. The ratio of $d_{CT}$ and $d_p$ shows the competition of the increase in trion PL due to the $X^0 \rightarrow X^-$ transition and the decrease in trion PL due to plasmonic quenching. A is a normalization parameter. The inverse $X^- \rightarrow$

$X^0$ transition probability was set to $\beta = 0.001$. This model was used to fit the results shown in Fig. 5.4. For the complete quenching case, $d_{CT} = 0.1d_p$, and $c = 0.234\,nm$. For the incomplete quenching case, $d_{CT} = 0.3d_p$, and $c = 0.220\,nm$. Our results show that the main differences between the complete and incomplete quenching are the larger parameters $1/d_{CT}$ and $c$ in the case of the complete quenching which shows the rapid increase of the $X^0 \rightarrow X^-$ transition rate with the decrease of the tip-sample distance *d*. Incomplete quenching shows the slow increase of the $X^0 \rightarrow X^-$ transition rate with *d* that cannot reach a significant value before the quantum quenching suppresses the near-field PL.

**5.6. References**


1. K. Mak and J. Shan, "Photonics and optoelectronics of 2D semiconductor transition metal dichalcogenides", *Nature Photonics*, vol. 10, no. 4, pp. 216-226, 2016.

2. R. Lv et al., "Transition Metal Dichalcogenides and Beyond: Synthesis, Properties, and Applications of Single- and Few-Layer Nanosheets", *Accounts of Chemical Research*, vol. 48, no. 1, pp. 56-64, 2014.

3. S. Butler et al., "Progress, Challenges, and Opportunities in Two-Dimensional Materials Beyond Graphene", *ACS Nano*, vol. 7, no. 4, pp. 2898-2926, 2013.

4. A. Boulesbaa et al., "Observation of two distinct negative trions in tungsten disulfide monolayers", *Physical Review B*, vol. 92, no. 11, 2015.

5. Y. You, X. Zhang, T. Berkelbach, M. Hybertsen, D. Reichman and T. Heinz, "Observation of biexcitons in monolayer WSe2", *Nature Physics*, vol. 11, no. 6, pp. 477-481, 2015.

6. A. Singh et al., "Trion formation dynamics in monolayer transition metal dichalcogenides", *Physical Review B*, vol. 93, no. 4, 2016.

7. M. Yoshida, A. Popert and Y. Kato, "Gate-voltage induced trions in suspended carbon nanotubes", *Physical Review B*, vol. 93, no. 4, 2016.

8. A. Mitioglu et al., "Optical manipulation of the exciton charge state in single-layer tungsten disulfide", *Physical Review B*, vol. 88, no. 24, 2013.

9. J. Li et al., "Tuning the photo-response in monolayer MoS2 by plasmonic nano-antenna", *Scientific Reports*, vol. 6, no. 1, 2016.

10. N. Peimyoo, W. Yang, J. Shang, X. Shen, Y. Wang and T. Yu, "Chemically Driven Tunable Light Emission of Charged and Neutral Excitons in Monolayer WS2", *ACS Nano*, vol. 8, no. 11, pp. 11320-11329, 2014.

11. S. Liang, Z. Ma, N. Wei, H. Liu, S. Wang and L. Peng, "Solid state carbon nanotube device for controllable trion electroluminescence emission", *Nanoscale*, vol. 8, no. 12, pp. 6761-6769, 2016.

12. K. Mak et al., "Tightly bound trions in monolayer MoS2", *Nature Materials*, vol. 12, no. 3, pp. 207-211, 2012.

13. M. Tame, K. McEnery, Ş. Özdemir, J. Lee, S. Maier and M. Kim, "Quantum plasmonics", *Nature Physics*, vol. 9, no. 6, pp. 329-340, 2013.

14. Y. Zhang et al., "Improving resolution in quantum subnanometre-gap tip-enhanced Raman nanoimaging", *Scientific Reports*, vol. 6, no. 1, 2016.

15. X. Yang et al., "Plasmon-exciton coupling of monolayer MoS 2 -Ag nanoparticles hybrids for surface catalytic reaction", *Materials Today Energy*, vol. 5, pp. 72-78, 2017.

16. S. Najmaei, A. Mlayah, A. Arbouet, C. Girard, J. Léotin and J. Lou, "Plasmonic Pumping of Excitonic Photoluminescence in Hybrid MoS2–Au Nanostructures", *ACS Nano*, vol. 8, no. 12, pp. 12682-12689, 2014.

17. W. Su, N. Kumar, S. Mignuzzi, J. Crain and D. Roy, "Nanoscale mapping of excitonic processes in single-layer MoS2 using tip-enhanced photoluminescence microscopy", *Nanoscale*, vol. 8, no. 20, pp. 10564-10569, 2016.

18. W. Zhu et al., "Quantum mechanical effects in plasmonic structures with subnanometre gaps", *Nature Communications*, vol. 7, no. 1, 2016.

19. Y. Wang et al., "Strain-induced direct–indirect bandgap transition and phonon modulation in monolayer WS2", *Nano Research*, vol. 8, no. 8, pp. 2562-2572, 2015.

20. A. Bondi, "van der Waals Volumes and Radii", *The Journal of Physical Chemistry*, vol. 68, no. 3, pp. 441-451, 1964.

21. S. Yun et al., "Synthesis of Centimeter-Scale Monolayer Tungsten Disulfide Film on Gold Foils", *ACS Nano*, vol. 9, no. 5, pp. 5510-5519, 2015.

22. K. Wei, Y. Liu, H. Yang, X. Cheng and T. Jiang, "Large range modification of exciton species in monolayer WS_2", *Applied Optics*, vol. 55, no. 23, p. 6251, 2016.

23. T. Kato and T. Kaneko, "Transport Dynamics of Neutral Excitons and Trions in Monolayer WS2", *ACS Nano*, vol. 10, no. 10, pp. 9687-9694, 2016.

24. S. Matthews, C. Zhao, H. Zeng and F. Bright, "Effects of Acetone Vapor on the Exciton Band Photoluminescence Emission from Single- and Few-Layer WS2 on Template-Stripped Gold", *Sensors*, vol. 19, no. 8, p. 1913, 2019.

25. Y. Zeng, W. Chen, B. Tang, J. Liao, J. Lou and Q. Chen, "Synergetic photoluminescence enhancement of monolayer MoS2via surface plasmon resonance and defect repair", *RSC Advances*, vol. 8, no. 42, pp. 23591-23598, 2018.

26. Y. Zeng, X. Li, W. Chen, J. Liao, J. Lou and Q. Chen, "Highly Enhanced Photoluminescence of Monolayer MoS2 with Self-Assembled Au Nanoparticle Arrays", *Advanced Materials Interfaces*, vol. 4, no. 21, p. 1700739, 2017.

27. Z. Wu, N. Zhu, J. Jiang, A. Zafar, J. Hong and Y. Zhang, "Tuning interlayer coupling by laser irradiation and broadband photodetection in vertical MoTe2/WS2 vdW heterostructure", *APL Materials*, vol. 7, no. 4, p. 041108, 2019.

28. Y. Kwon, K. Kim, W. Kim, S. Ryu and H. Cheong, "Variation of photoluminescence spectral line shape of monolayer WS 2", *Current Applied Physics*, vol. 18, no. 8, pp. 941-945, 2018.

29. M. Drüppel, T. Deilmann, P. Krüger and M. Rohlfing, "Diversity of trion states and substrate effects in the optical properties of an MoS2 monolayer", *Nature Communications*, vol. 8, no. 1, 2017.

30. T. Berkelbach, M. Hybertsen and D. Reichman, "Theory of neutral and charged excitons in monolayer transition metal dichalcogenides", *Physical Review B*, vol. 88, no. 4, 2013.

31. A. Chernikov et al., "Exciton Binding Energy and Nonhydrogenic Rydberg Series in MonolayerWS2", *Physical Review Letters*, vol. 113, no. 7, 2014.

32. E. Courtade et al., "Charged excitons in monolayer WSe2: Experiment and theory", *Physical Review B*, vol. 96, no. 8, 2017.

33. S. Borghardt et al., "Engineering of optical and electronic band gaps in transition metal dichalcogenide monolayers through external dielectric screening", *Physical Review Materials*, vol. 1, no. 5, 2017.

34. D. Van Tuan, M. Yang and H. Dery, "Coulomb interaction in monolayer transition-metal dichalcogenides", *Physical Review B*, vol. 98, no. 12, 2018.

35. K. Park, O. Khatib, V. Kravtsov, G. Clark, X. Xu and M. Raschke, "Hybrid Tip-Enhanced Nanospectroscopy and Nanoimaging of Monolayer WSe2 with Local Strain Control", *Nano Letters*, vol. 16, no. 4, pp. 2621-2627, 2016.

36. X. Wang, D. Zhang, K. Braun, H. Egelhaaf, C. Brabec and A. Meixner, "High-Resolution Spectroscopic Mapping of the Chemical Contrast from Nanometer Domains in P3HT:PCBM Organic Blend Films for Solar-Cell Applications", *Advanced Functional Materials*, vol. 20, no. 3, pp. 492-499, 2010.

37. D. Voronine, G. Lu, D. Zhu and A. Krayev, "Tip-Enhanced Raman Scattering of MoS2", *IEEE Journal of Selected Topics in Quantum Electronics*, vol. 23, no. 1, pp. 138-143, 2017.

38. "The physics and chemistry of the Schottky barrier height", *Applied Physics Reviews*, vol. 1, no. 1, p. 011304, 2014.

39. J. Zuloaga, E. Prodan and P. Nordlander, "Quantum Description of the Plasmon Resonances of a Nanoparticle Dimer", *Nano Letters*, vol. 9, no. 2, pp. 887-891, 2009.

40. Y. Yu et al., "Equally Efficient Interlayer Exciton Relaxation and Improved Absorption in Epitaxial and Nonepitaxial MoS2/WS2 Heterostructures", *Nano Letters*, vol. 15, no. 1, pp. 486-491, 2014.

# 6. CONCLUSIONS

In this paper, I demonstrate four works corresponding to different applications of tip-enhanced spectroscopy including Raman scattering and photoluminescence. To study molecular modes in the chapter 2 and chapter 3, Raman spectroscopy is of more value. The performance of vibrational modes helps to understand the enhancement mechanisms of the tip enhancement technique. In the chapter 3 and 4, for 2D semiconductors, we refer to photoluminescence emissions because they are corresponding to the inter-band transitions.

Chapter 2 shows the different effects of electromagnetic and chemical mechanisms of TERS. The chemical mechanism allows new bonds to form while tip contacts molecules. This can result in peak shifts involving the changes of peak ratios. In this chapter we also explain the possibility to have new peaks due to metal-molecule bonds formation.

Chapter 3 demonstrate a proof of principle experiment of single-molecule imaging. We designed a careful TERS scanning at 0.5 nm spatial resolution. Moreover, through the data analysis based on the correlation coefficients, we achieve quick DNA sequencing with a reasonable correction rate at 92%.

Chapter 4 and chapter 5 shows how we apply TEPL to photoelectron transitions within 2D semiconductors. The chapter 4 mainly focuses on the hot electron injection effects caused by TEPL. The chapter 5 then discusses the tip-enhanced quantum plasmonic effect and how it impacts the quasiparticle reactions. We prove that metallic

nano-tips can be a good candidate for manipulating electronic properties in a nanoscale regime.

Displaying TERS and TEPL in both classical and quantum conditions, we show how to conduct single-molecule level mapping of chemical components and active sites of nano-reactors.

APPENDIX A

SUPPLEMENTARY MATERIALS OF CHAPTER 3*

**Sample preparation**

M13mp18 single stranded bacteriophage DNA was produced in-house following a previously established protocol. [1] Gold substrates (Ted Pella) were cleaned with compressed air immediately before sample deposition. M13mp18 ssDNA in 50 μL of 1X TAE-Mg buffer (40 mM Tris-HCl pH 7.5, 20 mM acetic acid, 2 mM EDTA, and 12.5 mM magnesium acetate) was deposited on the gold surface and equilibrated at room temperature for 30 s. DNA concentrations from 0.4 nM to 40 pM were tested. A gentle stream of nitrogen was blown over the sample in an attempt to reduce the aggregation and coiling of the circular ssDNA along the gold surface. Excess liquid was then wicked away with a KIMWIPE and each sample was washed once with 50 μL of UltraPure H2O before being fully dried at room temperature.

**AFM and TERS measurement**

A HORIBA-AIST-NT AFM system was used for the AFM-TERS setup. The tip was a silicon corn ($d$ = 20 to 40 nm) covered with a silver layer. The excitation light at 532 nm was focused on the tip through an objective (100X, NA 0.7) mounted at 45 degrees. The substrate was a glass coverslip coated with a thin layer of gold (50 nm thick) and mounted on a motorized stage allowing the stage to shift during TERS scanning. The

* Reprinted/adapted with permission from "Tip-enhanced raman imaging of single-stranded DNA with single base resolution" by He, Z., Han, Z., Kizer, M., Linhardt, R. J., Wang, X., Sinyukov, A. M., ... & Scully, M. O., 2018. *Journal of the American Chemical Society*, *141*(2), 753-757, Copyright 2019 by American Chemical Society

tip, controlled by the AFM cantilever, was operated in tapping mode to avoid damaging the sample. The tapping amplitude was set at 10 nm. Meanwhile, the scanning rate was set to 0.5 Hz to attenuate the shear force on the sample during scanning. The tip contacts samples for TERS measurements. The original setpoint of AFM scanning is around 19000 a.u. For TERS measurements, two spectra were collected at each spot using a tip-sample distance $d_{gap} < 1\ nm$ (tip in contact) and $d_{gap} \sim 20\ nm$ (tip retracted). When the tip is in contact, the shift of normal force is 50 nN from the setpoint. The contact gain is 500. The acquisition time for each spectrum was 4 s. The laser power at the focal volume is 1 mW since higher laser power can easily damage DNA. All measurements are performed under the ambient condition.

**Data analysis**

The correlations between the measure spectra and a template is:

$$Corr(a,b) = \frac{\sum_i (a_i - \bar{a})(b_i - \bar{b})}{\sqrt{\sum_j (a_j - \bar{a})^2 \sum_k (b_k - \bar{b})^2}} \quad \text{(A.1)}$$

where $a$ and $b$ represent the intensities of measurements and templates respectively. The values $\bar{a}$ and $\bar{b}$ are the average values of the intensity arrays of $a$ and $b$. By scanning the center of reference Gaussian peaks in these ranges, the normalized correlation coefficient can be found to evaluate probabilities of four nucleobases.

$$P_i = \frac{Corr_i}{\sum_j Corr_j} \quad \text{(A.2)}$$

where $i$ or $j$ represents bases A, G, C, or T, and Pi represents the probability of the nucleobase type $i$.

**Table A1. The peak assignment table of DNA nucleobases. [2,3,4,5,6] Only separated peaks of A, C, G, T bases are shown. Labels A1, A2, C1, C2, G1, G2, T1, T2 are used for the following discussion.**

| Base | Label | Raman Shift ($cm^{-1}$) | Vibration mode |
|---|---|---|---|
| A | A1 | 735~737 [1] | Ring breathing |
| | A2 | 1467~1492 [1, 2, 3, 4] | C=N stretch, CH bend, CN |
| C | C1 | 799~801 [1, 2] | Ring breathing |
| | C2 | 1235~1270 [1, 2, 3, 4] | C-N ring stretch |
| G | G1 | 954~958 [1] | 5-ring deformation |
| | G2 | 1545~1554 [1, 2, 4] | Ring stretch CN |
| T | T1 | 778~782 [1] | Ring breathing |
| | T2 | 1366~1373 [2, 3, 4] | CN, $CH_3$ stretch |

**Table A2. Six repeating results from 3 different samples. Sample 1 and the DNA in Fig. 3.4 are on the same substrate. Samples 2 and 3 are on a different substrate. Three different tips are used for sample1, 2 and 3. Samples 2 and 3 both contain 10 fmol of M13mp18 DNA. The error of TERS sequencing and the average error for a random sequence are shown. The random trials were repeated 100,000 times for each case.**

| Position | Sequence | Measurement | Error | Average error for random sequence |
|---|---|---|---|---|
| Sample1_row55 | GTGGGCCATCG | GTGGGCCAGCG | 1/11 | 2.42/11 |
| Sample2_row49 | CCTCAACCTCC | CCCCAACCTCC | 1/11 | 2.42/11 |
| Sample2_row65 | TAAAATATATTT | TAAAATATATTT | 0/12 | 2.89/12 |
| Sample2_row66 | TAACTAAAATATATTT | TAATTAAAATATATTT | 1/16 | 4.95/16 |
| Sample3_row38 | TATAAAAAGAT | TATGAAAAGAT | 1/11 | 2.42/11 |
| Sample3_row40 | TTAAATGTAATTA | TTAAATATAATTA | 1/13 | 3.40/13 |

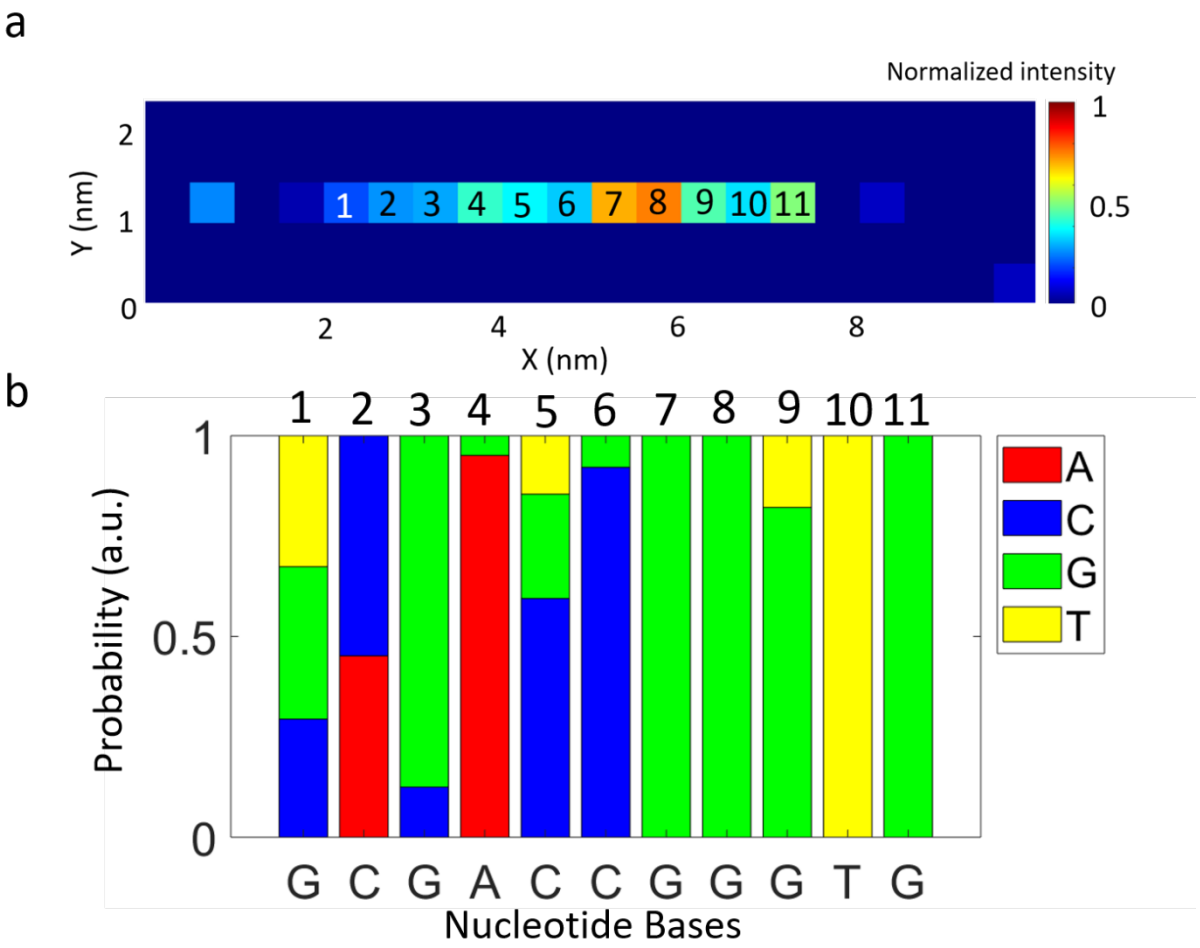


**Figure A1. A sample bar chart from the sample 1 row 55 in Table A2. (a) The TERS image shows a DNA strand width of 0.5 nm. (b) DNA sequence is retrieved from TERS signals and labeled at the bottom. The bar length shows the probability of each nucleobase type.**

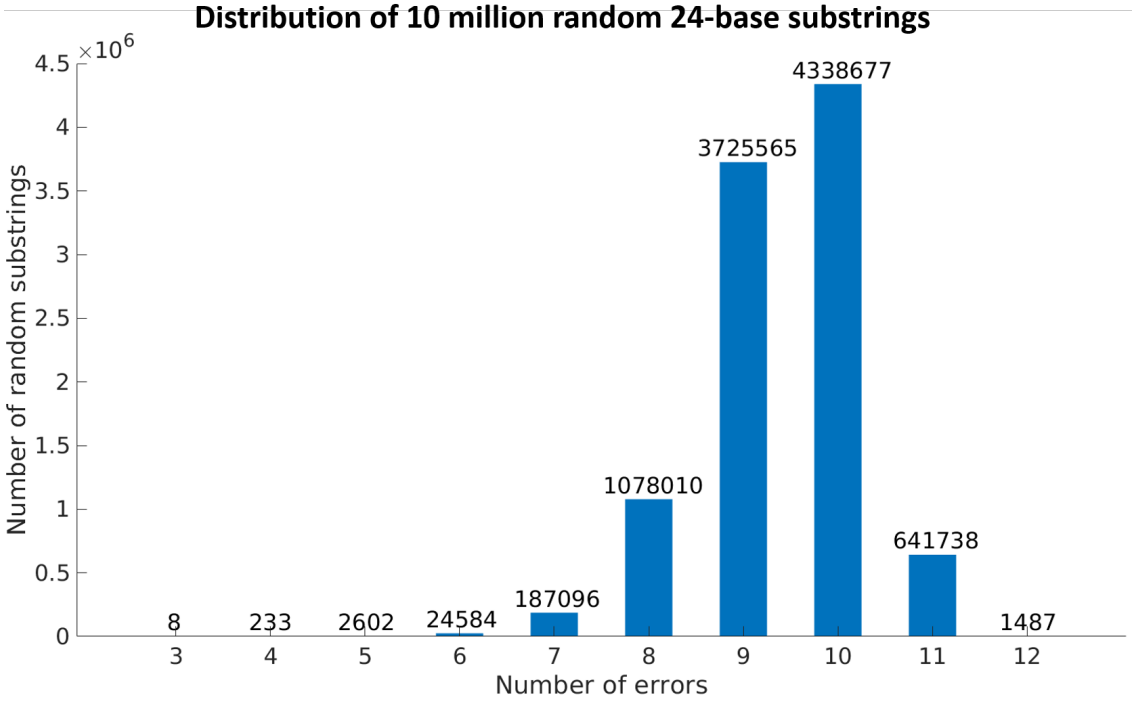


**Figure A2. The test of the best sequence matching with 24-base random strings and any 24-base string of the 7249-base M13mp18 DNA. It was repeated for 10 million times. The average number of mismatching errors is 9.4. The probability of our results (2 errors in 24 bases) is less than 1/10,000,000.**

a

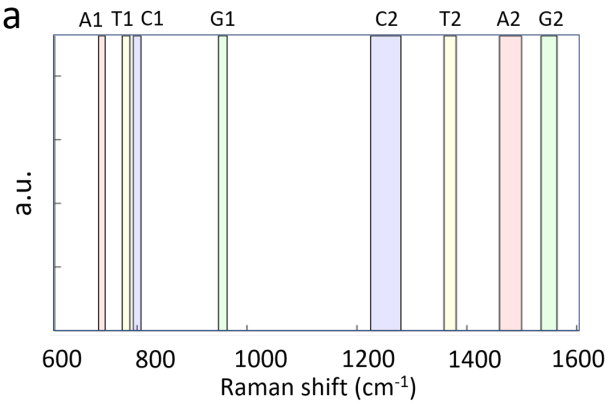


b

| Base | Label | Amplitude | FWHM ($cm^{-1}$) |
|---|---|---|---|
| A | A1 | 1 | 10 |
| | A2 | 2/5 | 15 |
| C | C1 | 1 | 12 |
| | C2 | 1 | 20 |
| G | G1 | 1 | 12 |
| | G2 | 1/2 | 20 |
| T | T1 | 1 | 10 |
| | T2 | 1 | 15 |

**Figure A3. The spectral templates for A, C, G, T. We assume a Gaussian function for the spectral templates:**

$$g = Ae^{\frac{-(x-x_0)^2}{2\sigma^2}}$$

**(a) Because the TERS peaks may shift due to the impact of the plasmonic tip, we need to consider spectral templates with ranges of peak values. The centers of the template peaks are located in the range showed by the width of the corresponding bars in (a). We vary the peak centers using the parameter x0 to achieve the maximum correlation coefficients in Eq. 1. The normalized amplitudes and FWHMs used in our calculation are listed in (b) according to the previous publications. [2, 4]**

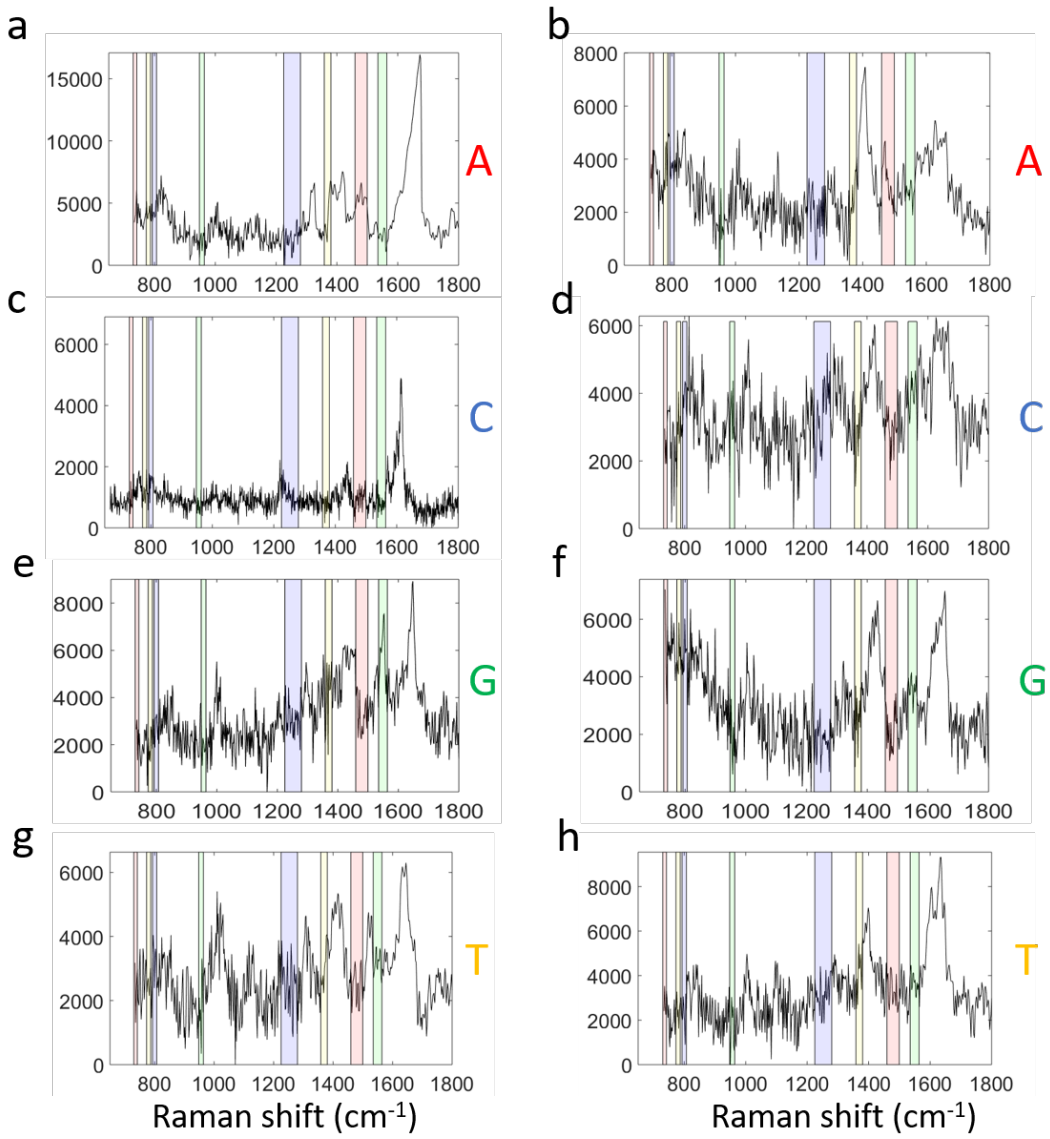


**Figure A4. The spectra of 4 nucleobases. The third-order polynomial baseline correction was applied in order to identify peaks. The corresponding bases are labelled on the right side. The spectra (a, b, d-h) are related to spots 15(A), 21(A), 26(GC), 7(G), 8(G), 13(T), 19(T) shown in Fig. 3.4 (c) is at the spot 2 of "sample2_row49" displayed in Table A2.**

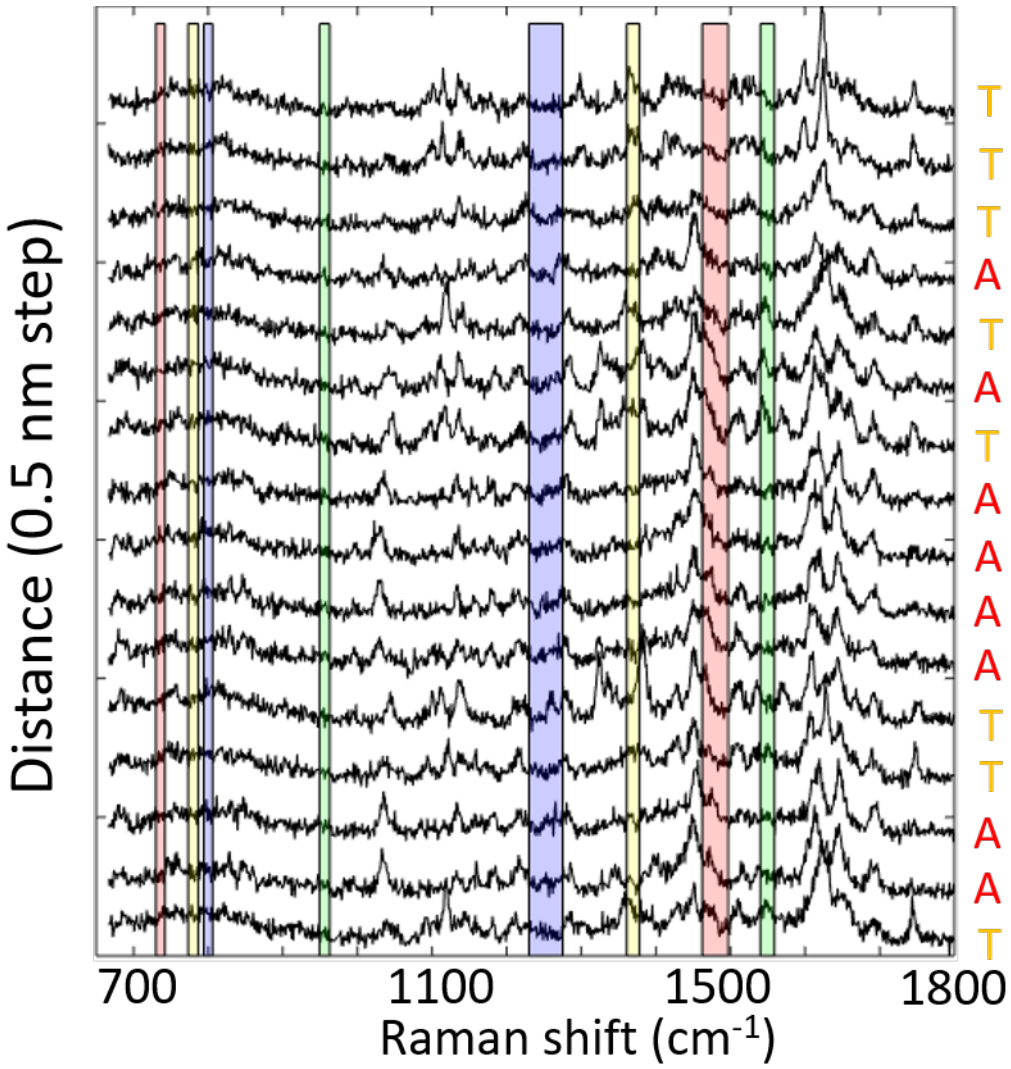


**Figure A5. The row data of "sample2_row66" in Table A2. The measured bases are label on the right side of each spectrum.**

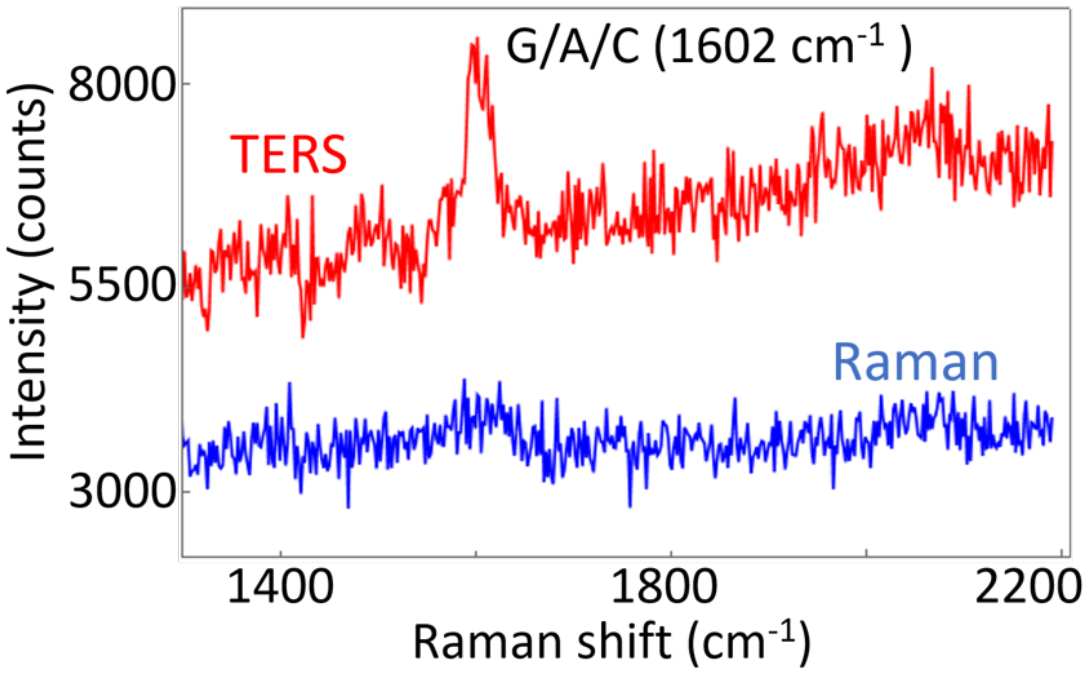


**Figure A6. Enhancement of TERS (red) compared to the standard Raman (blue) signal at the sample spot with an acquisition time of 4 s. The peak at 1602 cm-1 corresponds to the vibration modes of nucleobases.**

**References**

(1) Bellot, G.; McClintock, M. A.; Chou, J. J.; Shih, W. M. DNA Nanotubes for NMR Structure Determination of Membrane Proteins. *Nat. Protoc.* **2013**, *8* (4), 755–770.

(2) Madzharova, F.; Heiner, Z.; Gühlke, M.; Kneipp, J. Surface-Enhanced Hyper-Raman Spectra of Adenine, Guanine, Cytosine, Thymine, and Uracil. *J. Phys. Chem. C* **2016**, *120* (28), 15415–15423.

(3) Treffer, R.; Lin, X.; Bailo, E.; Deckert-Gaudig, T.; Deckert, V. Distinction of Nucleobases – a Tip-Enhanced Raman Approach. *Beilstein J. Nanotechnol.* **2011**, *2*, 628–637.

(4) Yang, S. Y.; Butler, I. S. Pressure-Tuning Infrared and Raman Microscopy Study of the DNA Bases: Adenine, Guanine, Cytosine, and Thymine. *J. Biomol. Struct. Dyn.* **2013**, *31* (12), 1490–1496.

(5) Peticolas, W. L., Raman Spectroscopy of DNA and Proteins. In *Methods in Enzymology*; Biochemical Spectroscopy; Academic Press, 1995; Vol. 246, pp 389–416.

(6) De Gelder Joke; De Gussem Kris; Vandenabeele Peter; Moens Luc. Reference Database of Raman Spectra of Biological Molecules. *J. Raman Spectrosc.* **2007**, *38* (9), 1133–1147.

APPENDIX B

SUPPLEMENTARY MATERIALS OF CHAPTER 4*

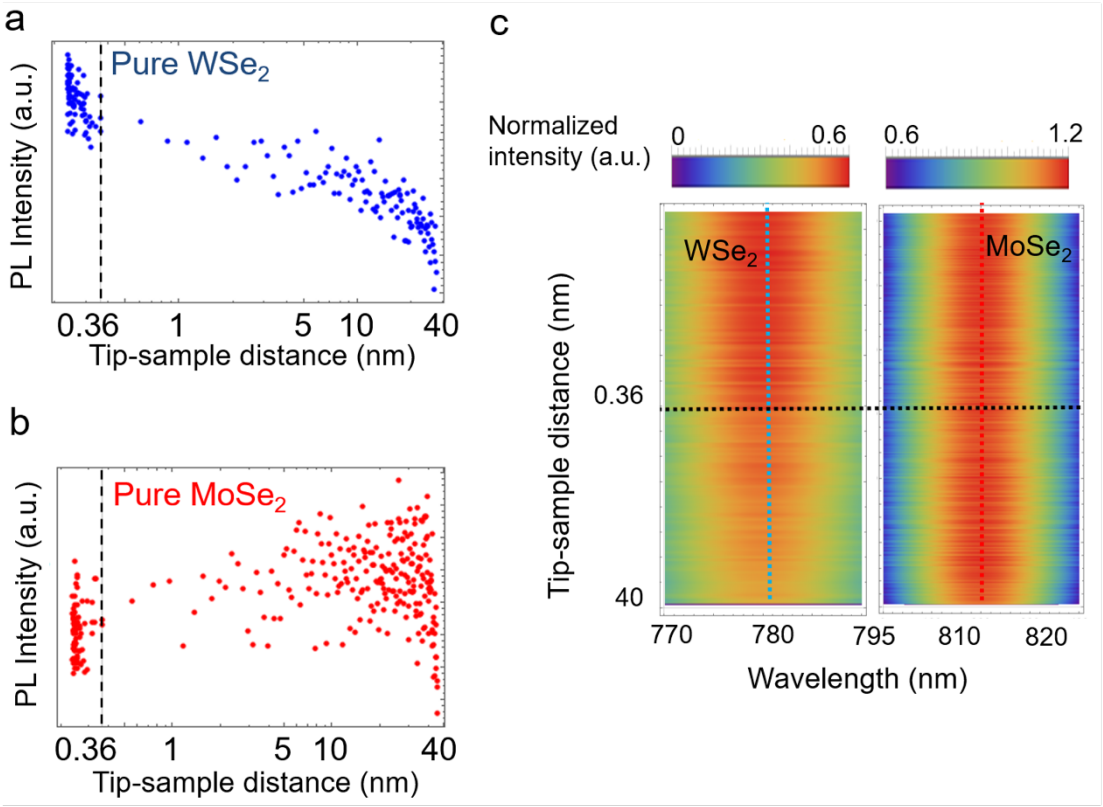


**Figure B1. Distance-dependence of the photoluminescence (PL) intensity of the pure monolayer 2D materials: (a) $WSe_2$ and (b) $MoSe_2$. (a) PL of $WSe_2$ increases when the tip-sample distance decreases from 40 nm to 0.36 nm due to the classical plasmonic enhancement. When the distance is smaller than 0.36 nm, the PL intensity increases within the distance of 0.1 nm due to the classical plasmonic near field enhancement. (b) PL of pure $MoSe_2$ does not show significant enhancement both in the classical ($d > 0.36$ nm) and quantum ($d < 0.36$ nm) regimes under the similar experimental conditions as $WSe_2$ due to the difference in the PL and tunneling efficiencies of the two materials. (c) Distance-dependence of the PL spectra of the pure monolayer $WSe_2$ and $MoSe_2$. Compared with the results from the heterostructure shown in Fig. 4.3a, no significant quenching of $WSe_2$ PL and no enhancement of $MoSe_2$ PL was observed.**

---

* Reprinted/adapted with permission from Tang, C., He, Z., Chen, W., Jia, S., Lou, J., & Voronine, D. V., "Quantum plasmonic hot-electron injection in lateral WSe2/MoSe2 heterostructures." by *Physical Review B*, *98*(4), 041402, 2018, Copyright 2018 by American Physical Society

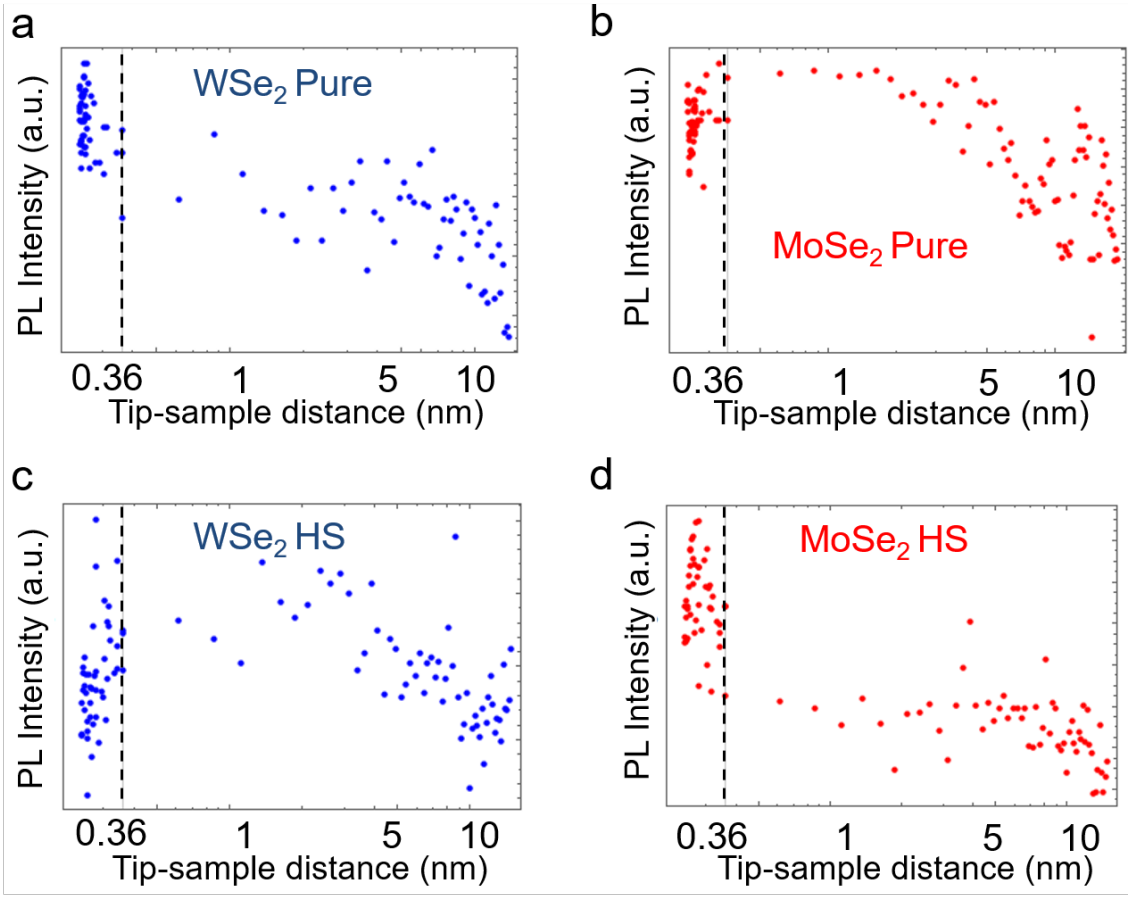


**Figure B2. Repeated experiments using a different $WSe_2$-$MoSe_2$ heterostructure and comparison with the pure 2D materials: PL intensity dependence on the tip-sample distance d. (a) PL of pure $WSe_2$ increases when d > 0.36 nm. (b) PL of pure $MoSe_2$ slightly increases when d > 0.36 nm and slightly decreases when d < 0.36 nm. At the junction of the heterostructure (HS), PL of the $WSe_2$ component shows quenching (c) while the $MoSe_2$ component shows enhancement (d) in the quantum plasmonic regime when d < 0.36 nm.**

APPENDIX C

SUPPLEMENTARY MATERIALS OF CHAPTER 5*

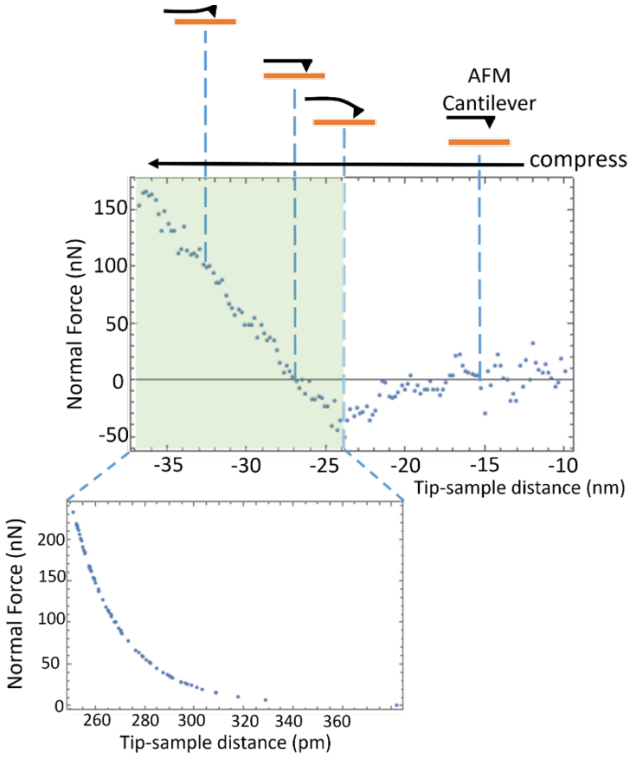


**Figure C1. AFM force-distance diagram. The diagram shows four stages during the tip-sample approach. (I) When the tip is far from the sample (d > 10 nm), the interaction force between the tip and the sample is weak. (II) When the tip is close to the sample surface (0.35 nm < d < 10 nm), the tip interacts with the sample and "jumps to contact" due to the attractive van der Waals (vdW) forces. (III) Further approach beyond the vdW contact distance (d < 0.35 nm) leads to a further decrease of the tip-sample distance. (IV) The vdW repulsive force surpasses the attractive force in the linear force-distance regime where the actual normal force is $\Delta N = N_{vdW} - N_{tension}$ (18). The vdW repulsive force is estimated by $N_{vdW} = \alpha x^{-13}$, where $\alpha \sim 10^{-7}\ nN \cdot nm^{13}$ is determined at the balance point ($x = r_{Au} + r_S$, $N_{vdW} = N_{tension}$). The resulting actual force-distance relation for x < 0.35 nm is shown in the inset below (blue dots).**

---

* Reprinted/adapted with permission from "Quantum plasmonic control of trions in a picocavity with monolayer WS2." by He, Z., Han, Z., Yuan, J., Sinyukov, A. M., Eleuch, H., Niu, C., ... & Scully, M. O., 2019. *Science advances*, *5*(10), eaau8763. © The Authors, some rights reserved; exclusive licensee American Association for the Advancement of Science. Distributed under a Creative Commons Attribution NonCommercial License 4.0 (CC BY-NC) http://creativecommons.org/licenses/by-nc/4.0/

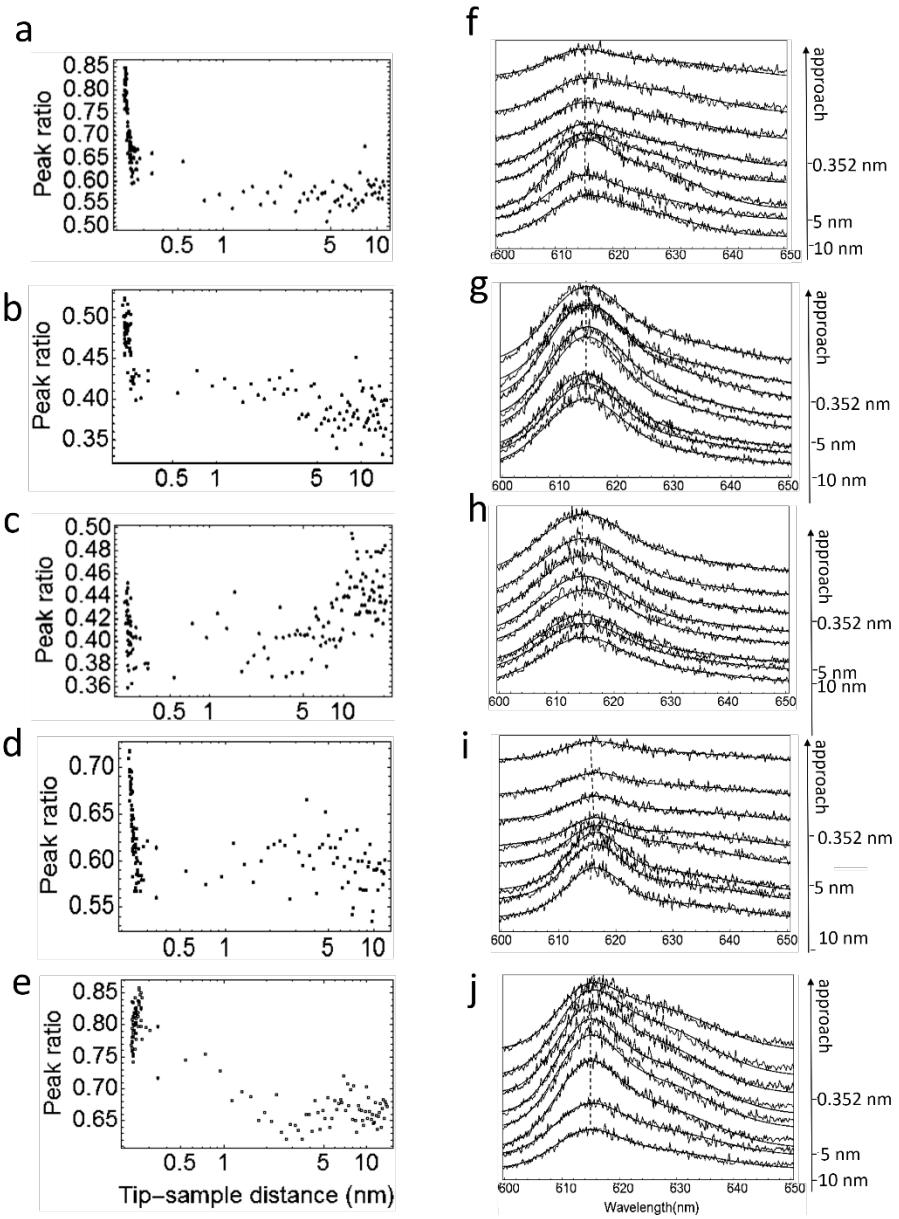


**Figure C2. Tip-sample distance dependence of the neutral exciton/trion photoluminescence. (a) – (e) Tip-sample distance dependence of the photoluminescence (PL) peak ratio $I_{X^-}/(I_{X^0} + I_{X^-})$ and (f) – (j) PL spectra at different tip-sample distances (highlighted in the decreasing order by the approach arrows) corresponding to the spatial locations marked A–E, respectively, in the $WS_2$ nanoflake shown in Figs. 5.3a and 5.3b.**

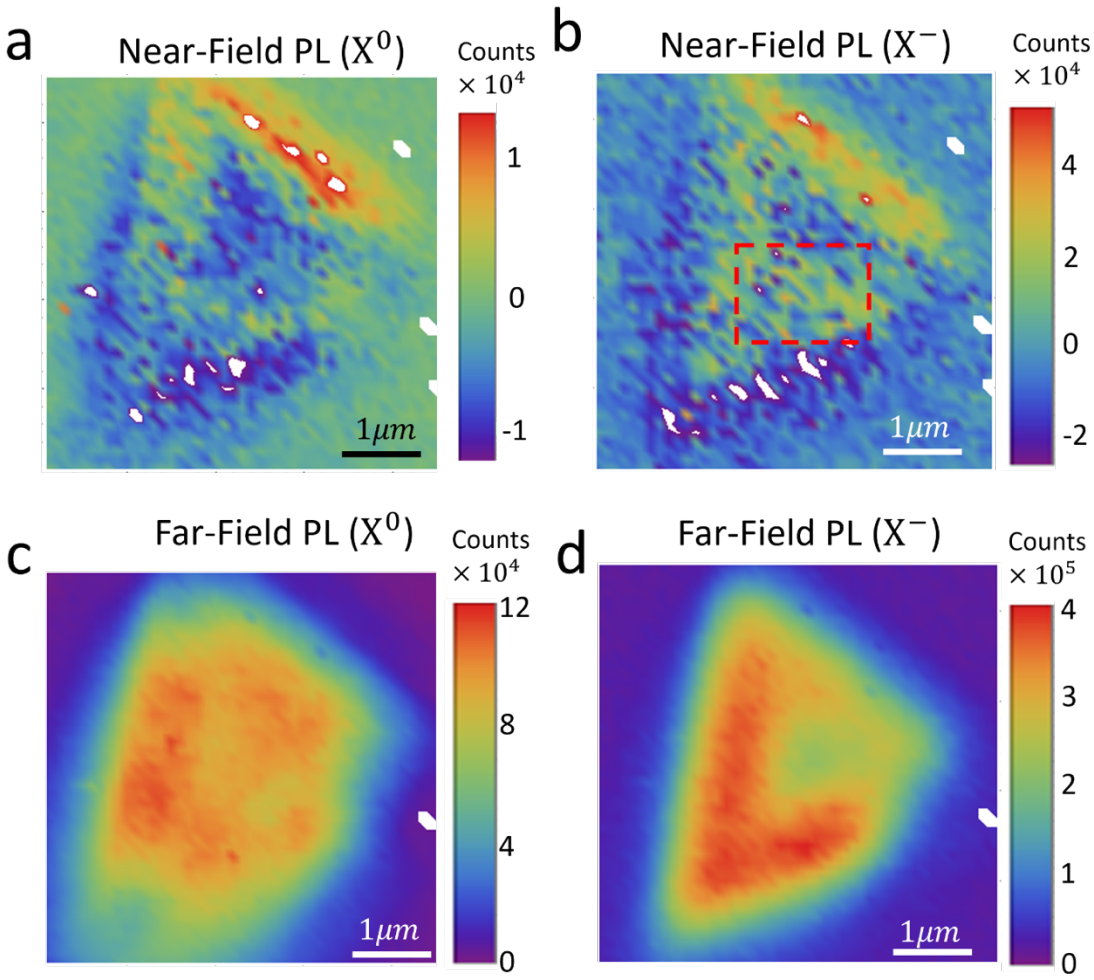


**Figure C3. Classical TEPL imaging. Spatial maps of the near-field (a, b) and far-field (c, d) PL intensities of neutral excitons $X^0$ (a, c) and trions $X^-$ (b, d) in the complex $WS_2$ nanoflake in a Au-Ag cavity obtained with similar experimental parameters as shown in Fig. 5.3 except for a different AFM setpoint value, which reduces the normal force of the tip on the sample and increases the tip-sample distance. This NF images in (a) and (b) have a larger contribution of the classical TEPL signal. The red dashed line highlights the selected area with a zoomed-in image shown in Figure C8.**

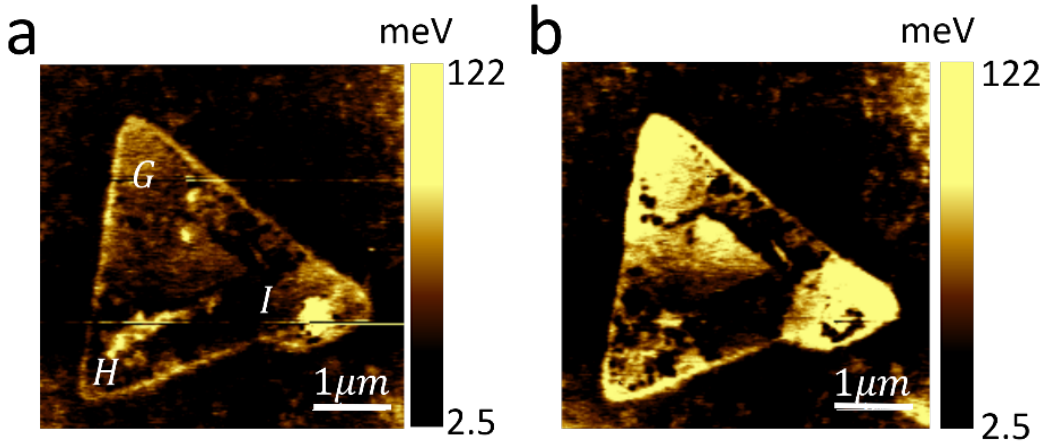


**Figure C4. Kelvin probe force microscopy. The KPFM results under different conditions: (a) without laser; (b) with a 532 nm laser. Laser power was 400 $\mu W$, which is same as for the TEQPL measurement. The CPD values of the corner regions G and I are substantially enhanced due to the charge doping effect.**

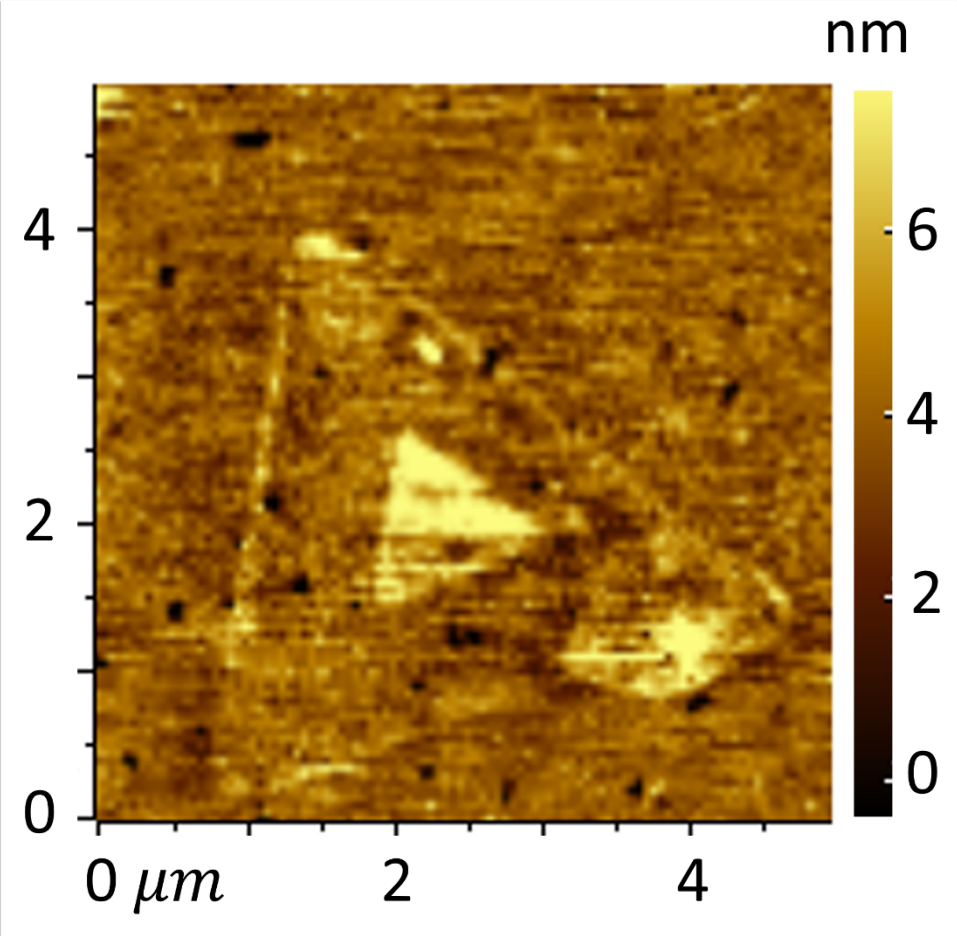


**Figure C5. AFM obtained during TEQPL imaging. AFM height profiles of the complex $WS_2$ nanoflake obtained during the TEQPL imaging simultaneously with the optical FF and NF maps shown in Fig. 5.3. No significant thermal drift is observed.**

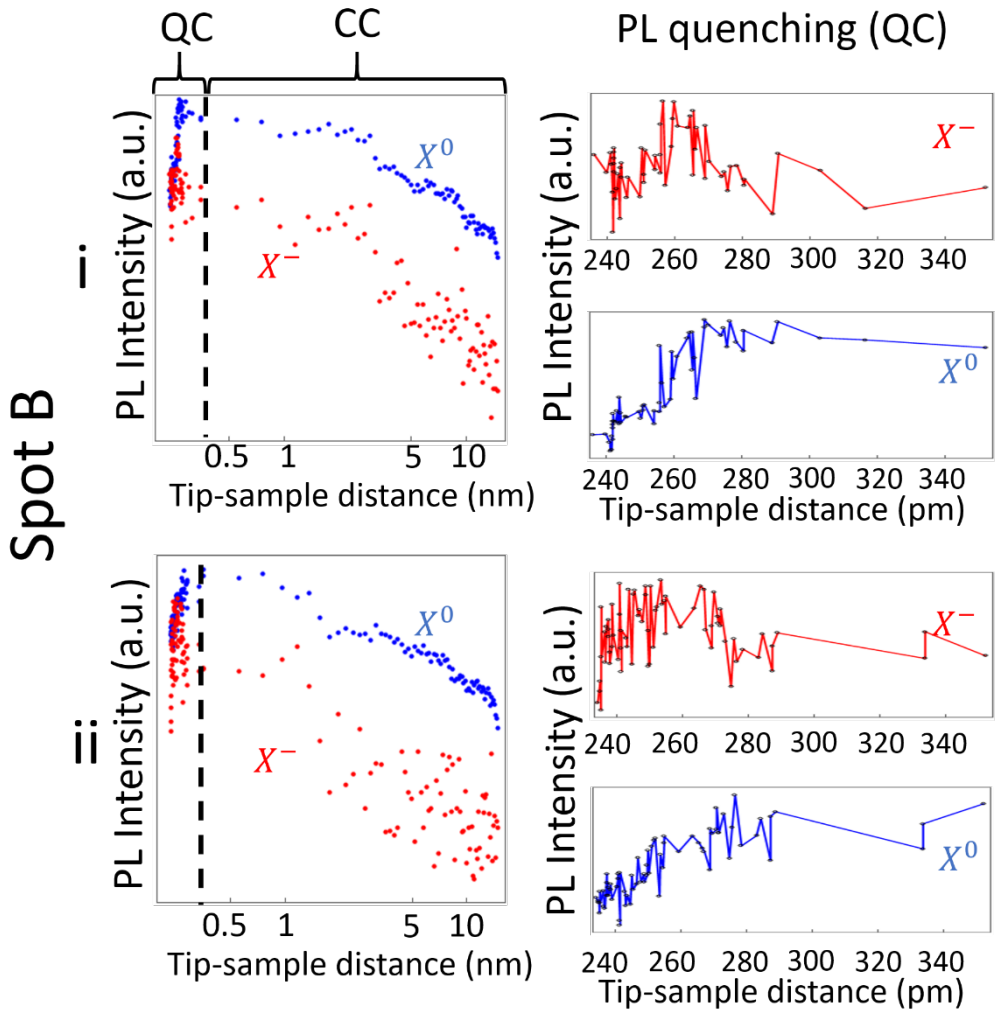


**Figure C6. Repeated distance dependence measurements of spot B. Reproducibility: repeated experiments on spot B marked on a complex $WS_2$ nanoflake in Fig. 5.3a for two consecutive measurements (i) and (ii). Distance-dependent PL intensity of neutral excitons $X^0$ (blue) and trions $X^-$ (red) in the whole range (left) including the classical coupling (CC) and quantum coupling (QC) regimes, and the zoomed-in distance dependence in the QC regime (right).**

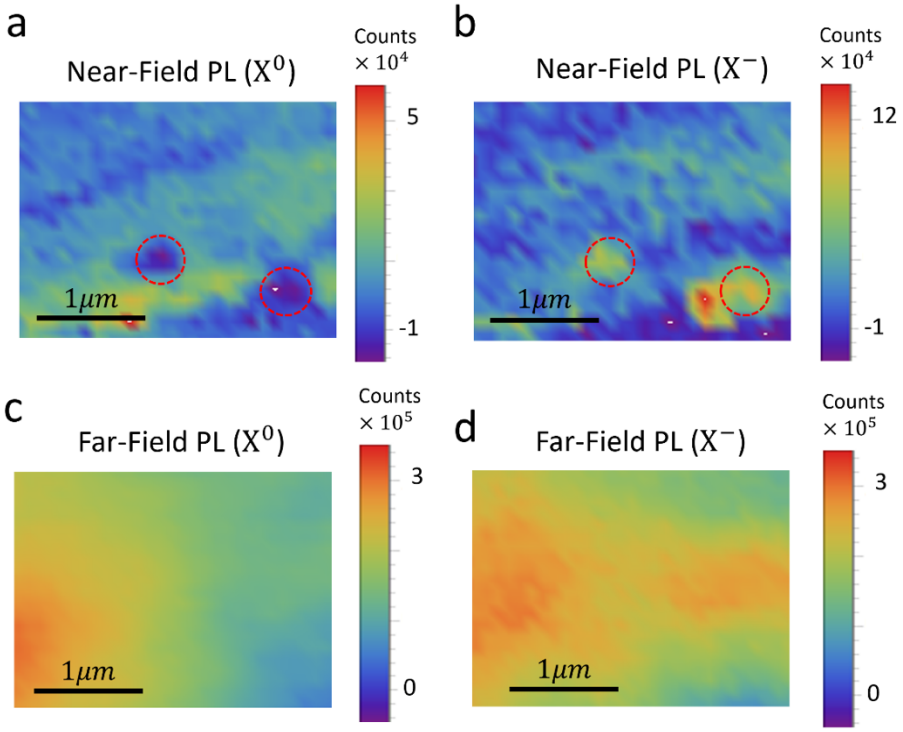


**Figure C7. Anti-correlated distributions of neutral excitons and trions under TEQPL. Spatial maps of the near-field (a, b) and far-field (c, d) PL intensities of neutral excitons $X^0$ (a, c) and trions $X^-$ (b, d) from a zoomed-in area in complex $WS_2$ nanoflake in a Au-Ag cavity marked by a yellow dashed rectangle in Fig. 5.3e. Near-field PL signals (a) and (b) show anti-correlated spatial distributions of neutral excitons and trions, revealing trion "hot spots" highlighted by dashed circles in (b). The corresponding far-field PL images (c) and (d) show poor spatial resolution and lack of any anti-correlated features due to the $X^0 \rightarrow X^-$ transition.**

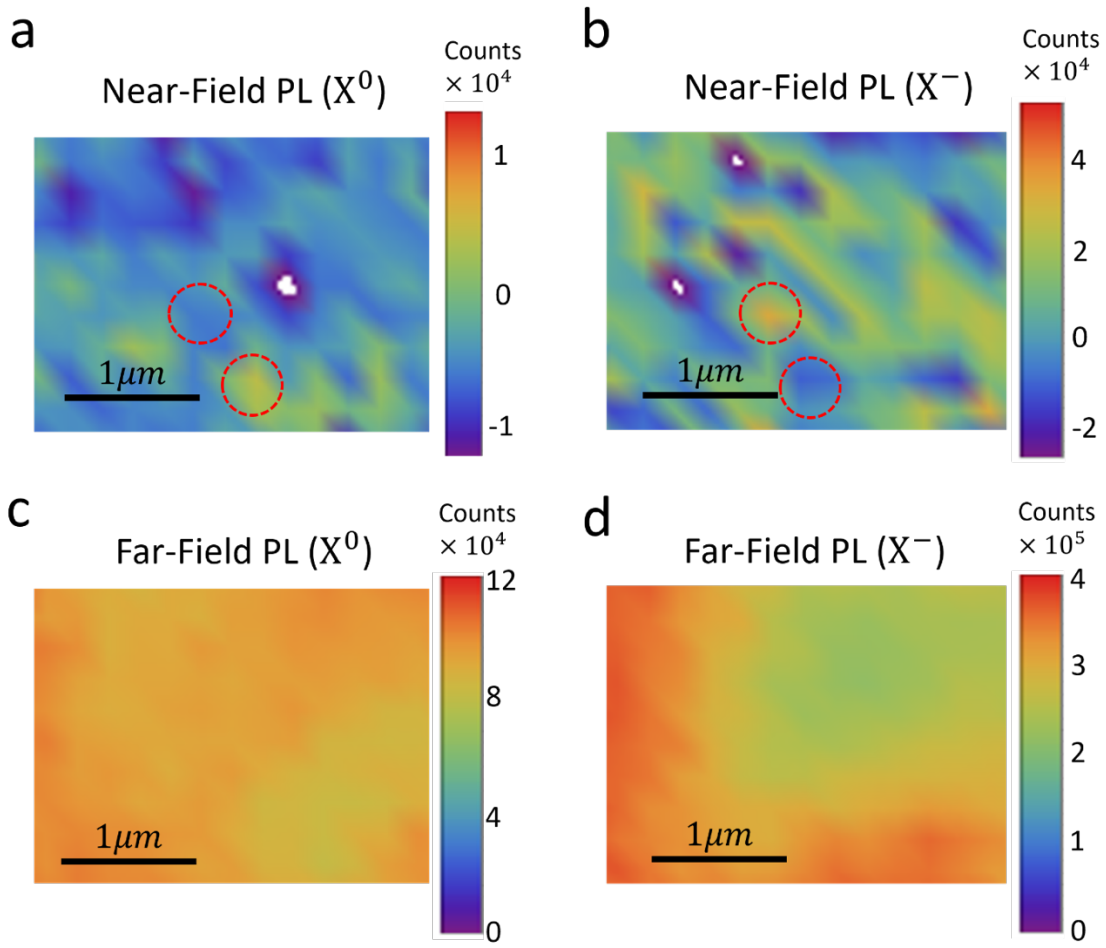


**Figure C8. Mixed distributions of neutral excitons and trions. Spatial maps of the near-field (a, b) and far-field (c, d) PL intensities of neutral excitons $X^0$ (a, c) and trions $X^-$ (b, d) from a zoomed-in area highlighted by the red dashed rectangle in complex WS2 nanoflake in a Au-Ag cavity shown in Figure C3. Near-field PL signals (a) and (b) show anti-correlated spatial distributions of neutral excitons and trions, revealing trion "hot spots" highlighted by dashed circles. The corresponding far-field PL images (c) and (d) show poor spatial resolution and lack of any anti-correlated features due to the $X^0 \rightarrow X^-$ transition.**

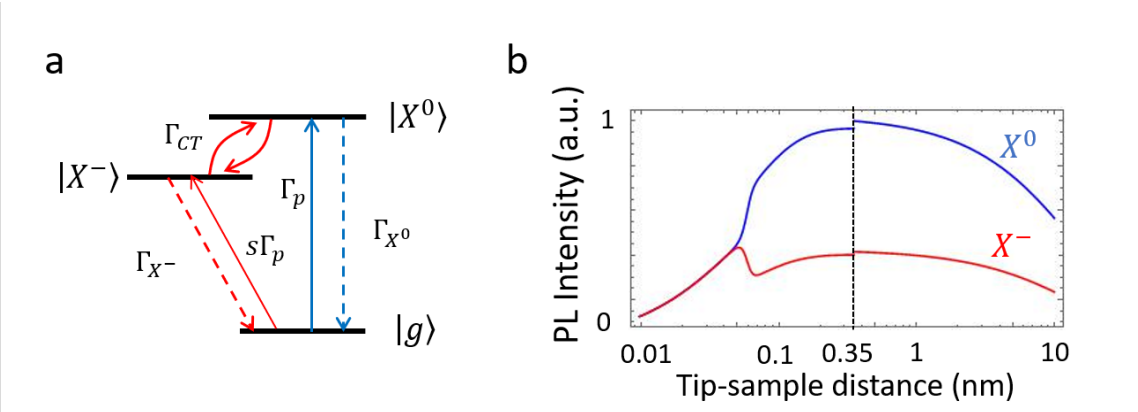


**Figure C9. The model and simulation of TEQPL. Theoretical model (a) and simulated distance dependence (b) of the PL of neutral excitons $X^0$ (blue) and trions $X^-$ (red) in monolayer WS2 in a Au-Ag cavity. The main kinetic parameters are the neutral exciton pumping rate $\Gamma_p$, charge transfer $X^0 \rightarrow X^-$ transition rate $\Gamma_{CT}$, and the trion pumping rate $s\Gamma_p$, where s is the relative neutral exciton-trion pumping ratio. $\Gamma_{X0}$ and $\Gamma_{X-}$ are the neutral exciton and trion decay rates, respectively.**

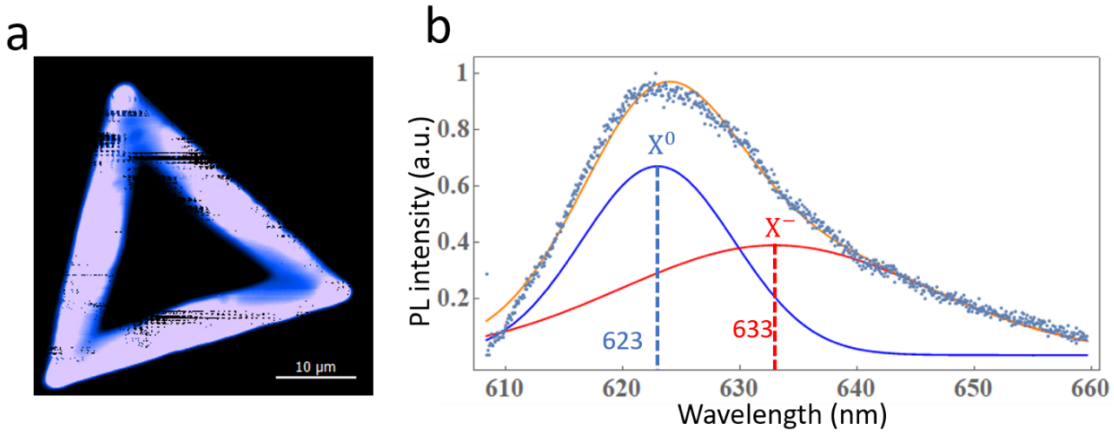


**Figure C10. Photoluminescence (PL) and peak assignment of $WS_2$ on $Si/SiO_2$. (a) Integrated PL image of monolayer $WS_2$ (outer area) with the bilayer $WS_2$ in the center. (b) Experimental PL spectrum (dotted) and Gaussian fittings of $X^0$ (blue line) and $X^-$ (red line) in monolayer $WS_2$ in the CC regime, centered at 623 nm and 633 nm, respectively.**